UCLA
UCLA Electronic Theses and Dissertations

Title
Addressing Practical Challenges in High-capacity Multi-antenna Communication Systems

Permalink
https://escholarship.org/uc/item/1rj7c5dd

Author
Zhao, Heng

Publication Date
2019

Peer reviewed|Thesis/dissertation

eScholarship.org Powered by the California Digital Library
University of California

UNIVERSITY OF CALIFORNIA

Los Angeles

Addressing Practical Challenges in High-capacity Multi-antenna Communication Systems

A dissertation submitted in partial satisfaction

of the requirements for the degree

Doctor of Philosophy in Electrical and Computer Engineering

by

Heng Zhao

2019

© Copyright by

Heng Zhao

2019

ABSTRACT OF THE DISSERTATION

Addressing Practical Challenges in High-capacity Multi-antenna Communication Systems

by

Heng Zhao
Doctor of Philosophy in Electrical and Computer Engineering
University of California, Los Angeles, 2019
Professor Gregory J Pottie, Co-Chair
Professor Babak Daneshrad, Co-Chair

In the recent decades, there have been dramatic changes in the ways people create and share information, hence a demand for wireless communication systems with over 100 Gb/s data rate has been envisioned. Promising techniques have been devised by researchers to fulfill this expectation, such as interference alignment (IA) and THz communication and many more. In theory, given ideal assumptions, they show extraordinary increases in the promised data rate relative to current wireless communication systems. Nevertheless, because of the hardware impairments, many practical challenges have to be addressed before bringing these advanced techniques from theory to practice. In this dissertation, a selection of practical issues of interference alignment and THz communication are discussed.

First, we consider the synchronization and channel estimation problem associated with enabling IA. Before achieving IA, in view of the uncoordinated interference, a concurrent synchronization and channel estimation mechanism with robustness against co-channel interference is needed. We start by deriving the maximum-likelihood expressions for optimal estimators. Then, it is realized that such estimators are infeasible in practice for requiring a computationally costly 2-D search. To reduce the complexity, we propose a Zadoff-Chu sequence based pilot structure. By utilizing its unique properties, the 2-D search problem can be converted into two 1-D search problems. Experimental results verify the great per-

formance of our proposed method in terms of both the residual frequency offset and the sum rate of an IA network. Second, we focus on the channel reciprocity in time division duplex (TDD) networks. The physical channel is reciprocal, but the channel considered by IA is not, because it also involves the radio frequency (RF) front-ends of the transceiver. The difference between the two individual circuits yields mismatch between the forward and backward channels. We provide the modeling of the non-reciprocity for the TDD MIMO channels, and propose a corresponding calibration method to minimize the mismatch. Experimental validation has been conducted. The results highlight the indispensability of the reciprocity calibration for approaching the network capacity promised by IA. Last, with a view to assessing THz communication system design requirements in practice, we measure the channels for both 350 GHz and 650 GHz carrier frequencies in a typical indoor environment. To obtain the spatial and temporal characteristics of the channel, the power angle profile (PAP) and the power delay profile (PDP) are measured using our proposed measurement systems and methods. From the measurement results, we have observed important facts regarding the THz wave propagation, which significantly affect the requirements for designing an indoor THz communication system.

The dissertation of Heng Zhao is approved.

Mona Jarrahi

Danijela Cabric

Gregory J Pottie, Committee Co-Chair

Babak Daneshrad, Committee Co-Chair

University of California, Los Angeles

2019

To my wife and my parents

TABLE OF CONTENTS

List of Figures . . . . . **x**

List of Tables . . . . . **xii**

Acknowledgments . . . . . **xiii**

Vita . . . . . **xiv**

1 Introduction **1**

1.1 Background 1

1.2 Interference Alignment 1

1.3 Terahertz Communication 3

1.4 Practical Challenges 4

1.5 Contribution of this Dissertation 6

1.6 Notations 6

2 Concurrent Synchronization and Channel Estimation for Interference Alignment Using Zadoff-Chu Sequence **8**

2.1 Overview 8

2.2 Signal and System Model 10

2.3 Optimum Synchronization and Channel Estimation 12

2.3.1 Maximum Likelihood Estimators 12

2.3.2 Robustness against Co-channel Interference 14

2.3.3 Extremely High Complexity 15

2.4 A Practical Method Using Zadoff-Chu Sequences 16

2.4.1 Zadoff-Chu Sequence Based Pilots 16
2.4.2 Simplified Maximum Likelihood Synchronization 17
2.4.3 Maximum Likelihood Channel Estimation 19
2.5 Validating Synchronization under Co-channel Interference 20
2.5.1 Experimental Setup 20
2.5.2 With and Without Inteference 21
2.5.3 Synchronization Results 21
2.6 IA with Concurrent Synchronization and Channel Estimation 23
2.6.1 Experimental Setup 23
2.6.2 Concurrent and Sequential Training 24
2.6.3 Calculating the IA solutions 25
2.6.4 Interference Alignment Performance 26
2.7 Summary 28

3 Reciprocity Calibration of TDD MIMO Channel for Interference Alignment 29
3.1 Overview 29
3.2 Channel Reciprocity Based Interference Alignment 32
3.2.1 The Concept of Interference Alignment 32
3.2.2 Calculating IA Solutions via Reciprocity 33
3.3 Non-reciprocity of Baseband TDD MIMO Channel 36
3.3.1 Coupling Matrix in Transmit Mode 37
3.3.2 Coupling Matrix in Receive Mode 39
3.3.3 Non-reciprocity of Mutual Coupling 41
3.4 Reciprocity Calibration for IA Network 42

3.4.1 Calibration with Single-antenna Reference Node 43
3.4.2 Calibration Matrix Estimation 43
3.5 Experimental Validation of the Proposed Calibration Method 45
3.5.1 Hardware Setup 45
3.5.2 Acquiring Bi-directional Channel Estimates 47
3.5.3 Validating the Calibration Matrices 49
3.6 Impact on Interference Alignment Performance 52
3.7 Summary 55

4 Extending Spatial and Temporal Characterization of Indoor Wireless Channels from 350 GHz to 650 GHz 57
4.1 Overview 57
4.2 Measurement System 59
4.2.1 Power Angle Profile Measurement System 59
4.2.2 Power Delay Profile Measurement System 61
4.3 Measurement Methods 63
4.3.1 PAP Measurements 64
4.3.2 PDP Measurements 66
4.4 Measurement Results 70
4.4.1 Power Angle Profiles 70
4.4.2 Power Delay Profiles 76
4.5 Summary 82

5 Conclusions 84
5.1 Summary of Contributions 84
5.2 Future Work 86

5.2.1 Prototyping the First Real-time IA System via Channel Reciprocity 86

5.2.2 Indoor Communication Link with Smart Massive Antenna Array . . 86

References **88**

LIST OF FIGURES

1.1 Trends in speed of wireless technology. 2

1.2 Atmospheric attenuation spectrum. 5

2.1 Topology of an IA network with K users 11

2.2 The two dimensional function in (2.18) under co-channel interference. 15

2.3 The pilot structure based on conjugate pairs of Zadoff-Chu sequences. 17

2.4 The two dimensional function in (2.18) using Zadoff-Chu sequence. 18

2.5 The experimental setup for validating synchronization using Zadoff-Chu sequences. 20

2.6 The signaling pattern of the transmitters. 21

2.7 The frequency offset estimation results given different ZC sequence lengths. . . . 22

2.8 The experimental setup for studying the interference alignment performance. . . 23

2.9 The signaling arrangement of transmitters in the 3-user interference alignment. . 24

2.10 The cumulative distribution function of the sum rate for interference alignment with concurrent synchronization and channel estimation. 27

3.1 The conceptual illustration of IA in a 3-user interference channel with 2×2 MIMO radios. 32

3.2 The pictorial representation of iterative interference alignment algorithms that exploit channel reciprocity. 35

3.3 The block diagram of the baseband TDD MIMO channel. 36

3.4 The mutual coupling effect in transmit mode. 38

3.5 The mutual coupling effect in receive mode. 40

3.6 The floor plan of the experiment environment. 46

3.7 The calibration phase and the verification phase of the reciprocity calibration experiment procedure. 48

3.8 Constellations of calibrated forward and backward channel coefficients. 51

3.9 The evolution of our iterative IA system in different cases of calibration. 54

4.1 Block diagram of the PAP measurement system. 60

4.2 Block diagram of the PDP measurement system. 62

4.3 Floor plan of the investigated conference room. 63

4.4 The improvement of SNR by averaging in time and frequency domains. 69

4.5 The measured power angle profiles for 350 GHz carrier frequency. 71

4.6 The measured power angle profiles for 650 GHz carrier frequency. 72

4.7 The floor plans with the identified paths marked for two Rx locations. 74

4.8 The measured power delay profiles for 350 GHz carrier frequency. 77

4.9 The measured power delay profiles for 650 GHz carrier frequency. 78

4.10 The histograms of the estimated mean excess delay and RMS delay spread for path (7) at 350 GHz and 650 GHz. 80

LIST OF TABLES

4.1 System Configuration for PAP Measurements 65

4.2 System Configuration for PDP Measurements 67

4.3 Spatial Characteristics of the Investigated Paths 75

4.4 Temporal Characteristics of the Investigated Paths 81

ACKNOWLEDGMENTS

As I look back upon my time spent at UCLA since 2014, I realize how fortunate I am in experiencing such an enriched life and meeting so many wonderful people. I would like to express my gratitude to my advisor Professor Babak Daneshrad, who has given me the opportunity to join his research group and has continuously supported me towards becoming an independent researcher. His valuable guidance has been and will always be a great treasure to me. I would also like to thank Professor Gregory Pottie for his optimistic outlook as well as his constant encouragement and support. I appreciate all the help I have received from Professor Mona Jarrahi and Professor Danijela Cabric.

I would like to thank all the people I have had the honor working with. A lot of thanks to my labmates, Hemant Saggar, Kia Karbasi, Nick Kauffroath, and Ehsan Keramat. They are my constant sources of inspiration and have made the lab always a friendly work place. Many thanks to the collaborators from the Terahertz Electronics Laboratory, Leihao Wei and Yenju Lin. Without their help, I could never be brave enough to explore the futuristic THz world. Also, thanks to the great engineers from SILVUS Technology, Sandeep Sasi, Jesse Chen, Yi Jiang, and Weijun Zhu. They are so generous and helped me so much on the hardware platform I have been using for my tests.

I would not be here today without the encouragement and support from my wife and my parents. Thank you for loving me and believing in me. You made the difficult time much easier, the blessed moments happier, and me a much better person.

VITA

2014 – 2015	M.S. in Electrical Engineering
	University of California, Los Angeles
2010 – 2014	B.S. in Information Engineering
	Shanghai Jiao Tong University
Summer 2012	Test Technician Intern
	Hitachi Global Storage Technologies Co. Ltd.
Summer 2013	Software Engineer Intern
	Huawei Shanghai Research Center
Summer 2018	DSP Engineer Intern
	Marvell Semiconductor Inc

PUBLICATIONS

Zhao, Heng, Leihao Wei, Mona Jarrahi, and Gregory Pottie, "Extending Spatial and Temporal Characterization of Indoor Wireless Channels from 350 GHz to 650 GHz," *IEEE Transactions on Terahertz Science and Technology*, 2019.

Zhao, Heng, Leihao Wei, Mona Jarrahi, and Gregory Pottie, "Propagation measurements for indoor wireless communications at 350/650 GHz," In *Infrared Millimetter and Terahertz Waves (IRMMW-THz)*, IEEE 2018.

Kermat, Ehsan, Nicholas Kauffroath, Kia Karbasi, Heng Zhao, Babak Daneshrad, and Gregory Pottie, "Experimental results for low overhead frequency offset estimation in MANETs with concurrent transmission," In *Military Communications Conference (MILCOM)*, IEEE 2017.

Chen, Xiangyu, Heng Zhao, Xiaoying Gan, Hao Feng, Jing Liu, and Xiaohua Tian, "Content delivery in converged network: reward sharing or not?," In *Global Communications Conference (GLOBECOM)*, IEEE 2015.

CHAPTER 1

Introduction

1.1 Background

High-speed high-throughput wireless communication has attracted extensive attention in the past decades because of dramatic changes in the ways people create and share information. The expected data rate to satisfy the demands of the customers is projected to be 100 Gbit/s by 2020 (Fig. 1.1) [NK14]. However, the throughput of today's wireless communication networks is limited by the high occupancy of the available spectrum resources up to 60 GHz. The inefficient utilization of the spectrum due to conservative interference management further reduces the achievable throughput [Rap96]. This trend has been forcing researchers to either increase the network spectral efficiency for existing wireless communication systems or push the carrier frequencies of the transceivers to higher frequencies to allow operation at frequency bands that have not been allocated to any specific active service yet. The two representative techniques are interference alignment and Terahertz communication.

1.2 Interference Alignment

In modern wireless communication networks, interference broadly exists and has significant impairment to successful communications. The cellular networks suffer from inter-cell interference when the same carrier frequency is reused by adjacent cells. The local area networks also have interference problems when the same channel is occupied by multiple users accessing different access points. Similarly, in mobile ad-hoc networks, neighboring nodes interfere with each other if they share the same time and frequency resources. With the presence of

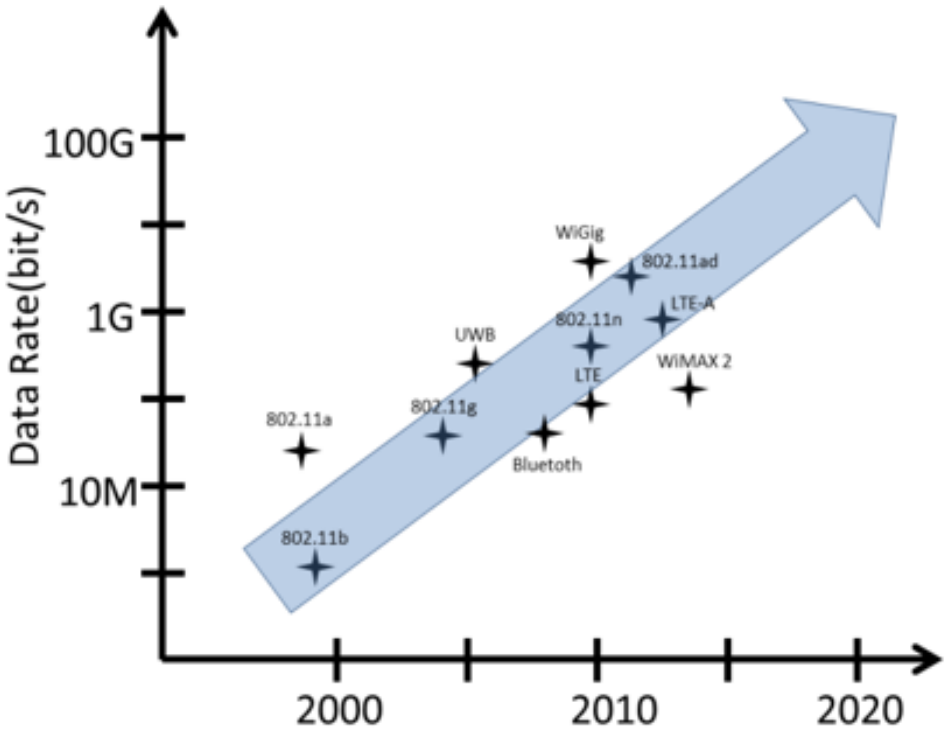

Figure 1.1: Trends in speed of wireless technology.

interference, the number of simultaneous communication links and the consequent system performance are greatly reduced due to conservative interference management.

Conventional methods for dealing with interference often centre on giving each user access to an exclusive fraction of the channel resources. In frequency-division multiple access (FDMA), the frequency spectrum is divided into many pieces, each being occupied by one user. The multiplexing can be easily achieved using filers, which eliminate frequency components out of the band of interest. In time-division multiple access (TDMA), the idea is even simpler, and users take turns to utilize the whole frequency band on a periodic set of time intervals. For random access protocols, the channel occupancy is monitored and users transmit when a channel becomes available. Because there is the possibility of collision, the utilization of the channel resources is typically even much less efficient. Regardless of the protocol, the common strategy is avoiding interference by limiting the number of concurrent transmissions, yielding system performance far short of its limit.

A recently proposed interference management strategy, called interference alignment (IA),

allows the achievable sum data rate of a wireless network to grow linearly as the network size increases [GCJ08, CJ08]. IA exploits the multiple dimensions of the signal space, which can be obtained from the channel diversity in time, frequency, and space domain. The transmitters jointly design their transmitted signals in a cooperative manner such that the observed interference at each receiver only occupies a fraction of the entire signal space. With the alignment of the interfering signals, multiple data links can be established resulting in much higher spectral efficiency, and system performance greatly outperforming that provided by conservative strategies like FDMA and TDMA. Since then, there has been a large number of papers on IA developing its theory and potential applications under various scenarios.

1.3 Terahertz Communication

Other than improving the spectral efficiency, researchers have also been trying to operate wireless communication at Terahertz (THz) frequencies, where more spectral resources are available for future ultra-fast wireless communication systems [SN11]. THz waves are located in the frequency range of 0.3-10 THz between the millimeter waves and the infrared light waves in the electromagnetic spectrum. Because of the scarcity of devices for generating and detecting THz waves, they had rarely been used except in astronomy and its related fields. Until the recent decades, the advances in THz devices, e.g. femtosecond lasers, photo-conductive antennas, and compound semiconductor technologies, have made it possible to utilize THz waves in various applications such as bio-medical science, imaging, and security [Ton07, Sie02]. Of course, wireless communication is also one of the potential THz applications due to the huge bandwidth, and has attracted attention in the THz community.

While communication systems with THz carrier frequencies have been hard to develop so far, we believe a THz communication link with data rates exceeding 100 Gbit/s over 10-20 meter distance is viable in the near future considering the prototyping efforts presented recently [SKA14, NOY16]. A system with this capability can be suitable for the next generation indoor wireless communication systems such as wireless local area networks (WLAN) and wireless personal area networks (WPAN), kiosk downloading, wireless back-hauling, and

data center connections.

1.4 Practical Challenges

Although both IA and THz communication are promising techniques to break the limit of throughput provided by current wireless communication networks, bringing them from theory to practice is not easy. On the one hand, some assumptions they heavily rely on may not hold in practice due to imperfect hardware [EPH13]. Hence, extra effort is required to achieve the exciting performance guaranteed in theory. On the other hand, some preliminary knowledge is necessary to guide the proper implementation of the entire system. In this section, some of the most pressing practical challenges for IA and THz communication are briefly listed respectively.

For interference alignment, we have at least the following challenges to overcome:

- The network capacity can only be achieved at high signal-to-noise ratio (SNR). Given moderate or low SNR levels, the IA performance may fall short of the theoretical maximum. As a result, the IA algorithms need to be modified to work in such scenarios.
- The coherent interference channel is assumed for IA, while the distributed nodes are generally not synchronized. Synchronization should be conducted before IA to remove any frequency and timing offsets between the cooperating nodes. With residual offsets, the additional interference may be introduced, causing performance degradation.
- Calculating IA precoders requires accessibility to accurate global channel state information (CSI) for all nodes. Hence, tremendous resources have to be allocated to pilot transmission, channel estimation, and CSI sharing. For a large-scale distributed network, the interference alignment proves to be too costly in terms of overhead to obtain sufficient IA gain in fast time-varying environments.

Developing Terahertz communication systems also has some major challenges as follows:

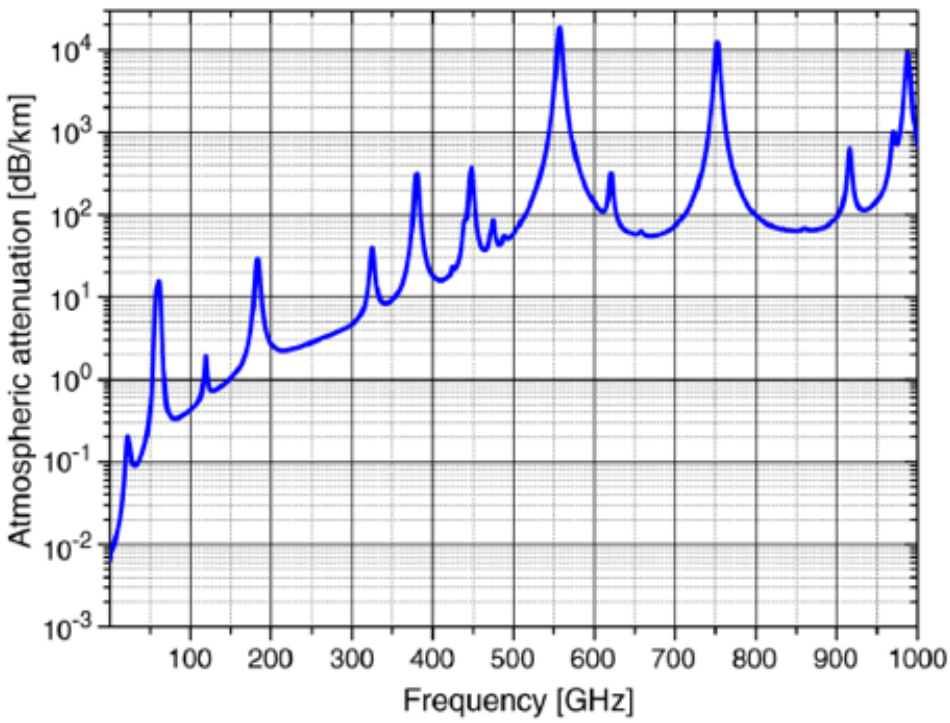

Figure 1.2: Atmospheric attenuation spectrum.

- High-performance THz transmitters and receivers suitable for developing a high SNR compact-size communication link are not available yet. In comparison with the radio frequency (RF) counterparts, the radiation power and detection sensitivity of THz transmitters and receivers are relatively much lower. The performance is mainly restricted by the inherent trade-off between the THz device's size, bandwidth, and power efficiency etc..

- The signal propagation loss at THz carrier frequencies is relatively high. Electromagnetic waves are attenuated due to interaction with water and other atmospheric gases. Although atmospheric losses can be neglected for short range communications at RF frequencies, their impact is rather significant at THz frequencies even for indoor communication systems. Fig. 1.2 shows the atmospheric attenuation measured at sea level given a water vapor density of 7.5 g/m [SWP12].

- The channel models for THz frequencies are not sufficient to determine the most ap-

propriate communication protocol. Existing channel models for RF frequencies do not take into account the high atmospheric propagation losses and many other factors that exist at the THz frequencies. An extensive multi-path channel modeling for a realistic dynamic environment is necessary for developing such THz communication systems, for which the propagation, interference characteristics, and coefficients for reflection, scattering and diffraction would be very different from RF frequencies.

1.5 Contribution of this Dissertation

Since it is not possible to address all the practical challenges of both IA and THz communication as shown in the previous section through a Ph.D. program, three major challenges of interest in practice are targeted in the subsequent chapters of this dissertation.

Chapter 2 focuses on achieving interference alignment using Zadoff-Chu (ZC) sequences, whose unique properties enable concurrent synchronization and channel estimation. The experimental results validate the viability of the proposed ZC sequence based algorithm. In Chapter 3, the reciprocity of time division duplex (TDD) multiple-input multiple-output (MIMO) channel is studied. Being taken for granted by many distributed IA algorithms, the assumption of channel reciprocity actually requires calibration to hold. Correspondingly, a reciprocity calibration method is proposed with experimental validation. Chapter 4 is devoted to extending the spatial and temporal characterization of THz indoor channels from 350 GHz to 650 GHz. An extensive THz channel measurement campaign is conducted in a typical indoor environment, and the measurement results provide important preliminary knowledge for future THz indoor communication system design.

1.6 Notations

To wrap up this chapter, the notation used throughout this dissertation is introduced. Lower and upper case bold fonts represent vectors and matrices respectively, while regular font denotes scalars. $\boldsymbol{A}^T$, $\boldsymbol{A}^H$, and $\boldsymbol{A}^{-1}$ are used for the transpose, transpose conjugate, and

inverse of matrix $\boldsymbol{A}$. Finally, $\|\boldsymbol{A}\|_F$ is the Frobenius norm of matrix $\boldsymbol{A}$.

CHAPTER 2

Concurrent Synchronization and Channel Estimation for Interference Alignment Using Zadoff-Chu Sequence

2.1 Overview

Interference alignment, a multi-antenna precoding technique, has been proven to enable concurrent data communications with a K-user interference channel, assuming accurate channel estimates and full synchronization [CJ08, GCJ08]. In theory, IA shows significant increase in the sum throughput of the network. However, synchronizing the radios and obtaining global channel information have to be done before the aggregated throughput improvement of IA can be realized. The synchronization includes correcting the frequency offset and the timing offset between each pair of transmitter (TX) and receiver (RX). As for the global channel information, not only the channel between a receiver and its desired transmitter needs to be estimated, but also the channels associated with interfering transmitters. Sometimes, it could also be the covariance matrix of the observed interference.

For traditional non-concurrent communication systems with no co-channel interference, the synchronization and channel estimation have been well studied. One intuitive synchronization approach is via correlating the received signal with a local copy of a known pilot sequence, which yields a peak when they are aligned. But the approach may fail because the correlation peak will not be as prominent with the presence of carrier frequency offset (CFO). To work around it, the authors of [SC97] proposed to correlate two consecutive identical pilot sequences from the received signal to identify the onset of the packet transmission, which is robust against CFO. In addition, the CFO can be estimated from the

repetitive pilot structure for further correction. This proposed method has been adopted by IEEE 802.11 standards for initial acquisition. By introducing modulation to the pilot sequences, [MBL03] has improved its performance with respect to timing offset estimation. As for channel estimation, various estimators, i.e. least squares (LS) and minimum mean squared error (MMSE) channel estimators [VES95,ESB98,LCS98], were proposed to provide accurate channel estimates assuming only additive white Gaussian noise (AWGN).

However, before IA succeeds in coordinating all nodes and eliminating the interference, the synchronization and channel estimation generally have to be done with the presence of the co-channel interference. Even if the interference is orthogonalized via a round-robin mechanism whereby the transmitters take turns to transmit [LGH14], it takes a tremendous amount of time. On the one hand, the long duration of the initial acquisition process, which linearly grows with the number of transmitters, ultimately reduces the IA gain and makes IA vulnerable to the time-varying channel. On the other hand, in general, not all transmitter are strong interference sources, and treating them equally is a wasteful utilization of the timing resources. Thus, a concurrent synchronization and channel estimation method robust to interference is desired for advanced techniques like IA.

Recently, Zadoff-Chu (ZC) sequences [Chu72] have attracted researchers' attention and been adopted in the 3GPP LTE systems for synchronization and cell search [MEJ09]. By exploiting the perfect cyclic auto-correlation property of ZC sequences, researchers also have developed fine timing offset estimation methods [WW09, WW11]. In [GML14], the authors have found that ZC sequences are robust against CFO, if a conjugate pair of ZC sequences is utilized along with cyclic prefix (CP) and cyclic suffix (CS). The CFO is divided into a fractional part and an integer part, each being estimated individually. Similar to [SC97], the timing offset is obtained via correlation following the estimation and correction of the CFO.

In this work, we address the synchronization and channel estimation challenges associated with enabling multiple concurrent communication links via interference alignment. A practical mechanism using conjugate pairs of ZC sequences was proposed for achieving the required synchronization and channel estimation concurrently. Starting from the expression

of the maximum likelihood (ML) function for joint timing and frequency synchronization in general situations, we realize the optimal ML estimator is practically infeasible for being too costly in terms of computation, though robust against co-channel interference. Then, the unique properties of ZC sequences and the proposed structure of conjugate ZC sequence pairs are fully exploited to reduce the implementation complexity. Hence, the concurrent synchronization and channel estimation are achieved through two one-dimensional searches other than one full search in a two-dimensional space.

The remainder of this chapter is organized as follows. Section 2.2 presents the network we consider and its corresponding signal models. In section 2.3, we derive the likelihood function of the unknown frequency and timing offsets as well as the channels. The optimal estimators under the ML criterion are also found to be impractical for being too complex as a two-dimensional search. In section 2.3, to address the problem, a pair of conjugate ZC sequences is proposed, and low-complexity approximate ML estimators for synchronization and channel estimation are derived. The experimental validation of the proposed algorithm is shown in the following section 2.5 and section 2.6. In the end, the summary is given in section 2.7.

2.2 Signal and System Model

Consider an IA network with K users that are randomly distributed within a circle as shown in Fig. 2.1. Through a network-wise frame synchronization mechanism, i.e. beacon and time stamp, all the transmitters are capable of sending signal frames with the pilot at the beginning. These pilots are received by each receiver after experiencing different channels, propagation delays, as well as frequency offsets. Given the received pilots, the receiver tries to achieve reliable acquisition, which includes estimating the frequency and timing offsets and the channel responses. To avoid confusion, it should be noted that different transmitters actually transmit different pilots according to an agreement a priori. In addition, we focus on a single-input multiple-output (SIMO) multipath channel for easier derivation. The extension to MIMO channel cases presents no fundamental hurdles if the orthogonalized sequences are

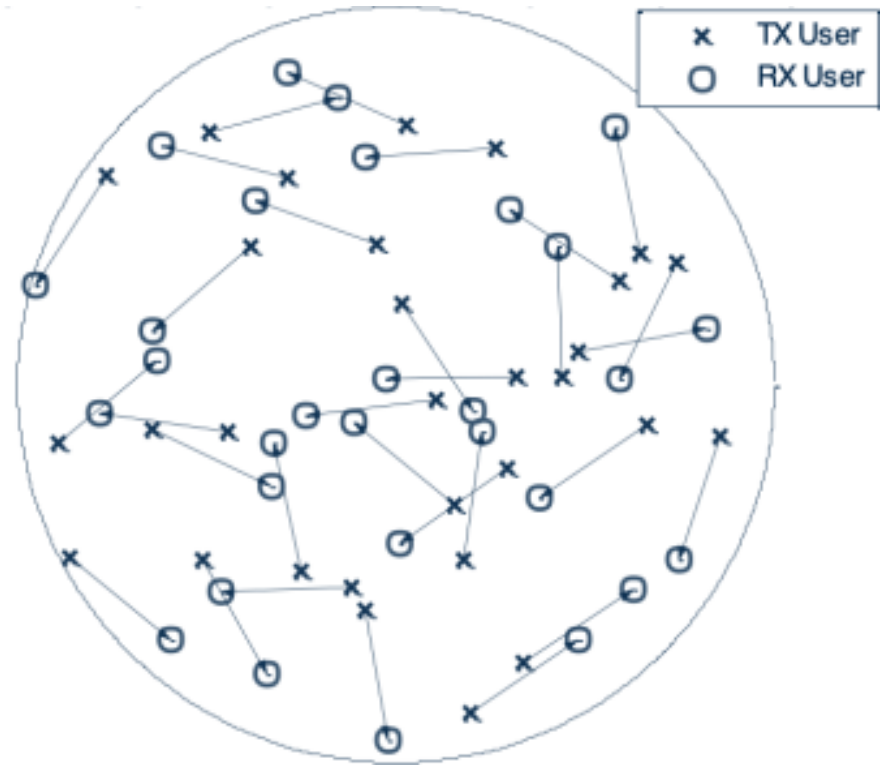

Figure 2.1: Topology of an IA network with K users .

assigned to different transmit antennas, which will be further discussed in section 2.4.

Given the assumptions above, the samples received by an arbitrary receiver with M antennas can be given as

$$\boldsymbol{x}(n) = \exp\left(j2\pi f n\right)\boldsymbol{H}\boldsymbol{s}(n-\tau) + \boldsymbol{v}(n), \quad n = 0, 1, 2, \ldots, N-1, \tag{2.1}$$

where

$$\boldsymbol{H} \triangleq \begin{bmatrix} \boldsymbol{h}_0 & \boldsymbol{h}_1 & \ldots & \boldsymbol{h}_{P-1} \end{bmatrix} \in \mathbb{C}^{M\times P} \tag{2.2}$$

is the SIMO multipath channel with P maximal number of taps,

$$\boldsymbol{s}(n) \triangleq \begin{bmatrix} s(n) & s(n-1) & \ldots & s(n-P+1) \end{bmatrix}^T \in \mathbb{C}^{P\times 1}, \tag{2.3}$$

is a subset of the known pilot sequence that contributes to $\boldsymbol{x}(n)$, and the L-length pilot sequence $\{s(n)\}$ is defined to take value 0 when $n \notin [0, L-1]$. The unknown carrier frequency offset and timing offset between the transmitter and receiver normalized by the sampling rate

are denoted by f and τ respectively. We model $\boldsymbol{v}(n) \in \mathbb{C}^{M\times 1}$ as the co-channel interference plus noise observed by the receiver, which may come from the peer transmitters or from the devices outside of the IA network. $\boldsymbol{v}(n)$ is assumed to be a temporally uncorrelated circularly symmetric complex Gaussian vector process with an unknown covariance matrix $\boldsymbol{Q}$.

2.3 Optimum Synchronization and Channel Estimation

2.3.1 Maximum Likelihood Estimators

Given the samples received by an arbitrary receiver $\boldsymbol{x(n)}$ and the assumption that the interference plus noise is Gaussian, the conditional probability function for receiving $\boldsymbol{x}(n)$ can be found to be

$$\begin{aligned} f\left(\boldsymbol{x}(n)|\tau, f, \boldsymbol{H}, \boldsymbol{Q}\right) = \frac{1}{\pi^M|\boldsymbol{Q}|}\exp\Big\{ &-\left[\boldsymbol{x}(n) - \exp\left(j2\pi fn\right)\boldsymbol{H}\boldsymbol{s}(n-\tau)\right]^H \boldsymbol{Q}^{-1} \\ &\times\left[\boldsymbol{x}(n) - \exp\left(j2\pi fn\right)\boldsymbol{H}\boldsymbol{s}(n-\tau)\right]\Big\} \end{aligned} \tag{2.4}$$

Considering the multiple received samples for $n = 0, 1, 2, \ldots, L+P+1$ and $\boldsymbol{v}(n)$ is temporally uncorrelated, the normalized log-likelihood function of the received sequence is derived as

$$\begin{aligned} C\left(\tau, f, \boldsymbol{H}, \boldsymbol{Q}\right) &= \frac{1}{L+P-1}\sum_{n=0}^{L+P+1}\log\left[f\left(\boldsymbol{x}(n)|\tau, f, \boldsymbol{H}, \boldsymbol{Q}\right)\right] \\ &= -\ln|\boldsymbol{Q}| - \frac{1}{L+P-1}\mathrm{Tr}\Bigg\{\boldsymbol{Q}^{-1}\sum_{n=0}^{L+P-1}\left[\boldsymbol{x}(n) - \exp\left(j2\pi fn\right)\boldsymbol{H}\boldsymbol{s}(n-\tau)\right] \\ &\quad\times\left[\boldsymbol{x}(n) - \exp\left(j2\pi fn\right)\boldsymbol{H}\boldsymbol{s}(n-\tau)\right]^H\Bigg\}. \end{aligned} \tag{2.5}$$

Using the method from [SS98], we take the partial derivative of $C\left(\tau, f, \boldsymbol{H}, \boldsymbol{Q}\right)$ over $\boldsymbol{Q}$ and obtain the ML estimate of $\boldsymbol{Q}$, the covariance matrix of $\boldsymbol{v}(n)$, as

$$\begin{aligned} \hat{\boldsymbol{Q}}_{ML} = \frac{1}{L+P-1}\sum_{n=0}^{L+P-1}&\left[\boldsymbol{x}(n) - \exp\left(j2\pi fn\right)\boldsymbol{H}\boldsymbol{s}(n-\tau)\right] \\ &\times\left[\boldsymbol{x}(n) - \exp\left(j2\pi fn\right)\boldsymbol{H}\boldsymbol{s}(n-\tau)\right]^H. \end{aligned} \tag{2.6}$$

By inserting (2.6) into (2.5), we see that the ML estimates of $\tau, f, \boldsymbol{H}$ should be solutions of the following minimization problem as

$$\begin{aligned}\hat{\tau}_{ML}, \hat{f}_{ML}, \hat{\boldsymbol{H}}_{ML} = \underset{\tau,f,\boldsymbol{H}}{\arg\min} \Bigg| \sum_{n=0}^{L+P-1} &[\boldsymbol{x}(n) - \exp(j2\pi fn)\boldsymbol{H}\boldsymbol{s}(n-\tau)] \\ &\times [\boldsymbol{x}(n) - \exp(j2\pi fn)\boldsymbol{H}\boldsymbol{s}(n-\tau)]^H \Bigg|,\end{aligned} \tag{2.7}$$

which can be reformulated into matrix form as

$$\hat{\tau}_{ML}, \hat{f}_{ML}, \hat{\boldsymbol{H}}_{ML} = \underset{\tau,f,\boldsymbol{H}}{\arg\min} \left| [\boldsymbol{X} - \boldsymbol{H}\boldsymbol{S}(\tau)\boldsymbol{D}(f)] [\boldsymbol{X} - \boldsymbol{H}\boldsymbol{S}(\tau)\boldsymbol{D}(f)]^H \right|, \tag{2.8}$$

where the denotation includes

$$\boldsymbol{X} \triangleq \begin{bmatrix} \boldsymbol{x}(0) & \boldsymbol{x}(1) & \dots & \boldsymbol{x}(L-1) \end{bmatrix} \in \mathbb{C}^{M\times L}, \tag{2.9}$$

$$\begin{aligned}\boldsymbol{S}(\tau) &\triangleq \begin{bmatrix} \boldsymbol{s}(\tau) & \boldsymbol{s}(\tau+1) & \dots & \boldsymbol{s}(\tau+L+P-2) \end{bmatrix} \in \mathbb{C}^{P\times(L+P-1)} \\ &= \begin{bmatrix} s(\tau) & s(\tau+1) & \dots & s(\tau+L+P-2) \\ s(\tau-1) & s(\tau) & \dots & s(\tau+L+P-3) \\ \vdots & \vdots & \ddots & \vdots \\ s(\tau-P+1) & s(\tau-P+2) & \dots & s(\tau+L-1) \end{bmatrix},\end{aligned} \tag{2.10}$$

$$\boldsymbol{D}(f) \triangleq \begin{bmatrix} 1 & 0 & \dots & 0 \\ 0 & \exp(j2\pi f) & \dots & 0 \\ \vdots & \vdots & \ddots & \vdots \\ 0 & 0 & \dots & \exp(j2\pi f(L+P-2)) \end{bmatrix} \in \mathbb{C}^{(L+P-1)\times(L+P-1)}. \tag{2.11}$$

Regarding the matrix in (2.8), the following inequality holds [JDP17]

$$[\boldsymbol{X} - \boldsymbol{H}\boldsymbol{S}(\tau)\boldsymbol{D}(f)] [\boldsymbol{X} - \boldsymbol{H}\boldsymbol{S}(\tau)\boldsymbol{D}(f)]^H \succeq \boldsymbol{R}_X - \boldsymbol{R}_{XS}(\tau,f)\boldsymbol{R}_S^{-1}(\tau)\boldsymbol{R}_{XS}^H(\tau,f), \tag{2.12}$$

where $A \succeq B$ implies $A - B$ is positive semi-definite, and $\boldsymbol{R}_S(\tau)$, $\boldsymbol{R}_X$, $\boldsymbol{R}_{XS}(\tau,f)$ respectively denote

$$\boldsymbol{R}_S(\tau) \triangleq \boldsymbol{S}(\tau)\boldsymbol{S}^H(\tau) \in \mathbb{C}^{P\times P}, \tag{2.13}$$

$$\boldsymbol{R}_X \triangleq \boldsymbol{X}\boldsymbol{X}^H \in \mathbb{C}^{M\times M}, \tag{2.14}$$

$$\boldsymbol{R}_{XS}(\tau,f) \triangleq \boldsymbol{X}\boldsymbol{D}^H(f)\boldsymbol{S}^H(\tau) \in \mathbb{C}^{M\times P}. \tag{2.15}$$

The condition for the equality to hold in (2.12) is also shown to be

$$\hat{\boldsymbol{H}}_{ML} = \boldsymbol{R}_{XS}(\tau, f)\boldsymbol{R}_S^{-1}(\tau), \tag{2.16}$$

which is exactly the ML estimator of the channel H for minimizing the determinant in (2.8). Therefore, we can obtain the ML estimators of the frequency offset f and the timing offset τ by further minimizing the right hand side of (2.12) as

$$\hat{\tau}_{ML}, \hat{f}_{ML} = \arg\min_{\tau,f} \left| \boldsymbol{R}_X - \boldsymbol{R}_{XS}(\tau, f)\boldsymbol{R}_S^{-1}(\tau)\boldsymbol{R}_{XS}^H(\tau, f) \right|. \tag{2.17}$$

In the case of a flat fading channel, i.e. $P = 1$, we can simplify (2.17) as

$$\begin{aligned} \hat{\tau}_{ML}, \hat{f}_{ML} &= \arg\min_{\tau,f} \left| \boldsymbol{I} - \boldsymbol{R}_X^{-1}\boldsymbol{R}_{XS}(\tau, f)\boldsymbol{R}_S^{-1}(\tau)\boldsymbol{R}_{XS}^H(\tau, f) \right| \\ &= \arg\min_{\tau,f} 1 - \boldsymbol{R}_S^{-1}(\tau)\boldsymbol{R}_{XS}^H(\tau, f)\boldsymbol{R}_X^{-1}\boldsymbol{R}_{XS}(\tau, f) \\ &= \arg\max_{\tau,f} \boldsymbol{R}_{XS}^H(\tau, f)\boldsymbol{R}_X^{-1}\boldsymbol{R}_{XS}(\tau, f), \end{aligned} \tag{2.18}$$

where the identity $|\boldsymbol{I} + \boldsymbol{AB}| = |\boldsymbol{I} + \boldsymbol{BA}|$ is used from the first to the second step, and $\boldsymbol{R}_S(\tau)$ is assumed to be almost a constant scalar within the observation window to yield the ultimate expression much simpler than (2.17).

2.3.2 Robustness against Co-channel Interference

A numerical example is presented in Fig. 2.2 to show the robustness of the ML estimators in (2.18) against co-channel interference. The signal received by a four-antenna receiver is composed of the desired signal and three interferers. The desired signal is a binary Gold sequence [Gol67] 15 dB over the noise floor, which is optimal for spread spectrum multiplexing. The three interferers have power 10dB, 10dB, and 20 dB higher than the desired signal. The channel is assumed to be flat fading with single-tap impulse response, hence (2.18) is evaluated rather than (2.17). In Fig. 2.2, even with the z-axis in dB scale, a prominent peak can be identified indicating the true frequency and timing offsets.

Due to the proximity of the co-channel peer nodes, the interference might be much stronger than the desired signal such as the case considered in Fig. 2.2. Hence, using the

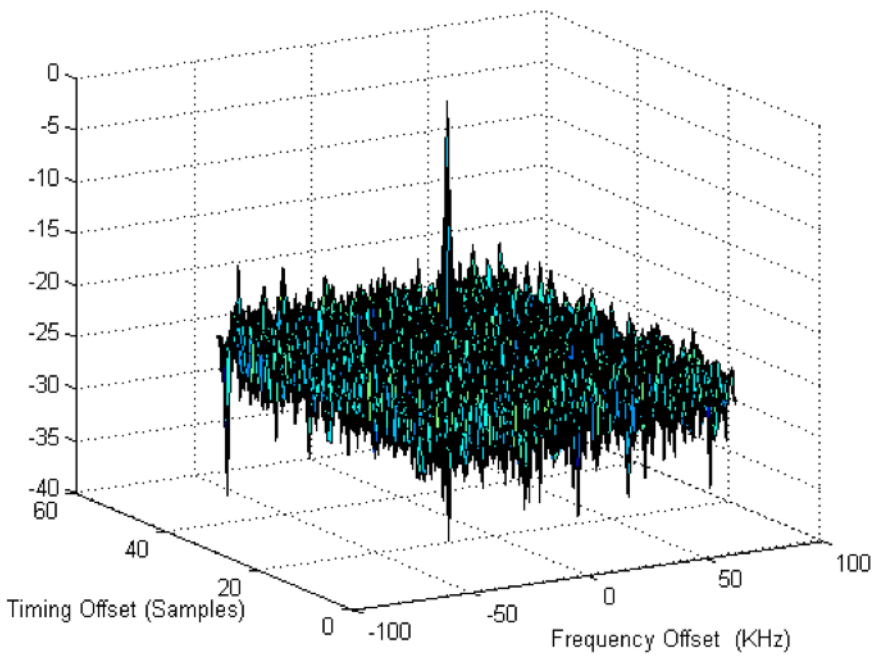

Figure 2.2: The two dimensional function in (2.18) under co-channel interference.

processing gain of the sequence alone is insufficient to suppress the interference and achieve reliable synchronization and channel estimation. However, the interference is spatially correlated in general, and the multiple antennas, each assumed to be equipped on the radio, can actually help with filtering such interference. That is why the derived two-dimensional search functions (2.17) and (2.18) both incorporate the term $\boldsymbol{R}_X^{-1}$ to provide the robustness against co-channel interference.

2.3.3 Extremely High Complexity

Although it has be shown that the ML estimators for carrier frequency offset f and timing offset τ are robust against co-channel interference, directly implementing these estimators on real hardware is way too costly in terms of computation. Unlike evaluating a close-form expression as in [SC97, MBL03], the computational complexity of these ML estimators mainly results from the searching of the peak in a two-dimensional function, which inherently

is solving a multivariate optimization problem. While in the case of flat fading channel, the function is (2.18) is greatly simplified, the two-dimensional search is required.

2.4 A Practical Method Using Zadoff-Chu Sequences

2.4.1 Zadoff-Chu Sequence Based Pilots

A Zadoff-Chu sequence, also referred to as Chu sequence or Frank-Zadoff-Chu sequence [ZF13], is a complex-valued sequence applied to radio signals, whose expression is given by

$$s(n) = \begin{cases} \exp\left(\frac{j2\pi n(n+1)}{L}\right), & \text{if } L \text{ is odd,} \\ \exp\left(\frac{j2\pi n^2}{L}\right), & \text{if } L \text{ is even,} \end{cases} \tag{2.19}$$

where L is the length of the sequence, the sample index $n = 0, 1, \ldots, L-1$, and the parameter r is co-prime with L.

The most significant property of the ZC sequence is the perfect cyclic auto-correlation function $\rho(\delta)$ with the cyclic shift τ, which is essentially a Kronecker delta function as

$$\rho(\tau) = \sum_{n=0}^{L-1} s(n)s^*((n-\tau) \bmod L) = \begin{cases} L, & \text{if } \tau = kL \quad \forall k \in \mathbb{Z}. \\ 0, & \text{otherwise.} \end{cases} \tag{2.20}$$

Another important property is the timing-frequency offset ambiguity. A cyclically shifted ZC sequence can be given as

$$s((n-\tau) \bmod L) = \begin{cases} \exp\left(\frac{j\pi r(\tau^2-\tau)}{L}\right) \exp\left(\frac{-j2\pi r\tau}{L}\right) s(n), & \text{if } L \text{ is odd,} \\ \exp\left(\frac{j\pi r\tau^2}{L}\right) \exp\left(\frac{-j2\pi r\tau}{L}\right) s(n), & \text{if } L \text{ is even,} \end{cases} \tag{2.21}$$

where, in either case, the cyclic time shift τ amounts to a modulation of the frequency offset $\frac{-r\tau}{L}$. Besides, ZC sequence has many other useful properties that are not directly related to our work, therefore not listed here. Without loss of generality, in the remainder of this chapter, we assume an odd length L for the convenience of discussion, unless stated otherwise.

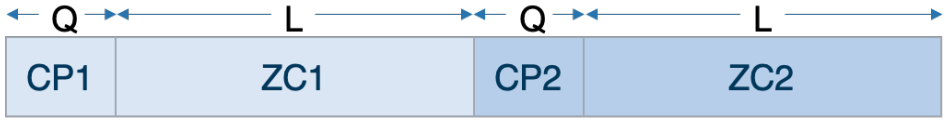

Figure 2.3: The pilot structure based on conjugate pairs of Zadoff-Chu sequences.

Considering the properties of the ZC sequence, we propose a pilot structure to be used with the maximum likelihood estimators such as (2.17) and (2.18). A pair of conjugate ZC sequences is adopted as illustrated in Fig. 2.3. The whole pilot is composed of two halves, each being a L-length ZC sequence with a Q-sample cyclic prefix (CP). The second half is the conjugate of the first half, and follows the first half in timing series. The CP is attached for two reasons. First, it is a guard interval rendering an inter-symbol interference (ISI) free zone as long as it is longer than the channel dispersion. Second, it transforms a timing offset to a cyclic shift, then we are able to exploit the ZC sequence properties on timing. Also note that different TX nodes use ZC sequences with different parameters r, and this can be achieved using ID assignment mechanism.

2.4.2 Simplified Maximum Likelihood Synchronization

Let us focus on the first half part of the pilot and see how it can simplify the maximum likelihood estimation problem. Similar to Fig. 2.2 where the pilot is a binary Gold sequence, Fig. 2.4 presents the plot of the objective function from (2.18) when the first half of the ZC pilot is applied. In comparison, instead of having a single prominent peak, we see a ridge because of the the timing frequency offset ambiguity of the ZC sequence. Any combination of the timing offset and frequency offset along a line yields the same value in evaluating (2.18). This can be proved by applying (2.21) to the term $\boldsymbol{R}_{XS}$ defined in (2.15), which is

$$\begin{aligned}\boldsymbol{R}_{XS}(\tau, f) &= \boldsymbol{X}\boldsymbol{D}^H(f)\boldsymbol{S}^H(\tau) \\ &= \boldsymbol{X}\boldsymbol{D}^H(f)\boldsymbol{D}^H\left(-\frac{r}{L}\tau\right)\boldsymbol{S}^H(0) \\ &= \boldsymbol{X}\boldsymbol{D}^H\left(f - \frac{r}{L}\tau\right)\boldsymbol{S}^H(0).\end{aligned} \tag{2.22}$$

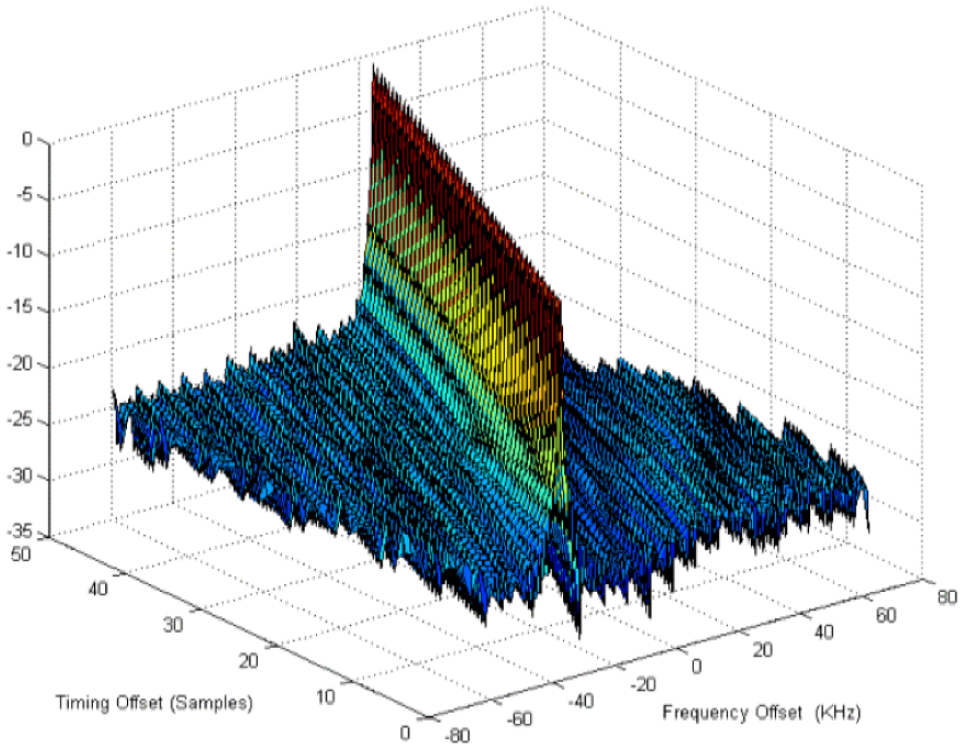

Figure 2.4: The two dimensional function in (2.18) using Zadoff-Chu sequence.

So, we can introduce a dummy variable

$$\zeta \triangleq f - \frac{r}{L}\tau, \tag{2.23}$$

then $\boldsymbol{R}_{XS}$ can be rewritten as a function of ζ as

$$\boldsymbol{R}_{XS}(\zeta) = \boldsymbol{X}\boldsymbol{D}^H(\zeta)\boldsymbol{S}^H(0). \tag{2.24}$$

As a result, the synchronization problem (2.18) is reduced to an optimization problem over a single variable as

$$\hat{\zeta}_{ML} = \arg\max_{\zeta} \boldsymbol{R}_{XS}^H(\zeta)\boldsymbol{R}_X^{-1}\boldsymbol{R}_{XS}(\zeta). \tag{2.25}$$

The above derivation indicates that, due to the ambiguity property of the ZC sequence, the timing offset τ and the frequency offset f cannot be estimated separately. Any combination of τ and f that results in identical ζ makes no difference regarding the maximum likelihood estimation.

Although, it sounds pretty bad for not being able to differentiate τ and f, please don't forget the second half of the ZC pilot, and such ambiguity actually turns out to be very helpful in reducing the complexity. Following the same derivation as the first half, another dummy variable can be introduced for the second half of the pilot as

$$\eta \triangleq f + \frac{r}{L}\tau, \tag{2.26}$$

where the minus sign is replaced by a plus sign, because the equivalent parameter for the second half is $-r$. Correspondingly, the optimization problem is also reduced to

$$\hat{\eta}_{ML} = \arg\max_{\eta} \boldsymbol{R}_{XS}^{H}(\eta)\boldsymbol{R}_{X}^{-1}\boldsymbol{R}_{XS}(\eta). \tag{2.27}$$

Given the optimal estimates of ζ and η respectively obtained from the first and second halves of the ZC pilot, the estimates of timing and frequency offsets can be calculated using

$$\hat{f}_{ML} = \frac{\hat{\zeta}_{ML} + \hat{\eta}_{ML}}{2}, \tag{2.28}$$

$$\hat{\tau}_{ML} = \frac{\hat{\eta}_{ML} - \hat{\eta}_{ML}}{2} \times \frac{L}{r}. \tag{2.29}$$

This can be interpreted as finding the intersection point of two straight lines that correspond to the two ridges for a pair of ZC sequences $s_r(n)$ and $s_r^*(n)$. The slopes of the two lines are $\frac{r}{L}$ and $-\frac{r}{L}$, and the intercepts are $\hat{\zeta}_{ML}$ and $\hat{\eta}_{ML}$. The two lines cross each other at the point $\left(\hat{\tau}_{ML}, \hat{f}_{ML}\right)$. Now, we see the benefit of utilizing a pair of conjugate ZC sequences: the extremely challenging two-dimensional optimization problem is simplified into two one-dimensional searches, which makes it a practical synchronization method robust against interference.

2.4.3 Maximum Likelihood Channel Estimation

Recall the general maximum likelihood channel estimator (2.16), which is derived assuming an arbitrary pilot. In the case of using ZC sequence based pilot, per its perfect auto-correlation property, we have

$$\boldsymbol{R}_S(\tau) = \boldsymbol{S}(\tau)\boldsymbol{S}^H(\tau) = L\boldsymbol{I}, \tag{2.30}$$

where $\boldsymbol{R}_S(\tau)$ is the term defined in (2.13), and $\boldsymbol{I}$ denotes an identity matrix. Then, the channel estimator becomes

$$\begin{aligned}\hat{\boldsymbol{H}}_{ML} &= \boldsymbol{R}_{XS}(\tau, f)\boldsymbol{R}_S^{-1}(\tau) \\ &= \frac{1}{L}\boldsymbol{X}\boldsymbol{D}^H(f)\boldsymbol{S}^H(\tau).\end{aligned} \tag{2.31}$$

Practically, the channel is estimated by first compensating the carrier frequency of the received samples using the estimated frequency offset $\hat{f}_{ML}$, and then conducting a cross-correlation of the compensated samples with a local ZC sequence template.

2.5 Validating Synchronization under Co-channel Interference

2.5.1 Experimental Setup

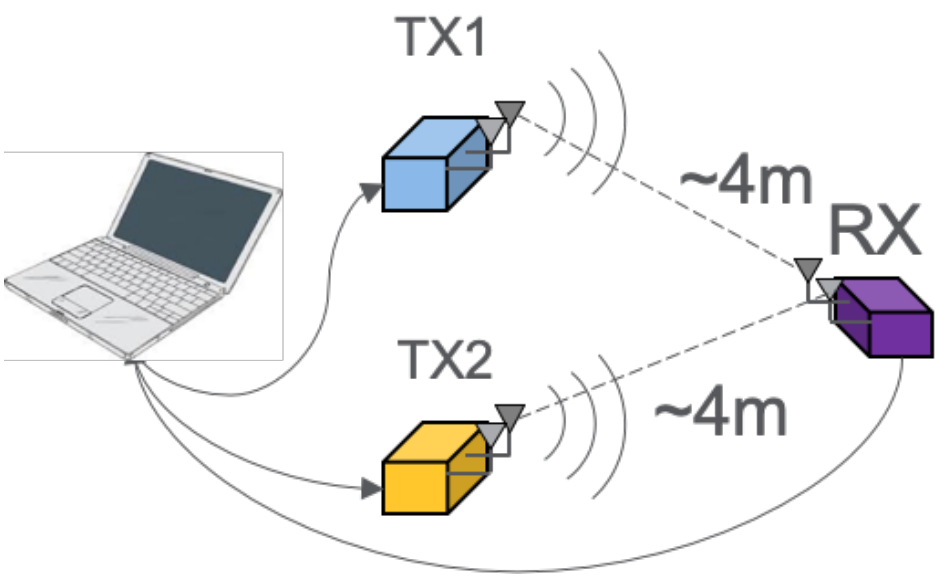

Figure 2.5: The experimental setup for validating synchronization using Zadoff-Chu sequences.

Here, the experiment we conducted for verifying our proposed synchronization algorithm is presented. Fig. 2.5 shows the experiment setup, where there are two transmitters and one receiver. The transmitter TX1 in light blue is the desired transmitter, while the other one is the interference node. Both of the two transmitters are placed approximately 4 meters away

from the receiver, resulting in a signal to interference plus noise ratio (SINR) around 0 dB. Each node is a MIMO radio equipped with 2 antennas. They are configured to operate in the 2.4 GHz frequency band with a 1.25 MHz bandwidth. A laptop is connected to all the nodes via Ethernet cables for data transferring and post-processing. The nodes are running based on their own crystal and clock, so the carrier frequency offsets exist with a typical value of 5 ppm.

2.5.2 With and Without Inteference

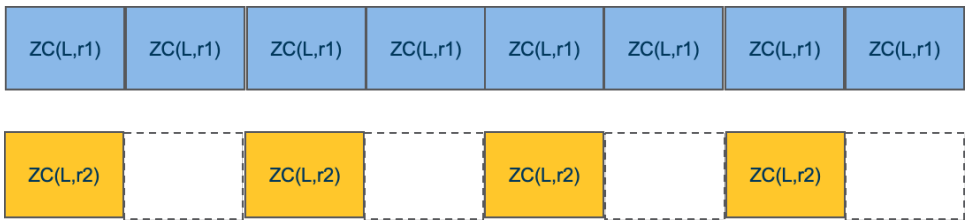

Figure 2.6: The signaling pattern of the transmitters.

The radios are programmed to transmit their pilots following the format as illustrated in Fig. 2.6. Each block is one ZC sequence based pilot as proposed in previous section. It can be noticed that the two transmitters are assigned with two different parameters, $r1$ and $r2$, for their ZC pilots. The desired transmitter keeps transmitting its pilot, yet the interference node only sends out its pilot in every other slot. By doing this, we can study the performance of our proposed synchronization algorithm in two cases: one with the presence of the co-channel interference and one without. When there is no interference, the performance is considered as a reference for comparison. In addition, the experiment is repeated with different ZC sequence lengths as the longer sequence has larger processing gain, which helps with rejecting interference as well.

2.5.3 Synchronization Results

The experimental results are presented in Fig. 2.7. The horizontal axis is the length of the ZC sequence, and the vertical axis is the standard deviation of the frequency offset error in dB

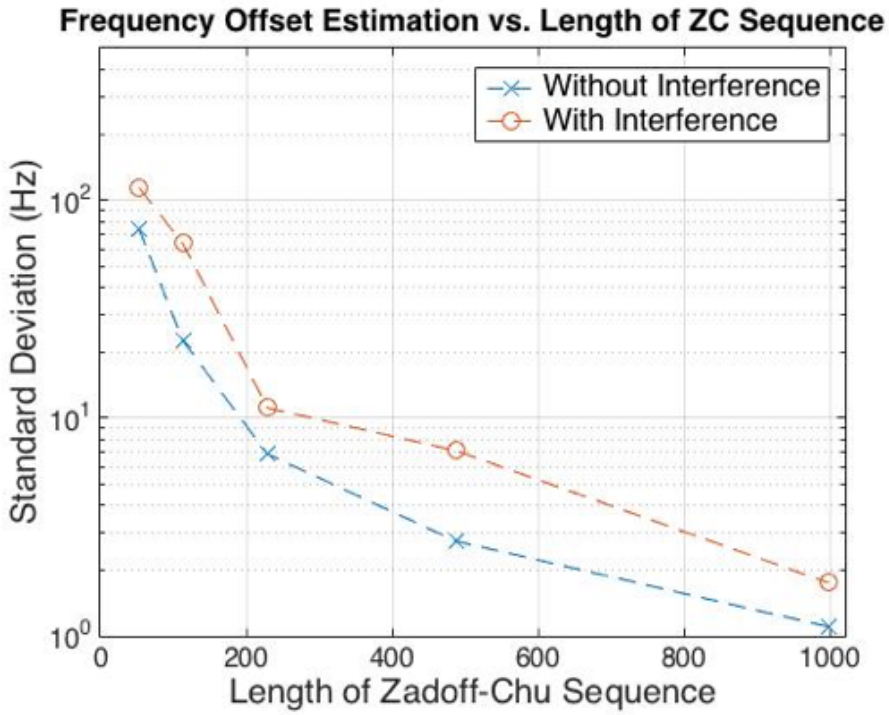

Figure 2.7: The frequency offset estimation results given different ZC sequence lengths.

scale with a unit of Hz. There are two curves in this figure, where the blue curve with crosses represents the case without interference, and the red curve with circles is for the case with interference. Comparing the two curves, we see the red one is slightly higher than the blue one and the performance degradation is successfully suppressed using our proposed algorithm. In other words, even with the presence of the interference of the same power level, our proposed synchronization algorithm can still output an accurate result with affordable computational complexity. Another important observation from the experimental results in Fig. 2.7 is that the standard deviation can be further reduced by increasing the length of the ZC sequence. This implies that, even the interference power is higher, reliable synchronization can still be achieved by increasing the length of the ZC sequence. Practically, a length over 1000 is not necessary for achieving extremely accurate frequency offset estimation. There are usually other modules, such as phase lock loop (PLL), that follow to finely tune the carrier frequency and eliminate the residual frequency offset. Basically, the initial synchronization results from our experiment fall in the range that a typical PLL can track, and our proposed method is

effective in achieving synchronization under co-channel interference.

2.6 IA with Concurrent Synchronization and Channel Estimation

2.6.1 Experimental Setup

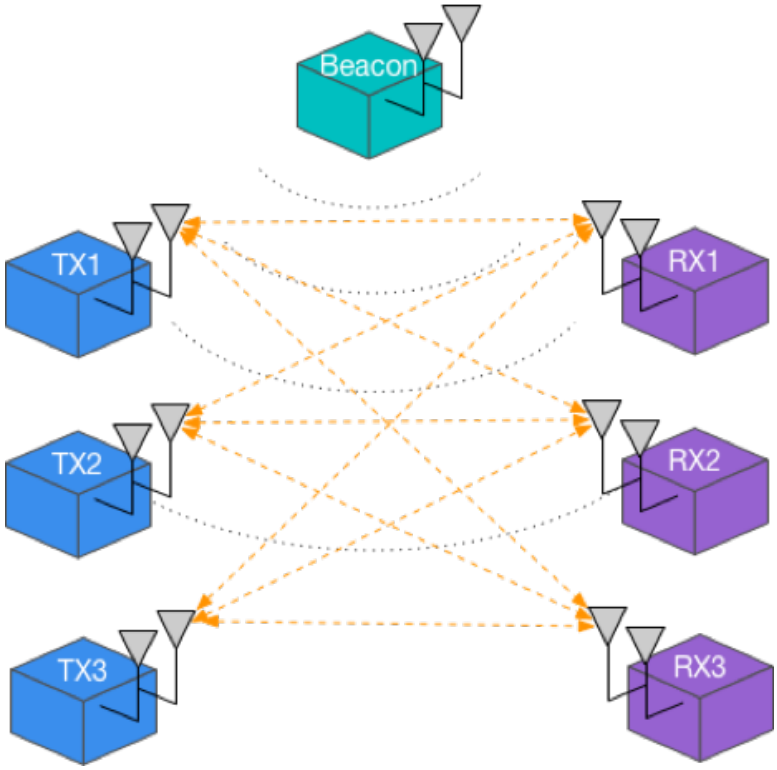

Figure 2.8: The experimental setup for studying the interference alignment performance.

Since the concurrent synchronization and channel estimation algorithm is proposed to help achieving interference alignment and many concurrent transmission schemes, we are also interested in how IA will perform using our proposed concurrent approach. Therefore, we have upgraded the experimental setup (see Fig. 2.5) and come up with a new setup for prototyping IA as shown in Fig. 2.8. In this setup, we have incorporated more 2×2 MIMO radios including three transmitters, three receivers, and one dedicated beacon node. All the radios form a classic IA setup with three pairs of users that has been extensively studied. The dedicated beacon node is utilized to achieve a rough frame synchronization for the whole

network. All the rest of the radios take actions under the coordination of the beacon node by being triggered by a specific beacon packet. Still, each radio is equipped with two antennas with the same configuration as in section 2.5.1.

2.6.2 Concurrent and Sequential Training

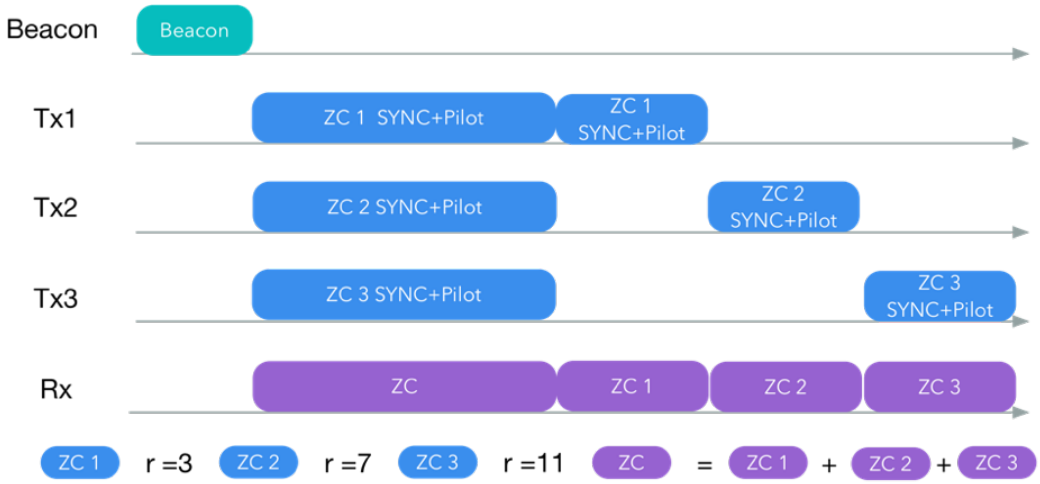

Figure 2.9: The signaling arrangement of transmitters in the 3-user interference alignment.

The radios transmit their pilots following the manner presented in Fig. 2.9. It can be seen that, after the beacon triggering, there are two training phases: a concurrent phase and a sequential phase. First comes the concurrent phase, where all three transmitters send their pilots roughly at the same time once the beacon packet is properly detected. As a result, our proposed approach should be utilized for dealing with their mutual interference. Right after the concurrent phase follows the sequential phase, where the transmitters take turns to transmit their training packets such that the received pilots are orthogonalized in time. Therefore, by windowing the received signal of interest, very accurate synchronization and channel estimation can be attained. This sequential phase is not only used to know the real channel, but also to help evaluating the upper limit of the IA network for comparison.

2.6.3 Calculating the IA solutions

Given the two sets of channel estimates individually obtained from the two training phases, we calculate the IA solutions using the iterative method devised in [PH09]. This method finds the precoding matrix set $\{\boldsymbol{P}_i\}$ by numerically solving an optimization problem that aims at minimizing the total interference leakage in the whole network. The optimization problem is formulated as follows:

$$\arg\min_{\boldsymbol{P}_i,\boldsymbol{C}_i} \sum_{j}^{K} \sum_{i\neq j} \left\| \boldsymbol{H}_{ji}\boldsymbol{P}_i - \boldsymbol{C}_j\boldsymbol{C}_j^H\boldsymbol{H}_{ji}\boldsymbol{P}_i \right\|_F^2, \tag{2.32}$$

where $\boldsymbol{H}_j i$ is the channel between the ith transmitter to the jth receiver, the matrix $\boldsymbol{C}_j$ is the orthonormal basis of the interference subspace for the jth receiver, and the subscript F indicates that the norm is the Frobenius norm. The procedure to solve (2.32) is summarized in Algorithm 1 as

Algorithm 1 The numerical solution to (2.32)

1: Initialize the set of precoders $\boldsymbol{P}_i$ randomly $\forall i$;

2: **repeat**

3: Choose the columns of $\boldsymbol{C}_j$ to be the eigen-vectors of

$$\sum_{i\neq j} \boldsymbol{H}_{ji}\boldsymbol{P}_i\boldsymbol{P}_i^H\boldsymbol{H}_{ji}^H$$

associated with the largest eigen-values $\forall j$;

4: Choose the columns of $\boldsymbol{P}_i$ to be the eigen-vectors of

$$\sum_{i\neq j} \boldsymbol{H}_{ji}^H \left(\boldsymbol{I} - \boldsymbol{C}_j\boldsymbol{C}_j^H\right) \boldsymbol{H}_{ji}^H$$

associated with the least eigen-values $\forall i$;

5: **until** $\{\boldsymbol{P}_i\}$ and $\{\boldsymbol{C}_j\}$ converge.

This algorithm has guaranteed convergence as each iteration monotonically reduces the non-negative objective function. And, compared with the closed-form solution in [CJ08],

it has a much higher flexibility for being applicable to a large-scale network. However, the objective function is non-convex in general, thus the search for the global optimum can fall into a local minimum. In addition, this algorithm assumes perfect channel state information, while the channel estimates in practice always come with some error due to noise. At low SNR, the performance is not as good as other algorithms that consider the noise.

As for the combiners on the receiver side, we simply adopt the well-known minimum mean squared error (MMSE) combining matrix, and the combining matrix for the i th receiver is given as

$$\boldsymbol{W}_i = \left(\sum_{j=1}^{K} \boldsymbol{H}_{ij} \boldsymbol{P}_j \boldsymbol{P}_j^H \boldsymbol{H}_{ij}^H + \sigma_i^2 \boldsymbol{I} \right)^{-1} \boldsymbol{H}_{ii} \boldsymbol{P}_i, \tag{2.33}$$

where σ_i^2 is the variance of the Gaussian noise observed at the ith receiver.

2.6.4 Interference Alignment Performance

Once the IA solutions, $\{\boldsymbol{P}_i\}$ and $\{\boldsymbol{W}_i\}$, are calculated using the algorithm introduced above, we can move forward and evaluate its corresponding performance. There are several metrics considered for assessing the performance of an IA network. The degrees of freedom (DoF) is in general the number of accessible signaling dimensions. For IA, it is equal to the number of data streams transmitted free of interference. Another metric is the bit error rate (BER), which is defined directly as the number of bit errors over the total number of transmitted bits. The outage probability is also used to reflect the reliability of the an IA network under varying conditions. The most broadly considered performance metric by the IA community, is the sum rate over the whole IA network, which is also going to be used by us. The sum rate approximates the true network-wise throughput given the SINR values for each link with practical meanings. More explicitly, the formula used to calculate the IA network sum rate R is given by

$$R = \sum_{i=1}^{K} \log_2 \left(1 + \frac{\boldsymbol{W}_i^H \boldsymbol{H}_{ii} \boldsymbol{P}_i \boldsymbol{P}_i^H \boldsymbol{H}_{ii}^H \boldsymbol{W}_i}{\boldsymbol{W}_i^H \left(\sum_{j \neq i}^{K} \boldsymbol{H}_{ij} \boldsymbol{P}_j \boldsymbol{P}_j^H \boldsymbol{H}_{ij}^H + \sigma_i^2 \boldsymbol{I} \right) \boldsymbol{W}_i} \right), \tag{2.34}$$

where the fractional term is exactly the effective SINR for each link incorporating both the precoding and combining matrices.

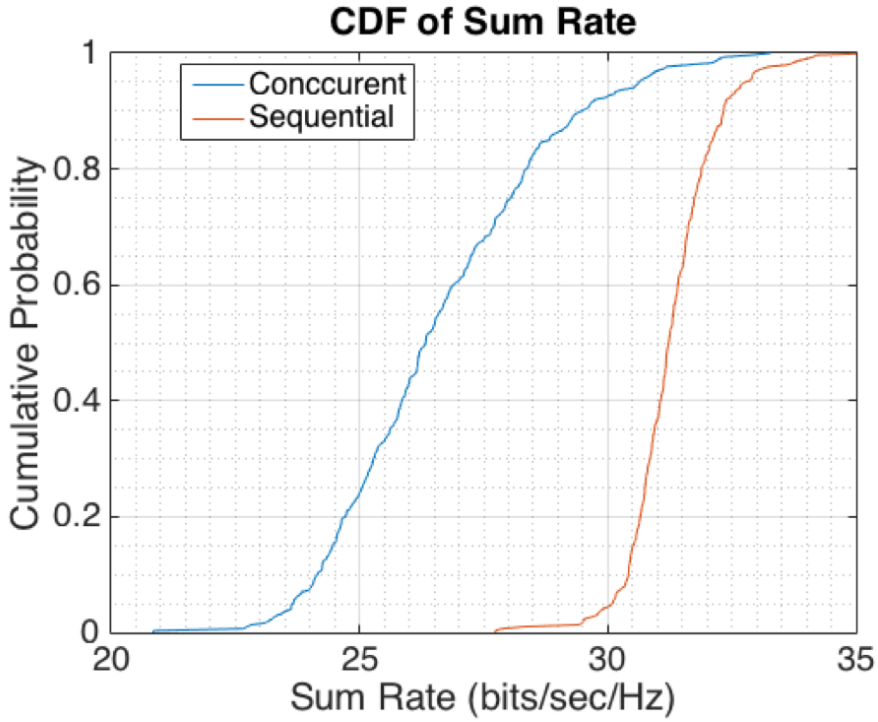

Figure 2.10: The cumulative distribution function of the sum rate for interference alignment with concurrent synchronization and channel estimation.

Then, the evaluated performance of IA with concurrent synchronization and channel estimation is shown in Fig. 2.10 as cumulative distribution function (CDF) curves of the sum rate. The horizontal axis is the sum rate calculated using (2.34) with a unit of bits/sec/Hz, and the vertical axis is the cumulative probability from 0 to 1. There are two CDF curves that correspond to the concurrent and sequential cases. It should be clarified that, for both curves, the channel matrices $\boldsymbol{H}_{ij}$ are measured using the pilots transmitted from the sequential phase for accuracy. The two curves differ from each other in the precoding and combining matrices, i.e. $\boldsymbol{P}_i$ and $\boldsymbol{W}_i$, derived from the concurrent and sequential phases accordingly.

The red curve from the sequential phase is taken as the upper limit approaching the theoretical IA performance. Here, the sum rate for the three links is above 30 bits/sec/Hz,

which means the rate each link can achieve on average is over 10 bits/sec/Hz. It amounts to deploying a modulation scheme with at least 1024 constellation points, and it can only be possible with the interference being eliminated. In comparison, the IA performance with concurrent synchronization and channel estimation represented by the blue curve is also pretty good. There is still a probability of 90% that the achievable sum rate is over 24 bits/sec/Hz. The interference level at each receiver is well suppressed, not as good as the sequential case though. Our proposed concurrent synchronization and channel estimation approach is further validated with the prototype IA network and the experimental results shown above.

2.7 Summary

Interference Alignment enables concurrent data transmission in a multi-user network via transmit and receive beamforming, and promises a much higher network sum throughput than the existing TDMA, FDMA, or CSMA based networks. However, in practice, synchronization and channel estimation need to be done with uncoordinated interference before achieving IA. Therefore, a concurrent algorithm with robustness against co-channel interference is needed. In this chapter, we begin with the derivation of the optimal maximum likelihood estimators. Although the requirement of suppressing interference is satisfied, they are impractical for being too computationally expensive. Then, we present a novel and practical approach that incorporates Zadoff-Chu sequences based pilots. The unique properties of ZC sequences are exploited to reduce the complexity of the ML approach. We can estimate the frequency and timing offsets through two one-dimensional searches rather than solving a complicated optimization problem over two variables. In addition, the same pilot is used to estimate the channel response and interference covariance matrix for each receiver. We conducted experiments regarding both the initial synchronization and the ultimate IA performances. Our proposed method is validated with the experimental results presented.

CHAPTER 3

Reciprocity Calibration of TDD MIMO Channel for Interference Alignment

3.1 Overview

Interference alignment, as introduced in the previous chapter, is a precoding technique that manages interference in multi-user wireless networks. Conventionally, handling the interference follows a conservative "cake-cutting" rule that each user is allocated an exclusive time slot or frequency bandwidth, e.g. TDMA and FDMA. IA, however, coordinates the concurrent co-channel signals in higher dimensions, and hence avoids significant interference on each receiver [CJ08]. Thus multiple communication links can be established at the same time using the same bandwidth. Ideally, the multiplexing gain attained through IA is proportional to the product of the total number of links and available signal dimensionality.

The high dimensionality of the signal is necessary to achieve IA. It can be obtained from the channel diversity either in time, frequency or space domains [BRB14, DZZ14, Jaf11]. The most reliable approach is through spatially separated antennas due to the popularity of the MIMO technique in recent decades. Each antenna sees a different channel realization as the signal arrives at the receiver via different propagation paths, yielding the multi-dimensionality. As in other MIMO applications, like beamforming and spatial multiplexing, the precoding and decoding of IA can also occur across the multiple antennas equipped on each node. In this chapter, we focus on MIMO based IA unless stated otherwise.

While IA shows promising benefits, translating them into practice is not easy. One of the most challenging issues is to acquire accurate channel state information on the transmitter

side for evaluating the precoding matrices. There are two main methods that can be used. One is feeding back the channel state information (CSI) estimated at the receivers to the transmitters as in [EH12,ELH12]. The other approach is utilizing the channel reciprocity. In time division duplex (TDD) systems, the forward and reverse transmissions occupy the same frequency band and take place sequentially, and the corresponding physical channels can be considered invariant within a short period of time, e.g. less than the channel coherence time. Therefore transmitters are enabled to learn the associated forward channels by receiving training sequences from the receivers during the reverse transmission. Assuming the channel being reciprocal, a large number of distributed IA algorithms have been developed [GCJ11, WV13, SBH10, KX10, FZF13].

Despite the fact that physical channels over the air are reciprocal in classical electromagnetism, such reciprocity cannot be directly extended to the interfaces between the digital basebands of transceivers. In addition to the physical channel, there are individual circuits for transmit and receive front ends [GSK05]. The difference between the two circuits actually results in channel non-reciprocity. When it comes to a multiple antenna system, the non-reciprocity is further complicated due to the mutual coupling effect that depends on the circuit connected to the antenna array [WWY15].

In practice, calibration is necessary to ensure the viability of techniques that assume channel reciprocity. Absolute calibration as in [BCK03] requires external devices to characterize the circuit solely, and hence is unfavorable in the context of a mobile communication network. The idea of relative calibration was first proposed in [GSK05], where only the calibration coefficients yielding reciprocal channels are targeted. This scheme has been extended to be used in various applications and network architectures [KJG10,SLY11,KGZ11,PSL13]. The latest progress can be found mostly related to massive MIMO. Similar to IA, via precoding, multiple access can be established between a base station (BS) equipped with a massive antenna array and many single-antenna user equipment (UE). In [SYA12], the Argos method was presented along with their many-antenna BS prototype, and the reciprocity calibration is performed partially on the BS side. For distributed massive MIMO systems, calibration

approaches were proposed in [RBP14, VRT14, VRE17].

In this research on relative calibration, it is assumed that there is no mutual coupling effect between elements in the antenna arrays, hence the calibration matrix is limited to have diagonal entries only. However, the mutual coupling effect generally exists and has been extensively studied since [GK83]. Whether the mutual coupling effect introduces channel asymmetry remains doubtful. On the one hand, in [JCK15], the authors claim that ignoring the off-diagonal elements in the relative calibration is reasonable for small-scale multiple-antenna systems. The mutual coupling effect is also considered to be symmetric in [PSL13]. On the other hand, it is suggested by [Bal16,Hui04,LHL09] that the mutual coupling behavior of an antenna array can differ fundamentally in the transmit and receive mode, and distinct methods for mutual coupling analysis and compensation have been devised.

There are a few attempts on real world implementation of IA. They either evaluate the precoding and combining matrices in a centralized way and designate them to each node [GRS11, GCG11, MFZ14], or let the the receivers feed the CSI back to all transmitters [LGH14]. However, to the best knowledge of the authors, there has been no trial on achieving IA as suggested in [GCJ11, WV13, SBH10] via utilizing channel reciprocity. Therefore, the channel non-reciprocity issue has not been considered as a significant practical impairment until now. In this chapter, for the first time, the channel non-reciprocity problem is studied in the context of IA with experimental validation.

In the rest of this chapter, we first review the subset of interference alignment algorithms that rely on the channel reciprocity in section 3.2. In section 3.3, we provide a model for TDD MIMO channels considering both RF gain mismatch and antenna mutual coupling, and show that the symmetry does not hold in general. Based on the channel modeling, a calibration method for all nodes in the IA network is proposed in section 3.4. Section 3.5 presents the experimental validation of the proposed calibration approach. In section 3.6, we discuss the impact of channel non-reciprocity on IA by examining the performance of a typical 3-user 2×2 network in our lab environment. Summary is given in section 3.7.

3.2 Channel Reciprocity Based Interference Alignment

3.2.1 The Concept of Interference Alignment

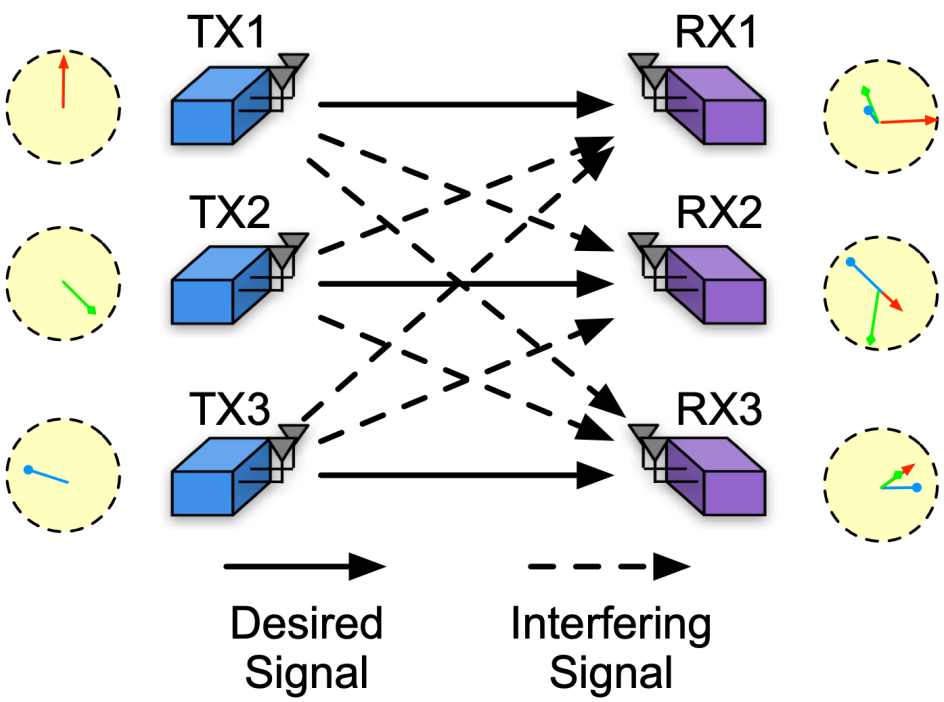

Figure 3.1: The conceptual illustration of IA in a 3-user interference channel with 2×2 MIMO radios.

Consider a network with K pairs of MIMO radios with N_{TX} and N_{RX} antennas. Fig. 3.1 shows an example with $K = 3$, $N_{TX} = N_{RX} = 2$, where the solid and dashed lines with arrows identify the desired and interfering signals respectively, and the coloured vectors with different heads on the two sides show the idea of aligning interference conceptually in a 2-D plane. In this network, the transmission takes place concurrently, and only the signal from the ith transmitter is desired at the ith receiver, while the others are regarded as interference. For the ith transmitter, it has a $N_s \times 1$ vector of symbols d_i to be transmitted, and the symbols are precoded with $N_{TX} \times N_s$ matrix $\boldsymbol{P}_i$ over all antennas. The channel between the ith transmitter and jth receiver is denoted by a $N_{RX} \times N_{TX}$ matrix $\boldsymbol{H}_{ji}$, which are assumed to be block fading. This assumption generally holds for a sub-carrier of orthogonal

frequency division multiplexing (OFDM) systems even under frequency-selective channels when designed properly. For the ith receiver, the received signal consists of three parts and is given by

$$y_i = \boldsymbol{H}_{ii}\boldsymbol{P}_i d_i + \sum_{j \neq i} \boldsymbol{H}_{ij}\boldsymbol{P}_j d_j + n_i \tag{3.1}$$

where the first term is the desired signal, the second term is the interfering signal, and n_i is the additive white Gaussian noise (AWGN) observed at receiver i.

The essence of IA is to find a set of precoders $\{\boldsymbol{P}_i\}$ such that, by applying $N_{RX} \times N_s$ linear combining matrices $\{\boldsymbol{W}_i\}$ at each receiver, the interference can be nulled out while the desired signal is retained. Mathematically, these conditions are represented by

$$\begin{aligned} &\boldsymbol{W}_i^H \boldsymbol{H}_{ij}\boldsymbol{P}_j = 0, \quad \forall j \neq i \\ &\operatorname{rank}\left(\boldsymbol{W}_i^H \boldsymbol{H}_{ii}\boldsymbol{P}_i\right) = N_s. \end{aligned} \tag{3.2}$$

To visually demonstrate the idea, in Fig. 3.1, the signals from different transmitters are represented as coloured vectors with different heads. With the cooperative precoding on the transmitter side, the interfering signals observed by any receiver are aligned to occupy only a fraction of the signal dimensionality. Thus, by projecting the received signal to the subspace perpendicular to the interference using the combining matrix, the desired signal can be decoded free from interference. Hence, multiple data links can be established over the interference channel to take full advantage of the degrees of freedom (DoF) of the network. Given high signal-to-noise ratio (SNR), the network sum capacity is achieved through IA [CJ08].

3.2.2 Calculating IA Solutions via Reciprocity

Calculating the precoders in a distributed manner requires accurate channel state information to be accessible for the transmitters. It includes not only the desired channel but also the interfering channels, because each transmitter is expected to minimize its interference leakage. A major category of approaches for obtaining the CSI at the transmitters is by exploiting the channel reciprocity.

By assuming the forward and backward channels being identical in a time-division duplexed network, the earliest IA strategy of finding the precoding matrices was proposed in [GCJ11]. The channel reciprocity allows the transmitters to be aware of the interference they generate in the forward channel by analyzing the interference they receive in the backward channel. It should be noted that all nodes essentially are transceivers with the capability of switching between transmit and receive modes, and the terms, transmitter and receiver, only refer to their roles in the IA network. Hence, the precoders $\{\boldsymbol{P}_i\}$ and the combiners $\{\boldsymbol{W}_i\}$ are updated iteratively to achieve the IA conditions through alternating transmissions. The iterative procedure is summarized in Algorithm 2.

Algorithm 2 The IA algorithm from [GCJ11]

```
Initialize the set of precoders randomly;
repeat
    Transmitters send pilot symbols using the precoders;
    Receivers estimate the forward channels and calculate the interference covariance matrix;
    Update the combiners as the eigen-vectors associated with the least eigen-values of the interference covariance matrix;
    Reverse the transmission direction;
    Receivers send pilot symbols using the combiners;
    Transmitters estimate the backward channels and calculate the interference covariance matrix;
    Update the precoders as the eigen-vectors associated with the least eigen-values of the interference covariance matrix;
    Reverse the transmission direction;
until The precoders and combiners converge.
```

In fact, selecting the precoders and combiners is not limited by the criterion introduced in Algorithm 2. Since then, other more advanced strategies have been suggested with respect to different objectives and application scenarios. For example, the authors of [GCJ11] also

proposed another version that maximizes the signal to interference plus noise ratio (SINR) at each iteration, which outperforms their original algorithm at low SNR. [WV13] further modified this algorithm to make it convergent by bringing power allocation into the picture. No matter how the criterion changes, such algorithms share a common framework as shown in Fig. 3.2, and heavily rely on the assumption of channel reciprocity. By alternating the transmission direction, the precoders and combiners are optimized following a certain rule until convergence. After the iterative training, concurrent data links can be established yielding greatly improved network sum rate.

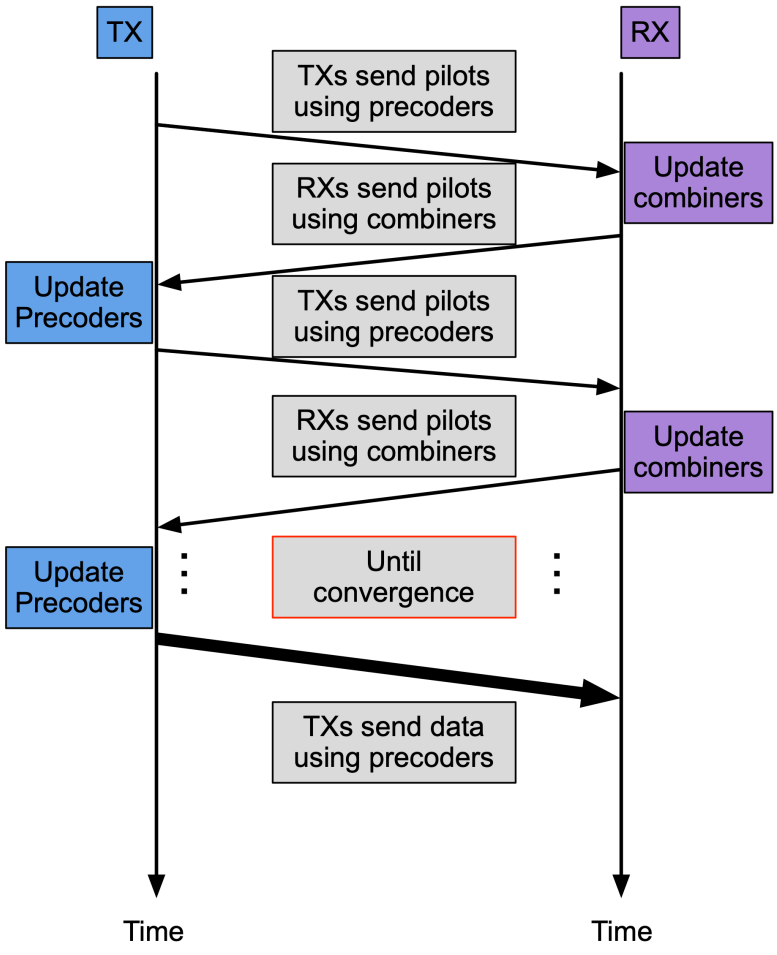

Figure 3.2: The pictorial representation of iterative interference alignment algorithms that exploit channel reciprocity.

3.3 Non-reciprocity of Baseband TDD MIMO Channel

In TDD systems, even though the physical channel involved in the over-the-air electromagnetic wave propagation can be considered reciprocal within a short period of time, i.e. less than the channel coherence time, this property generally does not hold when the hardware components are incorporated. In the context of IA or other high-level applications, it is obvious that the channels are between the digital basebands including the RF circuits and antennas. For a typical transceiver, the circuits to be used in transmit and receive modes are two individual signal paths, and therefore break the reciprocity.

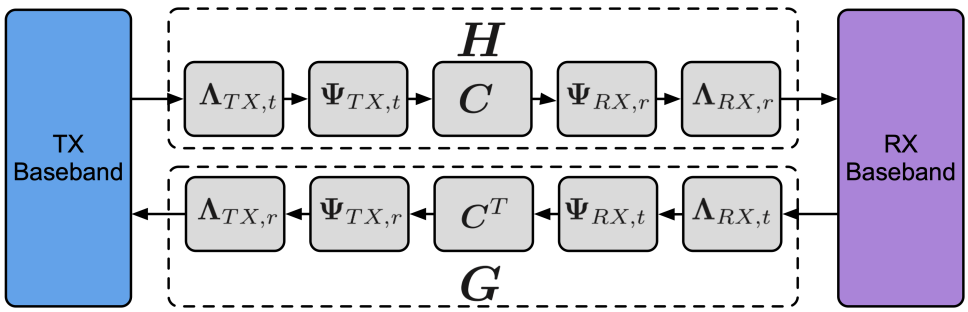

Figure 3.3: The block diagram of the baseband TDD MIMO channel.

In this section, we model the baseband MIMO channel between an arbitrary pair of transmitter and receiver as illustrated in Fig. 3.3. The forward channel is at the top, whereas the backward channel is at the bottom. The arrow shows the direction of the signal flow. As linear time invariant (LTI) systems, both the forward and backward channels consist of five serial blocks: transmit front-end $\boldsymbol{\Lambda}_t$, antenna array in transmit mode $\boldsymbol{\Psi}_t$, physical channel $\boldsymbol{C}$, antenna array in receive mode $\boldsymbol{\Psi}_r$, and receive front-end $\boldsymbol{\Lambda}_r$. Given a block fading channel, the system function of each block is a matrix with complex elements of different sizes. Due to the reciprocity of the physical channel, the matrix $\boldsymbol{C}$ of size $N_{RX} \times N_{TX}$ are identical in both directions except for the transpose operation. The matrices $\boldsymbol{\Psi}_t$ and $\boldsymbol{\Psi}_r$ are the responses of the antenna array in the transmit and receive modes respectively, which characterize the antenna array mutual coupling effect. Similarly, $\boldsymbol{\Lambda}_t$ and $\boldsymbol{\Lambda}_r$ stand for the different gains of the two individual sets of RF front-ends of a MIMO transceiver while operated in the two

different modes . The subscripts also tell whether the matrix is for the transmitter (TX) or the receiver (RX). If it is for the transmitter, it has the size of $N_{TX} \times N_{TX}$, otherwise $N_{RX} \times N_{RX}$. As a whole, the composite forward and backward channels, denoted as $\boldsymbol{H}$ and $\boldsymbol{G}$ respectively, thus can be calculated as the product of the responses of all blocks, which are

$$\begin{aligned} \boldsymbol{H} &= \boldsymbol{\Lambda}_{RX,r}\boldsymbol{\Psi}_{RX,r}\boldsymbol{C}\boldsymbol{\Psi}_{TX,t}\boldsymbol{\Lambda}_{TX,t}, \\ \boldsymbol{G} &= \boldsymbol{\Lambda}_{TX,r}\boldsymbol{\Psi}_{TX,r}\boldsymbol{C}^T\boldsymbol{\Psi}_{RX,t}\boldsymbol{\Lambda}_{RX,t}. \end{aligned} \tag{3.3}$$

The mutual coupling effect is defined as the electromagnetic interaction between closely placed elements of an antenna array, and plays a significant role in multi-antenna applications. Unfortunately, it has been either ignored or considered symmetric in numerous studies on TDD MIMO channel reciprocity [GSK05, BCK03, KJG10, SLY11, PSL13], where $\boldsymbol{\Psi}_t$ and $\boldsymbol{\Psi}_r$ are assumed to be diagonal matrices. Nevertheless, the mutual coupling broadly exists and behaves differently in the transmit and receive modes [Bal16, Hui04, LHL09]. Here, we derive the coupling matrix from the Thevenin equivalent circuit and show the non-symmetry in theory.

3.3.1 Coupling Matrix in Transmit Mode

Based on the antenna array theory [Bal16], the electromagnetic radiation behaviour happening in the transmit mode between arbitrary mth and nth elements of an antenna array with N total elements is presented in Fig. 3.4a, where the arrows with Roman numerals specify the energy travelling direction and sequence. The RF front-end for each port is attached to the antenna with energy travelling towards the antenna (i). Starting from the mth antenna, there is energy radiated into space (ii) and towards the nth antenna (iii). Because of the incident energy, the nth antenna sets up currents that result in energy rescattering to space (iv) and energy travelling towards the nth front-end circuit (v). Part of the rescattered energy is captured by the mth antenna (vi) and this process continues on and on. When all the ports are driven by the RF front-ends simultaneously, the ultimate radiated and rescattered fields are formed following the superposition rule.

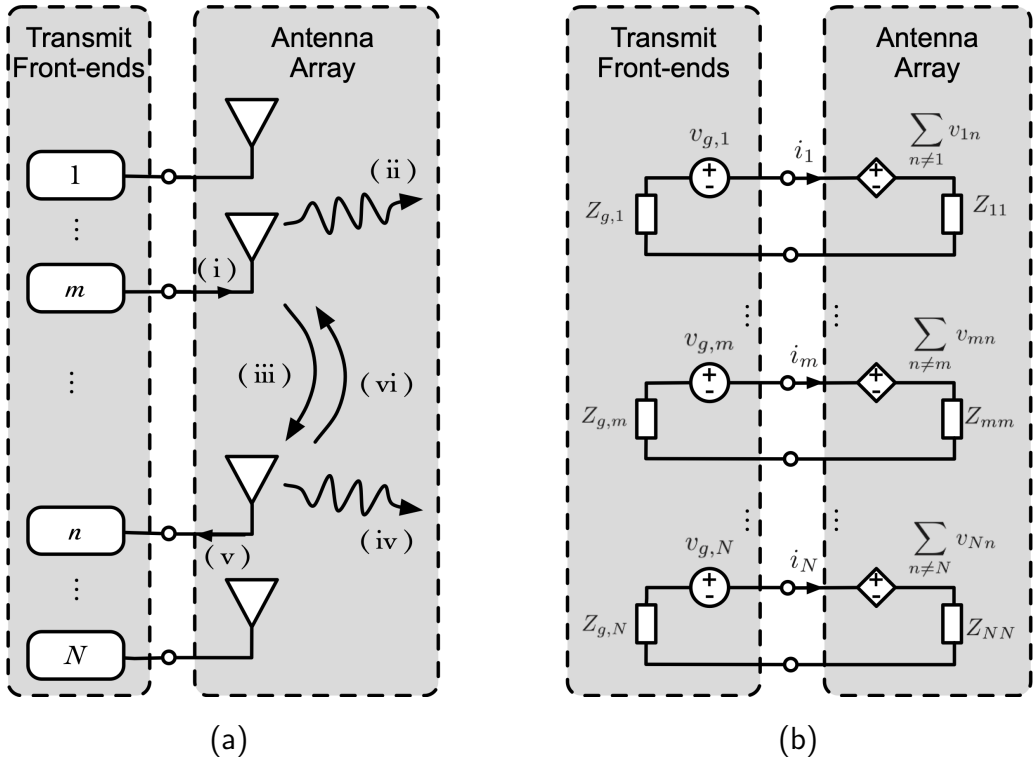

Figure 3.4: The mutual coupling effect in transmit mode.

Correspondingly we have the equivalent circuits for the RF front-ends and the antenna array as depicted in Fig. 3.4b. The symbols with shape of circle, diamond, and rectangle correspond to independent voltage source, dependent voltage source, and impedance respectively. In the transmit mode, the mth RF front-end is modeled as an independent voltage source $v_{g,m}$ with equivalent impedance $Z_{g,m}$. The current in the circuit is denoted by i_m. The antenna is characterized as the combination of the antenna's isolated self-impedance Z_{mm} and a dependent voltage source $\sum_{n\neq m} v_{mn}$. The voltage v_{mn} is the coupled voltage from the nth antenna subject to

$$v_{mn} = Z_{mn} i_n, \tag{3.4}$$

where Z_{mn} is the mutual impedance between the mth and nth antennas. The contribution of the mth antenna's radiation to the entire electromagnetic field is calculated as

$$v_{t,m} = Z_{mm} i_m. \tag{3.5}$$

According to Kirchhoff's voltage law, the following equations hold

$$\begin{aligned} v_{g,1} - Z_{g,1} i_1 \qquad & -Z_{11} i_1 + \sum_{n \neq 1} v_{1n} \quad = 0 \\ v_{g,2} - Z_{g,2} i_2 \qquad & -Z_{22} i_2 + \sum_{n \neq 2} v_{2n} \quad = 0 \\ \vdots \qquad & \qquad\qquad\qquad\qquad \vdots \\ v_{g,N} - Z_{g,N} i_N \quad & -Z_{NN} i_N + \sum_{n \neq N} v_{Nn} \quad = 0. \end{aligned} \tag{3.6}$$

By putting (3.4) and (3.5) into (3.6), the relationship between the transmitted signals and the driving signals and the coupling matrix are obtained in compact matrix form as

$$\boldsymbol{v}_t = \boldsymbol{\Psi}_t \boldsymbol{v}_g, \tag{3.7}$$

$$\boldsymbol{\Psi}_t = \boldsymbol{Z}_a (\boldsymbol{Z}_a + \boldsymbol{Z}_g + \boldsymbol{Z}_m)^{-1}, \tag{3.8}$$

where $\boldsymbol{v}_t = [v_{t,1}, v_{t,2}, \ldots, v_{t,N}]^T$ is the vector of radiated signal from each antenna, $\boldsymbol{v}_g = [v_{g,1}, v_{g,2}, \ldots, v_{g,N}]^T$ is the vector of the driving signal generated by the front-ends, and

$$\boldsymbol{Z}_a = \begin{bmatrix} Z_{11} & 0 & \ldots & 0 \\ 0 & Z_{22} & \ldots & 0 \\ \vdots & \vdots & \ddots & \vdots \\ 0 & 0 & \ldots & Z_{NN} \end{bmatrix}, \boldsymbol{Z}_g = \begin{bmatrix} Z_{g,1} & 0 & \ldots & 0 \\ 0 & Z_{g,2} & \ldots & 0 \\ \vdots & \vdots & \ddots & \vdots \\ 0 & 0 & \ldots & Z_{g,N} \end{bmatrix},$$

$$\boldsymbol{Z}_m = \begin{bmatrix} 0 & Z_{12} & \ldots & Z_{1N} \\ Z_{21} & 0 & \ldots & Z_{2N} \\ \vdots & \vdots & \ddots & \vdots \\ Z_{N1} & Z_{N2} & \ldots & 0 \end{bmatrix}$$

are respectively the matrices of the antenna self impedance, front-end equivalent impedance, and the antenna mutual impedance.

3.3.2 Coupling Matrix in Receive Mode

In the receive mode, the mutual coupling effect is shown in Fig. 3.5a, where the arrows with Roman numerals specify the energy travelling direction and sequence. The mth antenna

is first struck by the incident wave (i) from free space, yielding induced current flow (ii) towards the RF front-end. Due to the induced current flow, energy is radiated to space (iii), and part of it is captured by the nth element (iv). The subsequently induced current in the nth antenna similarly radiates energy to space as (vi) and continues affecting the mth antenna. The same procedure happens to all antennas when they are hit by the incident wave, and the the ultimate current distribution and total field can be added up linearly as for the transmit mode.

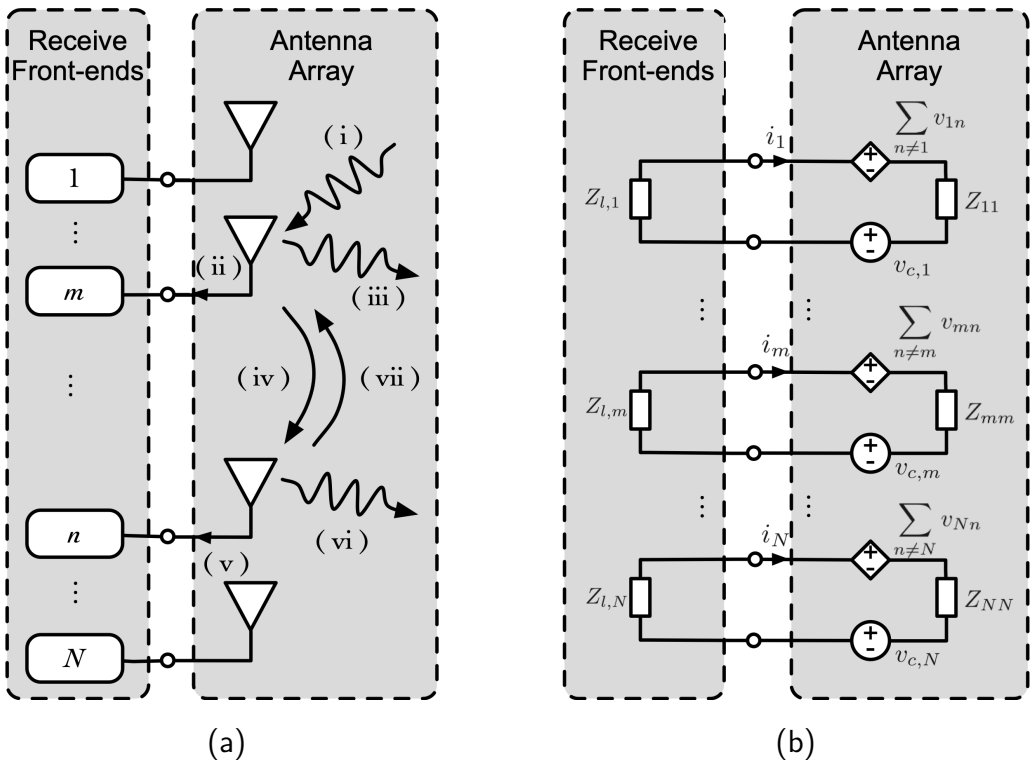

Figure 3.5: The mutual coupling effect in receive mode.

As for the equivalent circuit for receive mode given in Fig. 3.5b, it can be noted that the mth RF front-end now is modeled as a passive load impedance $Z_{l,m}$, whereas the mth antenna incorporates an additional voltage source $v_{c,m}$ corresponding to the incident wave

being captured. Similarly, Kirchoff's law gives us the following equations:

$$\begin{aligned}
v_{c,1} - Z_{l,1} i_1 \qquad & -Z_{11} i_1 + \sum_{n \neq 1} v_{1n} \quad &= 0 \\
v_{c,2} - Z_{l,2} i_2 \qquad & -Z_{22} i_2 + \sum_{n \neq 2} v_{2n} \quad &= 0 \\
\vdots \qquad & \qquad\qquad\qquad\qquad\qquad \vdots \\
v_{c,N} - Z_{l,N} i_N \quad & -Z_{NN} i_N + \sum_{n \neq N} v_{Nn} \quad &= 0.
\end{aligned} \tag{3.9}$$

In the receive mode, the signal observed by the mth front-end $v_{r,m}$ is the voltage over the load impedance, which is

$$v_{r,m} = Z_{l,m} i_m. \tag{3.10}$$

How it relates to the captured incident wave, i.e. the coupling matrix, can be found to be

$$\boldsymbol{v}_r = \boldsymbol{\Psi}_r \boldsymbol{v}_c, \tag{3.11}$$

$$\boldsymbol{\Psi}_r = \boldsymbol{Z}_l (\boldsymbol{Z}_a + \boldsymbol{Z}_l + \boldsymbol{Z}_m)^{-1}, \tag{3.12}$$

where $\boldsymbol{v}_r = [v_{r,1}, v_{r,2}, \ldots, v_{r,N}]^T$ is the vector of signals observed by each front-end, $\boldsymbol{v}_c = [v_{c,1}, v_{c,2}, \ldots, v_{c,N}]^T$ is the vector of signals captured by the antenna array, and the impedance matrices are defined the same as the transmit mode except

$$\boldsymbol{Z}_l = \begin{bmatrix} Z_{l,1} & 0 & \ldots & 0 \\ 0 & Z_{l,2} & \ldots & 0 \\ \vdots & \vdots & \ddots & \vdots \\ 0 & 0 & \ldots & Z_{l,N} \end{bmatrix}.$$

3.3.3 Non-reciprocity of Mutual Coupling

Given the derived expressions (3.8) and (3.12), the coupling matrices $\boldsymbol{\Psi}_t$ and $\boldsymbol{\Psi}_r$ are found to have a similar structure but very different components. This is because the excitation mechanisms and the connected circuits differ in the transmit and receive modes as described in the previous two subsections. The self and mutual impedance are intrinsic properties of an antenna array that primarily depend on the relative separation and orientation. Although

they stay the same when the mode switches, the current flow distribution may vary upon the associated circuit, thus leading to different coupling matrices.

In the ideal case, when $\boldsymbol{Z}_a$, $\boldsymbol{Z}_g$,and $\boldsymbol{Z}_l$ are assumed to be equal for perfect matching, we do have the equality between $\boldsymbol{\Psi}_t$ and $\boldsymbol{\Psi}_r$. Nevertheless, in practice, the manufacturing error is inevitable and the matching technique is never perfect. Most importantly, the transmit and receive RF front-ends are essentially two individual circuits. Therefore, the reciprocity of coupling matrices in general should not be taken for granted.

3.4 Reciprocity Calibration for IA Network

Interference alignment imposes high requirements on channel reciprocity, because, to enable the cooperation between the transmitters, both the desired and interfering channels are expected to be reciprocal. Given the channel model in the previous section, the network-wise channel reciprocity can be achieved with the plausible calibration matrices (3.13) that compensate the mismatch between the transmit and receive modes.

$$\begin{aligned} \boldsymbol{\Gamma}_{TX} &= \boldsymbol{\Lambda}_{TX,t}^{T}\boldsymbol{\Psi}_{TX,t}^{T}\boldsymbol{\Psi}_{TX,r}^{-1}\boldsymbol{\Lambda}_{TX,r}^{-1}, \\ \boldsymbol{\Gamma}_{RX} &= \boldsymbol{\Lambda}_{RX,t}^{T}\boldsymbol{\Psi}_{RX,t}^{T}\boldsymbol{\Psi}_{RX,r}^{-1}\boldsymbol{\Lambda}_{RX,r}^{-1}. \end{aligned} \tag{3.13}$$

By applying the calibration matrices (3.13) to the channel given by (3.3), we can calculate the calibrated channels $\tilde{\boldsymbol{H}}$ and $\tilde{\boldsymbol{G}}$ as

$$\begin{aligned} \tilde{\boldsymbol{H}} &= \boldsymbol{\Gamma}_{RX}\boldsymbol{H} = \boldsymbol{\Lambda}_{RX,t}^{T}\boldsymbol{\Psi}_{RX,t}^{T}\boldsymbol{C}\boldsymbol{\Psi}_{TX,t}\boldsymbol{\Lambda}_{TX,t}, \\ \tilde{\boldsymbol{G}} &= \boldsymbol{\Gamma}_{TX}\boldsymbol{G} = \boldsymbol{\Lambda}_{TX,t}^{T}\boldsymbol{\Psi}_{TX,t}^{T}\boldsymbol{C}^{T}\boldsymbol{\Psi}_{RX,t}\boldsymbol{\Lambda}_{RX,t}, \end{aligned} \tag{3.14}$$

such that the reciprocity condition (3.15) is satisfied.

$$\tilde{\boldsymbol{H}} = \left(\tilde{\boldsymbol{G}}\right)^{T} \tag{3.15}$$

Although such a calibration matrix exists, unfortunately, the information required to directly compose the calibration matrix is usually not available. A more practical method is to directly find such a calibration matrix for each node that approximates (3.13) and enables channel reciprocity. In this section, we propose a calibration method that, with the help of a single-antenna reference node, finds the calibration matrices for all nodes in the IA network.

3.4.1 Calibration with Single-antenna Reference Node

Consider the bidirectional channels between an arbitrary multiple-antenna node and the single-antenna reference node, and the multiple-input single-output (MISO) channels are reduced from (3.3) as

$$\begin{aligned} \boldsymbol{h} &= \lambda_{ref,r} \boldsymbol{c} \boldsymbol{\Psi}_t \boldsymbol{\Lambda}_t, \\ \boldsymbol{g} &= \boldsymbol{\Lambda}_r \boldsymbol{\Psi}_r \boldsymbol{c}^T \lambda_{ref,t}, \end{aligned} \tag{3.16}$$

where $\lambda_{ref,t}$ and $\lambda_{ref,t}$ are the respective gains of the reference node in transmit and receive mode, and no coupling matrix is needed for the reference node since there is only a single antenna. Because $\lambda_{ref,t}$ and $\lambda_{ref,t}$ are commutative scalars, given any channel $\boldsymbol{c}$, the relationship between h and g follows

$$\boldsymbol{h}^T = \boldsymbol{\Gamma} \boldsymbol{g}, \tag{3.17}$$

$$\boldsymbol{\Gamma} = \frac{\lambda_{ref,r}}{\lambda_{ref,t}} \boldsymbol{\Lambda}_t^T \boldsymbol{\Psi}_t^T \boldsymbol{\Psi}_r^{-1} \boldsymbol{\Lambda}_r^{-1}. \tag{3.18}$$

The matrix Γ only differs from the ideal calibration matrices given by (3.13) in the constant factor of $\lambda_{ref,r}/\lambda_{ref,t}$. For an arbitrary transmitter and receiver pair, if we apply (3.18) as the calibration matrix, the reciprocity condition (3.15) will also be satisfied even with that factor. The most important thing is that, unlike (3.13), $\boldsymbol{\Gamma}$ can be estimated using either the total least squares (TLS) method proposed in [GSK05] or the least squares (LS) method from [RBP14] depending on the trade-off between performance and efficiency. Consequently, we deconstruct the reciprocity calibration problem for the IA network as individual calibration problems between each node and the reference node.

3.4.2 Calibration Matrix Estimation

In order to find the calibration matrix, we need multiple pairs of bidirectional MISO channels to begin with. The node and the reference can take turns to transmit known pilot symbols within a short period of time for invariant physical channels. Then, using the received pilots, the channels are estimated, and the estimation errors are assumed to be Gaussian distributed complex random variables. On top of that, because the calibration matrix $\boldsymbol{\Gamma}$ has a size of

$N \times N$, N^2 independent equations are needed to find the N^2 elements. Thus, at least N different physical channel realizations are required to make the system over-determined, each providing N equations.

Given K pairs of such bidirectional channel estimates from at least N physical channel realizations, we formulate the calibration matrix estimation problem as

$$\begin{aligned}\hat{\boldsymbol{\Gamma}} &= \underset{\boldsymbol{\Gamma},\theta_1,\ldots,\theta_K}{\arg\min} \sum_{k=1}^{K} \left\| \hat{\boldsymbol{h}}_k - \boldsymbol{\Gamma}\hat{\boldsymbol{g}}_k e^{i\theta_k} \right\|^2 \\ &= \underset{\boldsymbol{\Gamma},\boldsymbol{\Theta}}{\arg\min} \left\| \hat{\boldsymbol{H}} - \boldsymbol{\Gamma}\hat{\boldsymbol{G}}\boldsymbol{\Theta} \right\|_F^2,\end{aligned} \tag{3.19}$$

where $\hat{\boldsymbol{H}} = \left[\hat{\boldsymbol{h}}_1^T, \hat{\boldsymbol{h}}_2^T, \ldots, \hat{\boldsymbol{h}}_K^T\right]$ and $\hat{\boldsymbol{G}} = [\hat{\boldsymbol{g}}_1, \hat{\boldsymbol{g}}_2, \ldots, \hat{\boldsymbol{g}}_K]$ are the collected K pairs of bidirectional channel estimates in matrix form, and $\boldsymbol{\Theta}$ is a diagonal matrix defined as

$$\boldsymbol{\Theta} = \begin{bmatrix} e^{i\theta_1} & 0 & \ldots & 0 \\ 0 & e^{i\theta_2} & \ldots & 0 \\ \vdots & \vdots & \ddots & \vdots \\ 0 & 0 & \ldots & e^{i\theta_K} \end{bmatrix}$$

correcting the relative phase uncertainty in the K channel measurements. The relative phase offsets between $\hat{\boldsymbol{h}}$ and $\hat{\boldsymbol{g}}$ should be identical to make the estimation of $\boldsymbol{\Gamma}$ meaningful. Nevertheless, in practice, the radios are not perfectly synchronized in frequency, and random phase offset is induced when the radios are not controlled strictly in time, i.e. the time interval consumed to switch the channel direction varies every time. Although the objective function is minimized when $\boldsymbol{\Gamma}$ approximates (3.18) and the phases are properly aligned using $\boldsymbol{\Theta}$, there is no trivial closed-form solution.

Fortunately, this optimization problem can still be solved iteratively. In each iteration, by fixing the $\boldsymbol{\Gamma}$ to be the estimate of $\hat{\boldsymbol{\Gamma}}$ from the last iteration, the objective function can be minimized by updating each element of $\hat{\boldsymbol{\Theta}}$ to be

$$\hat{\theta}_k = \angle\left(\boldsymbol{h}_k \boldsymbol{g}_k^H \hat{\boldsymbol{\Gamma}}^H\right), \tag{3.20}$$

where $\angle$ denotes the operation of extracting the phase of a complex number. This amounts to individually rotating each pair of channel coefficients until the distances are minimized.

Then, with the updated $\hat{\boldsymbol{\Theta}}$ being fixed, $\boldsymbol{\Gamma}$ further minimizing the objective function can be found to be the classic LS solution as

$$\hat{\boldsymbol{\Gamma}} = \hat{\boldsymbol{H}}\hat{\boldsymbol{\Theta}}^H\hat{\boldsymbol{G}}^H\left(\hat{\boldsymbol{G}}\hat{\boldsymbol{\Theta}}\hat{\boldsymbol{\Theta}}^H\hat{\boldsymbol{G}}^H\right)^{-1}. \tag{3.21}$$

By alternatively minimizing the non-negative objective function using (3.20) and (3.21) as summarized in Algorithm 3, the calibration matrix is estimated with assured convergence.

Algorithm 3 Iterative Calibration Matrix Estimation

```
Initialize the calibration matrix as an identity matrix I;
repeat
    Individually find each θ̂_k using (3.20);
    Update Θ̂;
    Find Γ̂ based off (3.21) using all channel estimates;
    Update Γ̂;
until The objective function in (3.19) converges;
Use Γ̂ as the ultimate calibration matrix that approximates (3.18).
```

3.5 Experimental Validation of the Proposed Calibration Method

Our method stands out from the other calibration methods by considering the off-diagonal elements of the calibration matrix introduced by the antenna array mutual coupling effect. We now inquire whether the effect is large enough that a diagonal calibration matrix is insufficient. In this section, we conduct experiments using real radios to show the mutual coupling effect in practice and validate our proposed channel reciprocity calibration method.

3.5.1 Hardware Setup

We placed 8 radios in total in our laboratory environment with a dimension of 11.2 m $\times$ 7.92 m as shown in Fig. 3.6. The radios are placed on tables and shelves, and they are represented by small colored shapes. The 3 blue square blocks on the left side are the

transmitters, while the 3 purple ones are the receivers on the other side. In addition, we have a beacon node in the cyan circle on the conference table and a single antenna reference node in the orange diamond. Among those radios, 6 of them are equipped with 2 antennas, and they are designated to be the 3 transmitters and 3 receivers in the 3-user IA network as in Fig. 3.1. One radio is the reference node with only one active antenna being enabled, which is required by the channel reciprocity calibration. Additionally, the reference node is mounted on top of a motorized rotary stage to provide multiple channel realizations, which may also be obtained by manually placing the reference node at different locations. In more practical situations, the motion of the radios, e.g. users moving with the nodes, could be utilized as well. The last radio is a beacon node that coordinates the signal transmission of the rest of the radios by broadcasting a beacon packet.

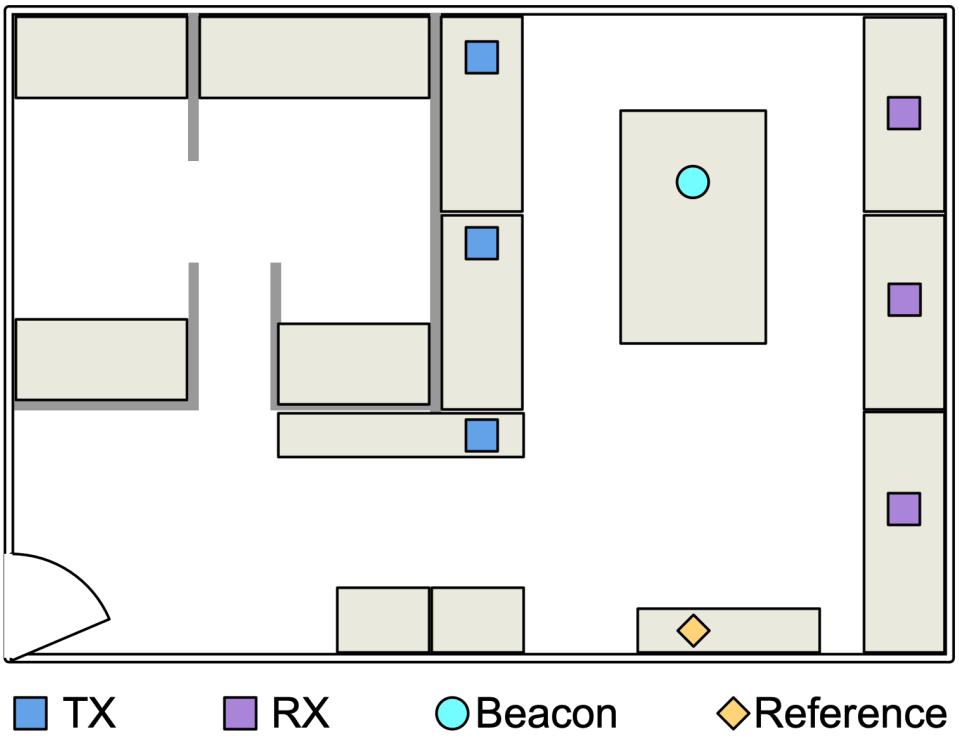

Figure 3.6: The floor plan of the experiment environment.

Each radio is a customized MIMO transceiver (SC3500) from SILVUS Technology, which is configured to operate in the frequency band from 2.4 GHz to 2.5 GHz with a bandwidth of 1.25 MHz and a total power of 0 dBm. The antenna (AOV3T245515575) used in our

experiment is a rubber ducky omni-directional mono-pole antenna with 3 dBi gain. The separation between the antennas is 2.54 cm, which is relatively compact for being less than a quarter of the wavelength. The radio root file system, Linux kernel, is installed to enable flexible control in a typical software defined radio (SDR) manner. To transmit an arbitrary signal, the samples can be stored in a file and loaded into a transmit buffer with a size of 32768. Every time when the transmission is triggered by the beacon, the buffer samples are flushed to the RF front-end for transmission. Similarly, in the receive mode, all captured samples are put into the receive buffer with the same size as the transmit buffer, then stored in a file for off-line post-processing. A laptop is connected to all radios via Ethernet cables, and processes the data transferred from each radio individually. There is no information exchange between the radios through the Ethernet connections, hence the radios actually run independently and the whole network still operates in a distributed manner as in practice.

3.5.2 Acquiring Bi-directional Channel Estimates

Our experiment is composed of a calibration phase and a verification phase as presented in Fig 3.7, where the blocks represent the signal packets that radios take turns to send. And the color shows the different origins of the signal packets. The beacon node only broadcasts the beacon packet and controls the signal transmission direction. The other nodes are loaded with the channel estimation packets and will send the packets upon the beacon detection. In the calibration phase, multiple bi-directional channel estimates under multiple physical channel realizations are needed for calculating the reciprocity calibration matrices. One pair of bi-directional channel estimates between the reference node and the other IA nodes was acquired following the procedure shown in Fig. 3.7a. The procedure is composed of the forward and backward channel measurement, each triggered by a beacon packet from the beacon node. In the forward channel measurement, all IA nodes take turns to send their channel estimation packets in the air, while the reference node receives. Then, the reference node broadcasts its packet and the others all capture it in the backward channel measurement. This procedure was repeated for multiple times at each reference node location

yielded by the rotary stage. In the verification phase, only a single pair of bidirectional MIMO channels between the transmitters and receivers are measured following the procedure in Fig. 3.7b. They are used to examine the calculated calibration matrices and see if the channel reciprocity can be achieved.

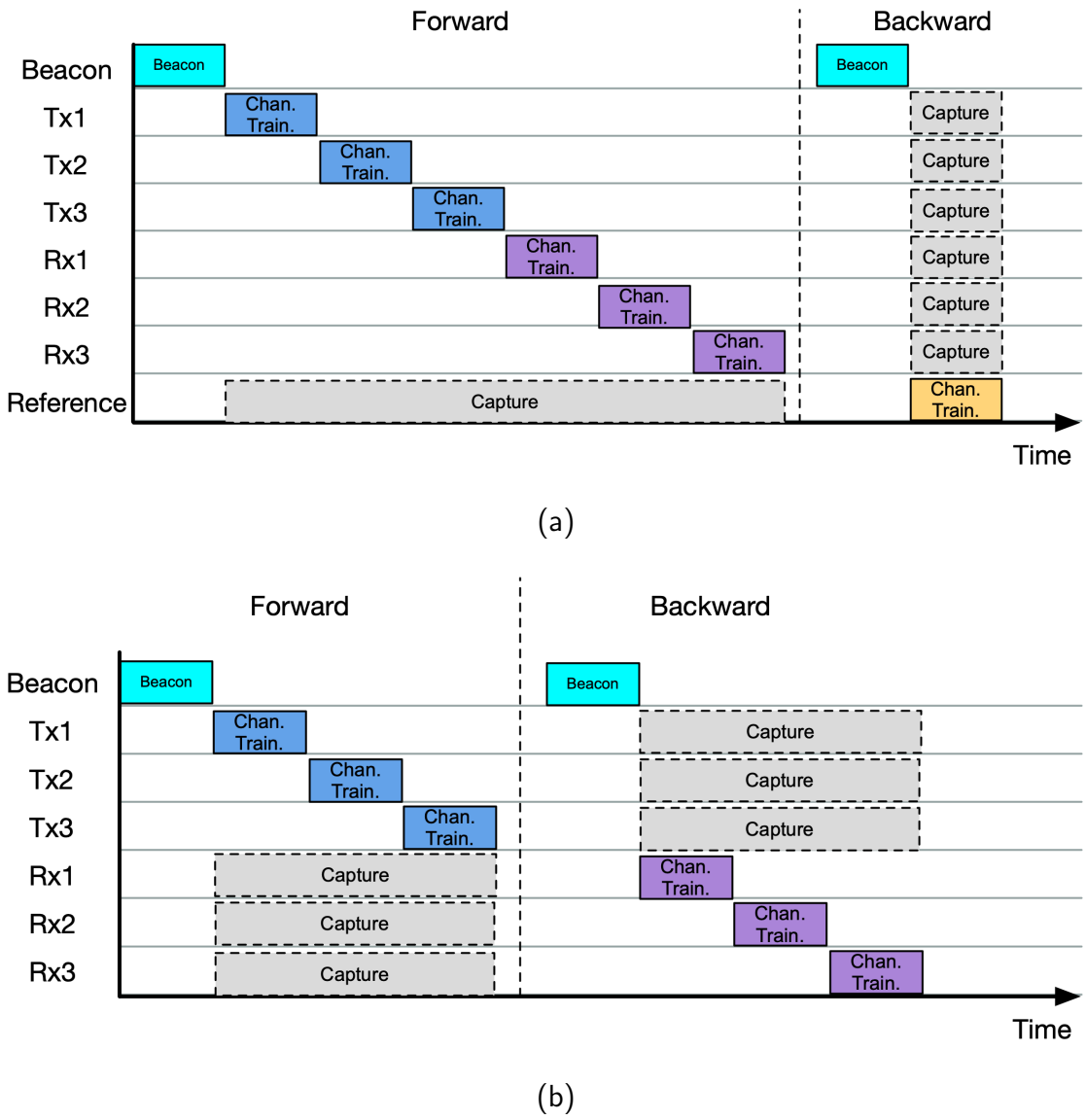

Figure 3.7: The calibration phase and the verification phase of the reciprocity calibration experiment procedure.

The beacon packet has an OFDM symbol whose sub-carriers are mapped from a specific identity sequence and a direction bit. The identity sequence is used to distinguish our

packets from the other roaming packets in the air as the experiment was conducted in an unregulated spectrum. The direction bit is used to notify the other radios whether it is the forward or backward channel being measured. Only when this packet is successfully decoded by the other radios in the network, the signal transmission and reception occur. Then all radios are coordinated in time via this beacon mechanism. It should be noted that the beacon mechanism is not mandatory for the calibration if other coordinating mechanisms are available such as using time stamps.

The channel training packet starts with a synchronization field required for accurate channel measurement. It has a repeated structure in time from which the frequency and timing synchronization can be achieved using the method in [SC97]. Following the synchronization field are the symbols intended for channel estimation. The symbol is generated by taking a 64-point inverse fast Fourier transform (IFFT) of a known sequence and adding a cyclic prefix (CP) of 16 samples. The same symbol is sent from each antenna in a time orthogonal manner. After correcting the frequency offset and taking a fast Fourier transform (FFT) of the captured samples, we adopted the classic LS estimators to obtain the channel estimates. For the calibration purpose, only the channel estimates of one specific valid sub-carrier are utilized for later processing. In general, any type of channel channel training packet can be used as long as it provides reasonably accurate bi-directional channel estimates within the coherence time.

3.5.3 Validating the Calibration Matrices

We applied our proposed calibration method to the acquired channel estimates for calculating the calibration matrices. Also, for comparison, we consider the case of ignoring the mutual coupling effect. In that case, the calculation of a diagonal $\mathbf{\Gamma}$ is decomposed into calculating each diagonal element individually as solving single-input single-output (SISO) problems, and our proposed method is still applicable. Taking the calculated calibration matrices for

node RX2 as an example, we have

$$\mathbf{\Gamma}_{full} = \begin{bmatrix} 0.76\underline{/-0.08^\circ} & 0.12\underline{/97.78^\circ} \\ 0.13\underline{/-29.50^\circ} & 1.49\underline{/-115.83^\circ} \end{bmatrix},$$

$$\mathbf{\Gamma}_{diag} = \begin{bmatrix} 0.67\underline{/-0.52^\circ} & 0 \\ 0 & 1.57\underline{/-115.97^\circ} \end{bmatrix},$$

where $\mathbf{\Gamma}_{full}$ and $\mathbf{\Gamma}_{diag}$ respectively denote the calculated calibration matrices in cases of considering and ignoring the mutual coupling effect, and the complex elements are shown in polar form for easy comparison. It can be noted that the off-diagonal elements in $\mathbf{\Gamma}_{full}$ are of great importance. Ignoring the mutual coupling effect, we ended up with $\mathbf{\Gamma}_{diag}$, which corrects the non-reciprocity to some extent, but not as well as $\mathbf{\Gamma}_{full}$.

Using the measured bidirectional MIMO channels between the transmitters and receivers, we checked if those calibration matrices can make them reciprocal as (3.14). Fig. 3.8 shows the example constellations of forward and backward MIMO channel coefficients. Three cases are considered: (a) Without calibration; (b) With calibration ignoring mutual coupling effect; (c) With calibration using the proposed method considering the mutual coupling effect. The four pairs of complex channel coefficients are from the 2×2 channel between the nodes TX2 and RX2 measured in the verification phase as an example. The forward channel coefficients are presented using blue circles, while the backward ones are shown as red crosses. Quantitatively, we evaluated the non-reciprocity as the sum of squared Euclidean distances between the forward and backward channel coefficients. Without calibration, the bidirectional channels are off by a significant amount as large as 18622.6. Even though the diagonal calibration matrix reduces the mismatch between the two channels to 854.7, obvious offset can still be seen. By contrast, only when the calibration matrix with off-diagonal elements is used, the residual mismatch can be minimized to 26.7. In summary, our proposed calibration method has been validated with experimental proof. Ignoring the mutual coupling effect will result in considerable residual mismatch between the forward and backward MIMO channels.

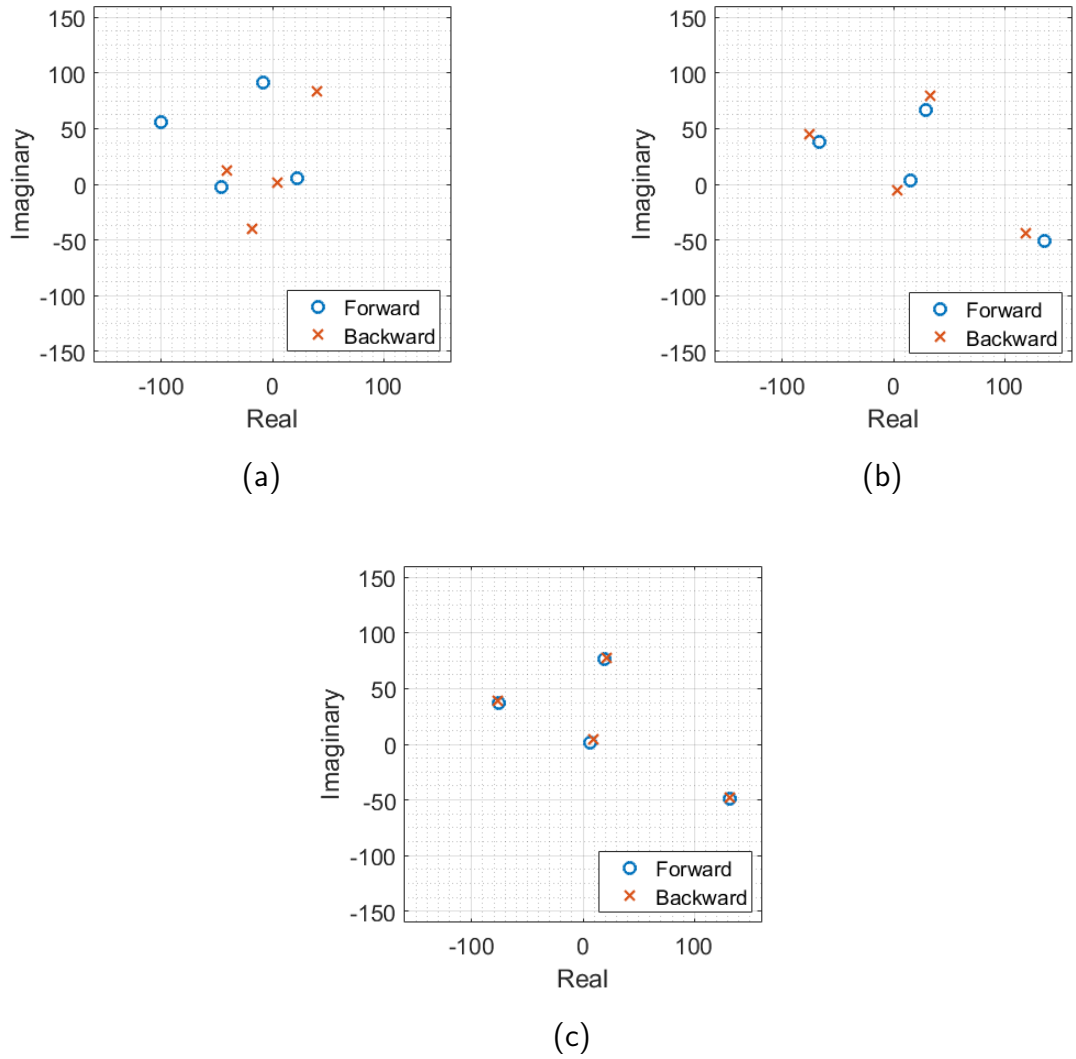

Figure 3.8: Constellations of calibrated forward and backward channel coefficients.

3.6 Impact on Interference Alignment Performance

Given the measured channels, it is clear that the channel reciprocity cannot be taken for granted in practice as introduced in earlier sections. Even with careful calibration, the forward and backward MIMO channels are not identical due to other hardware impairments such as the additive noise, the non-linearity of amplifiers, and the IQ imbalance etc.. For IA algorithms that assume perfect channel reciprocity, it is thus doubtful, under imperfect channel reciprocity, if the extraordinary performances promised by those algorithms can still be retained. Here, we consider two performance metrics: total interference leakage and the sum rate, which are used broadly in IA literature.

The total interference leakage is defined as the summation of the interference power observed by the receivers of each link in the IA network, which is calculated as

$$L = \sum_{i}^{K} \boldsymbol{w}_i^H \boldsymbol{Q}_i \boldsymbol{w}_i, \tag{3.22}$$

$$\boldsymbol{Q}_i = \sum_{j \neq i}^{K} \boldsymbol{H}_{ij} \boldsymbol{p}_j \boldsymbol{p}_j^H \boldsymbol{H}_{ij}^H \tag{3.23}$$

where $\boldsymbol{w}_i$ is the combining vector used by the receiver i, $\boldsymbol{Q_i}$ is the covariance matrix of the interference seen by the ith receiver, and $\boldsymbol{H}_{ij}$ is the calibration forward MIMO channel between the jth transmitter and the ith receiver. The notations for the precoding and combining matrices $\boldsymbol{P}_i$ and $\boldsymbol{W}_i$ in section II are respectively reduced to $\boldsymbol{p}_i$ and $\boldsymbol{w}_i$ in lower cases because we have had only a single data stream for each link in our experiment. Ideally, the total interference leakage can be monotonically decreased to 0 by running the iterative interference alignment algorithm proposed in [GCJ11].

The other performance metric we consider, the sum rate, is of more interest as it reveals the potential data throughput the IA network can support. The calculation of the sum rate follows

$$R = \sum_{i}^{K} \log_2 \left(1 + \frac{\boldsymbol{w}_i^H \boldsymbol{H}_{ii} \boldsymbol{p}_i \boldsymbol{p}_i^H \boldsymbol{H}_{ii}^H \boldsymbol{w}_i}{\sigma_i^2 + \boldsymbol{w}_i^H \boldsymbol{Q}_i \boldsymbol{w}_i} \right), \tag{3.24}$$

where σ_i^2 is the measured Gaussian noise variance, and the fractional term can be regarded as the SINR of each link. The sum rate achieved over the entire IA network is the summation of

the normalized link capacity achieved by all users. Relative to the total interference leakage, the sum rate is a more practical performance metric, because it puts the signal power into consideration and the signal power may end up being very small to meet the IA condition (3.2).

Given the measured channels and the calculated reciprocity calibration matrices, we simulated the evolution procedure of our 3-user 2×2 IA system running the Algorithm 2, and the results with respect to both the total interference leakage and the sum rate are shown in Fig. 3.9. The horizontal axis is the number of iterations the IA algorithm has been through, and the vertical axis is the performance metric of interest. Both figures have 4 curves with markers every 10 iterations. As the iterations went on, the total interference leakage L and sum rate R are recorded as functions of the number of iterations. The performances are compared considering the following 4 cases:

1. No calibration matrix is applied, and the raw forward and backward channels are used for IA.

2. The nodes are calibrated using the calibration matrix $\mathbf{\Gamma}_{diag}$, which ignores the mutual coupling effect and has only diagonal elements.

3. The nodes are calibrated using the calibration matrix $\mathbf{\Gamma}_{full}$, which considers the mutual coupling effect and incorporates off-diagonal elements.

4. The nodes are calibrated using the calibration matrix $\mathbf{\Gamma}_{full}$, but the backward channels are artificially made reciprocal of the forward channel as perfect reciprocity holds.

In Fig. 3.9a, we can see how the total interference leakage gradually gets diminished as the number of iterations increases. In the considered four cases, all the curves converge but end up with a very different ultimate leakage level. It is not surprising that, given the perfect channel reciprocity, the interference leakage is completely eliminated as desired satisfying the IA condition (3.2). By contrast, without any calibration, the iterative algorithm fails to further suppress the interference leakage after a few iterations. The ultimate

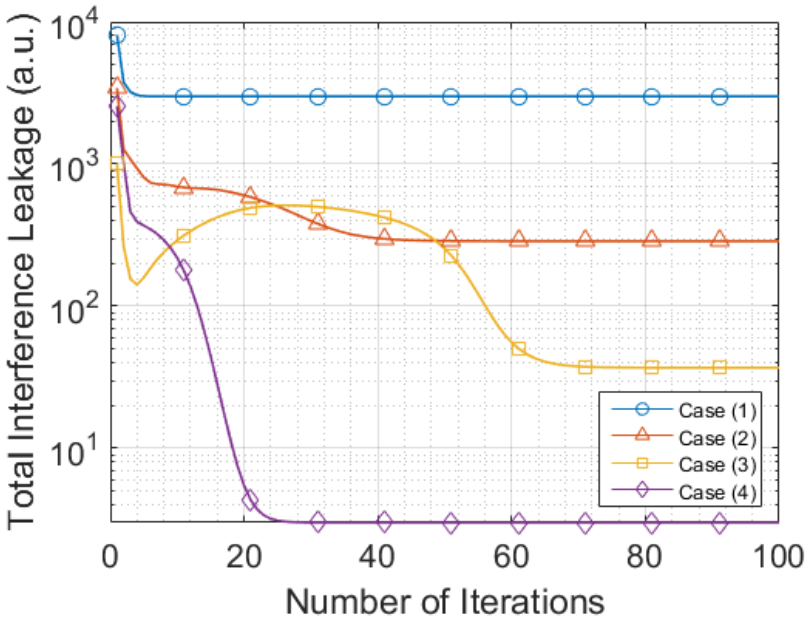

(a)

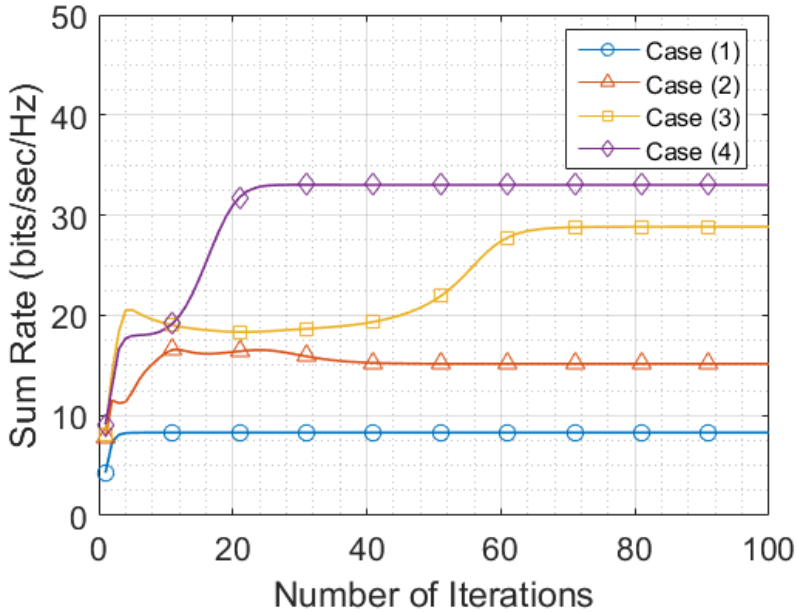

(b)

Figure 3.9: The evolution of our iterative IA system in different cases of calibration.

interference strength is still tremendous yielding no possibility of operating 3 high quality links concurrently. Comparing the residual total interference leakage of case (2) and (3), we see $\mathbf{\Gamma}_{full}$ outperforms $\mathbf{\Gamma}_{diag}$, which also validates the necessity of considering the antenna array mutual coupling effect in the reciprocity calibration for IA. Regarding Fig. 3.9a, the most thought-provoking observation is, due to channel non-reciprocity, the decreasing of the total interference leakage may not be monotonic. As in case (3), it takes many more iterations to converge to its optimum. In [GCJ11], assuming perfect channel reciprocity, it has been shown that the iterative IA algorithm has the property of monotonic convergence, which leads to fast convergence and high reliability. Nevertheless, this property no longer holds given the imperfect channel reciprocity in practice. Under circumstances when a large IA system training overhead should be avoided, i.e. the maximum number of iterations is limited, the optimal performance may not be achievable.

The Fig. 3.9b gives the comparison of the 4 cases from the perspective of sum rate. We pay attention to the final sum rates after the convergence, and the difference between case (2) and (3) is more obvious. Ignoring the mutual coupling effect results in significant performance drop. Even with the calibration matrices using our proposed method, the sum rate in case (3) is still short of the upper bound in case (4) due to the remaining mismatch between the forward and backward channels. This brings out the point that such imperfect channel non-reciprocity should be taken into account when devising an IA algorithm that attempts to exploit the reciprocal channel. Other than that, assessing the performance of a channel reciprocity based IA algorithm should take the channel non-reciprocity mismatch into consideration as well as other hardware impairments.

3.7 Summary

IA is a precoding technique that promises to boost the throughput of wireless networks. This chapter focuses on a category of IA algorithms that rely on the reciprocity of TDD MIMO channels. However, the channels are not reciprocal in practice when the RF front-end circuits come into the picture. This issue has been studied in this paper by modeling the channels

with the transceiver working in both transmit and receive modes. The antenna array mutual coupling effect has been emphasized for often being ignored by other researchers. In fact, the mutual coupling effect generally exists and complicates the calibration required to regain the channel reciprocity. To deal with this problem, we have proposed a calibration method that incorporates a single-antenna reference node. This method has been validated with solid experimental results and compared with the case ignoring the mutual coupling effect. In the end, we have also investigated how the channel non-reciprocity affects the performance of an IA system as a rather significant hardware impairment. Proper channel reciprocity calibration is indispensable to achieve the promising throughput improvement using IA in practice.

CHAPTER 4

Extending Spatial and Temporal Characterization of Indoor Wireless Channels from 350 GHz to 650 GHz

4.1 Overview

The demands for robust high-speed wireless services have been growing in the past decades because of the dramatic changes in the ways people create and share information. However, the speed of today's wireless communication systems is mainly limited by the narrow bandwidth of existing transceivers and the heavy use of the wireless spectrum up to 60 GHz [Rap96]. The increasing demand has motivated researchers to explore the possibility of operating at higher frequency bands that have not been allocated to any specific active service yet [DSP15, KLA13, NHM13, SFB14, SN11].

The terahertz frequencies, which cover the frequency range of 0.3-10 THz, have attracted interest due to the recent advancements in terahertz electronics [TGK08, GVP08] and photonics [Jar15, YJ18, PDM11]. Developing communication systems at such high carrier frequencies has become promising, and it is very likely to support links with data rates exceeding 50 Gbit/s for distances over 20 meters [SKA14, NOY16]. A system with this capability is suitable for next generation indoor wireless applications, such as ultra-fast kiosk downloads, uncompressed video streaming, and wireless extension of wired backbone networks.

Developing a robust wireless communication system that maintains a high signal-to-noise ratio (SNR) and a high data rate requires prior knowledge of channel statistics for different frequencies. An appropriate channel model is crucial to effectively evaluate different communication methodologies and determine appropriate protocols, such as equalization, modula-

tion and adaptation schemes. At lower frequencies up to 6 GHz, a large number of studies have been exhaustively conducted to understand radio propagation for both existing cellular and indoor wireless applications [Par92, Has93, JW04]. For the same reason, many studies have also been conducted on the channels at higher frequencies between 28 and 78 GHz that are to be deployed for future 5G millimeter-wave technology [XKR02, MMI96, MC04]. These studies have measured the path loss due to propagation, the power attenuation caused by absorption, and multipath effects due to reflection. Through these studies, parameters such as the Doppler frequency and delay spread have been characterized, statistical models have been created, and ray-tracing methods have been developed. In comparison, as a prerequisite for developing terahertz communication systems, however, the studies of terahertz channels have been limited to the atmospheric transmission bands below the 350 GHz transmission window [JPM11, PKJ13, PK13, PJJ11, HGF17, PJM07, KJP12], while mostly considering short-range communication paths, which are not applicable to realistic indoor communication systems. Atmospheric transmission windows are defined as the frequency bands with relatively low atmospheric attenuation [SWP12].

These are significant limitations, preventing an in-depth understanding of the characteristics of terahertz communication channels at higher-frequency atmospheric transmission bands at which high-power transmitters and high-sensitivity receivers have become available [HYY17, YWL15, YJ15, BHP14, WCL18], making it possible to build higher data-rate communication systems in the future. Existing channel models at frequencies bellow 350 GHz are not directly applicable to higher frequency bands when considering the directional nature of the terahertz beams used in communication systems and the diffusive reflections from objects with roughness levels comparable to or larger than the wavelength.

At terahertz frequencies, on both the transmitter (Tx) and receiver (Rx) sides, it is necessary to have either directional antennas or large-scale antenna arrays with the capability of transmitting/receiving narrow beams. The two main reasons for this requirement are as follows. First, the radiated signal power is low due to power limitations of existing terahertz radiation sources and high atmospheric losses. It is only realistic to ensure reasonable

signal strength at the receiver side by incorporating high antenna gains in the link budget. Second, in the absence of a directional beam and without the spatial filtering of multipath components, the delay spread exceeds 30 ns or over 300 symbols at a 10 GHz symbol rate in an indoor scenario, which requires a very complex equalizer to address the inter-symbol interference (ISI). However, the multipath components are significantly filtered out spatially when using a directional beam, eliminating the need for a complicated equalizer.

One concern about using highly directional beams is sustaining a communication link when the line-of-sight (LoS) path is obstructed by moving objects or people. Having a non-line-of-sight (NLoS) path with a sufficient signal level prevents catastrophic signal loss. In this regard, it is necessary to have an extensive multipath channel model that describes the spatial distribution of all available paths and their relative power levels. The other concern is the residual channel dispersion of the spatially resolved paths. The diffusive reflections from a rough surface may result in multipath components that will arrive from the same direction and will require equalization depending on the desired symbol rate and the channel dispersion. The impact of the diffusive reflections can be significantly affected by the wavelength of the terahertz beam, which is often comparable with or smaller than roughness of the objects in an indoor communication system. Therefore, this chapter is dedicated to expanding the spatial and temporal characterization of terahertz wireless channels in a typical indoor environment from the 350 GHz to 650 GHz transmission window. The 350 GHz and 650 GHz transmission windows are chosen for comparison to gain more insight into terahertz wave propagation at different wavelength ranges.

4.2 Measurement System

4.2.1 Power Angle Profile Measurement System

Power angle profile (PAP) measurements characterize the relative signal strength as a function of both the angle of departure (AoD) and the angle of arrival (AoA). Each combination of an AoD and an AoA corresponds to a path in the space, and PAP records the spatial

power distribution. Figure 4.1 shows the block diagram of our PAP measurement system. We transmit a continuous wave (CW) 350/650 GHz signal along different paths and examine if the SNR of the received signal is sufficient to decode the transmitted data.

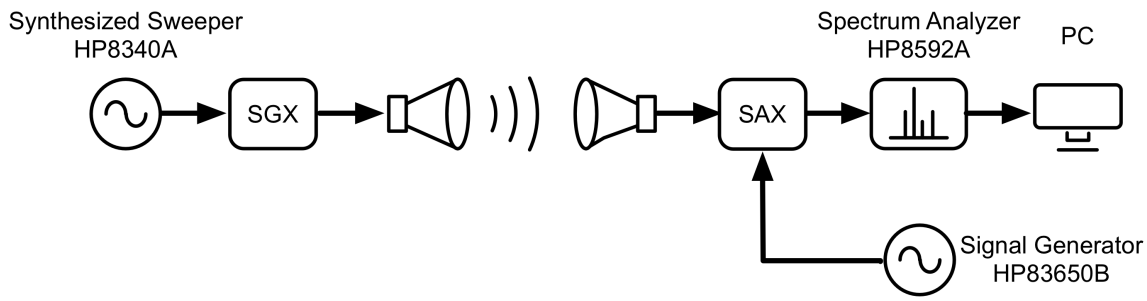

Figure 4.1: Block diagram of the PAP measurement system.

On the Tx side, a synthesized sweep signal generator (HP8340A) generates a radio frequency (RF) CW signal, which feeds a signal generator extension (SGX) module from Virginia Diodes, Inc. (VDI). The SGX module is an amplifier/multiplier chain (AMC) with reconfigurable waveguide-fed components that can boost the frequency of the input signal to cover different terahertz frequency ranges. It has a typical output power of 0 and -10 dBm when configured for the WR 2.8 and WR 2.2 waveguide bands respectively. Horn antennas with a 25 dBi gain and a 12-degree half power beamwidth (HPBW) are used on both the Tx and Rx sides. On the Rx side, the received signal is fed into a spectrum analyzer extension (SAX) module also from VDI. The SAX module employs a mixer/amplifier/multiplier chain (MixAMC), which has an additional sub-harmonic mixer compared with the SGX module. This mixer down-converts the received terahertz signal to a desired intermediate frequency by mixing with a CW signal, whose frequency is extended by the incorporated amplifier/multiplier chain. The saturation power levels of the SAX module are -10 dBm and -20 dBm when configured for the WR 2.8 and WR 2.2 waveguide bands respectively. Another synthesized sweep signal generator (HP83650B) on the Rx side is used to provide this CW signal. The power of the down-converted signal is measured by a spectrum analyzer (HP8592A). The auxiliary components of this measurement system, not shown in Fig. 4.1, include two rotary stages and a PC. The rotary stages work as the bases of our Tx and Rx

and provide different combinations of AoD and AoA under the control of the PC. The PC is also connected with the spectrum analyzer via a general-purpose interface bus (GPIB) cable to remotely acquire and store the measured signal strength.

4.2.2 Power Delay Profile Measurement System

Power delay profile (PDP) measurements record the power distribution over time and require resolving multipath components using their relative delays. One way to do these measurements is using a vector network analyzer, which can offer a timing resolution as high as 0.1 ns [PJJ11]. However, the Tx-Rx separation and measurement frequency are both limited when using a VNA connected to the Tx and Rx. An alternative technique is the spread spectrum channel sounding, in which channels are probed using a spread spectrum signal, such as wideband chirp signals. A chirp signal is essentially a frequency-modulated CW signal whose frequency usually linearly increases or decreases with time. Chirp signals are widely used to achieve high timing/distance resolution in radar applications. When being used for channel sounding, their capability of resolving multipath components increases with the bandwidth. Considering the use of the chirp bandwidth expansion technique [GLR14, ABM04, GDP11], our SGX module can generate an ultra-wideband chirp signal when its input signal is also a chirp signal. Both the center frequency and bandwidth of the input chirp signal are magnified by the same multiplication factor, resulting in the center frequency residing in the desired terahertz range and the bandwidth satisfying the high timing resolution requirement. Additionally, since the probe signal is locally generated at the Tx, this technique has fewer constraints on the Tx-Rx separation and provides greater flexibility regarding the measuring distance.

Figure 4.2 shows the block diagram of our PDP measurement system, which has the following changes from the PAP measurement system. On the Tx side, the synthesized sweeper is replaced by an arbitrary wave generator (AWG70001A). The AWG has a 50 GS/s maximum sampling rate and a 20 GHz maximum analog bandwidth, which is achieved by interleaving signals from two digital-to-analog converters, each working at 25 GS/s. This

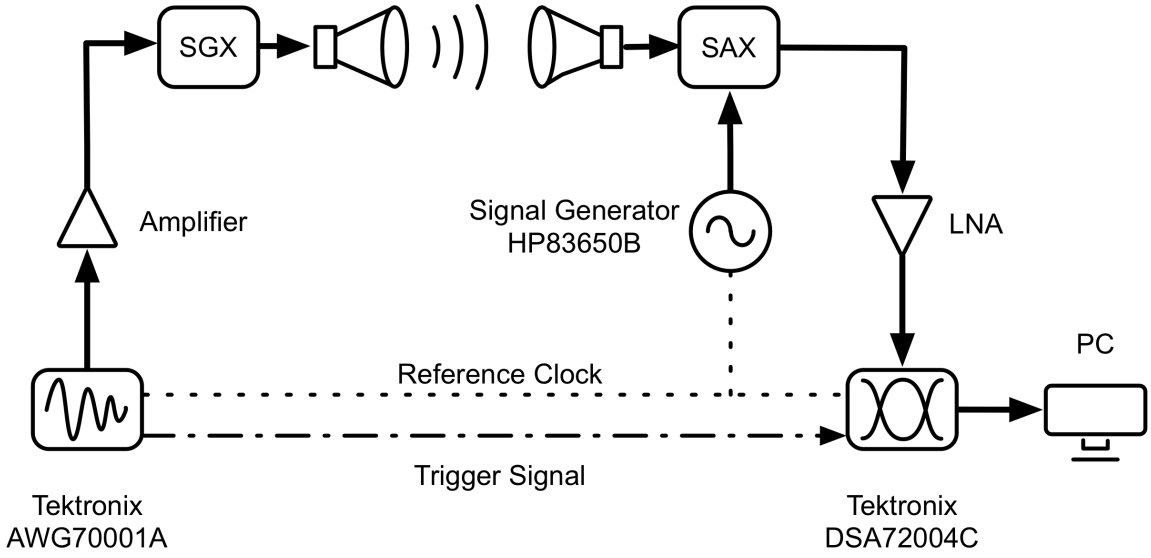

Figure 4.2: Block diagram of the PDP measurement system.

allows us to generate a wideband chirp signal readily by loading the desired chirp samples in the AWG buffer.

Since the generated chirp signal from the AWG has a maximum magnitude of 1 V_{pp}, which is insufficient to drive the SGX module, a 28 dB gain amplifier is used to meet this requirement. On the Rx side, the received signal is amplified by a low-noise amplifier with a 17 dB gain and monitored by a high-speed oscilloscope (DSA72004C). This oscilloscope features an up to 100 GS/s real time sampling rate and an up to 250 mega-sample record length, which enables us to capture the data and perform data processing offline. A digital marker output of the AWG, which is synchronized with the transmitted chirp waveform, is connected to the oscilloscope for triggering data acquisition. By utilizing this trigger signal, we ensure the signal integrity and a common reference time for all captured data. While the physical connection is through a 9-meter coaxial cable, the timing jitter observed by the oscilloscope is below 20 ps. An optical fiber link can be used to carry the trigger signal to perform PDP measurements for larger Tx-Rx separations and to achieve lower timing jitters [DW12, LY03]. All the instruments with internal clocks, including the AWG, the oscilloscope and the synthesized signal generator, are also connected using coaxial cables to

share a common clock reference to pursue the optimal timing performance. The connections between the PC and all instruments are established via Ethernet cables instead of GPIB cables for faster data transfer.

4.3 Measurement Methods

The measurement campaign took place in a conference room at UCLA, whose floor plan is shown in Fig. 4.3. This room measures 9.20 m by 5.98 m. The ceiling is made of suspended acoustic tiles. The walls are constructed with prevalent drywalls. The floor is covered with tiles. Starting from the left, the tables and the door are made of wood. In the center of the room, two blocks of chairs are separated by an aisle. Two whiteboards are mounted side by side on one of the walls. A podium stands at the lower right corner, and a glass window with a metal frame is in the rightmost wall.

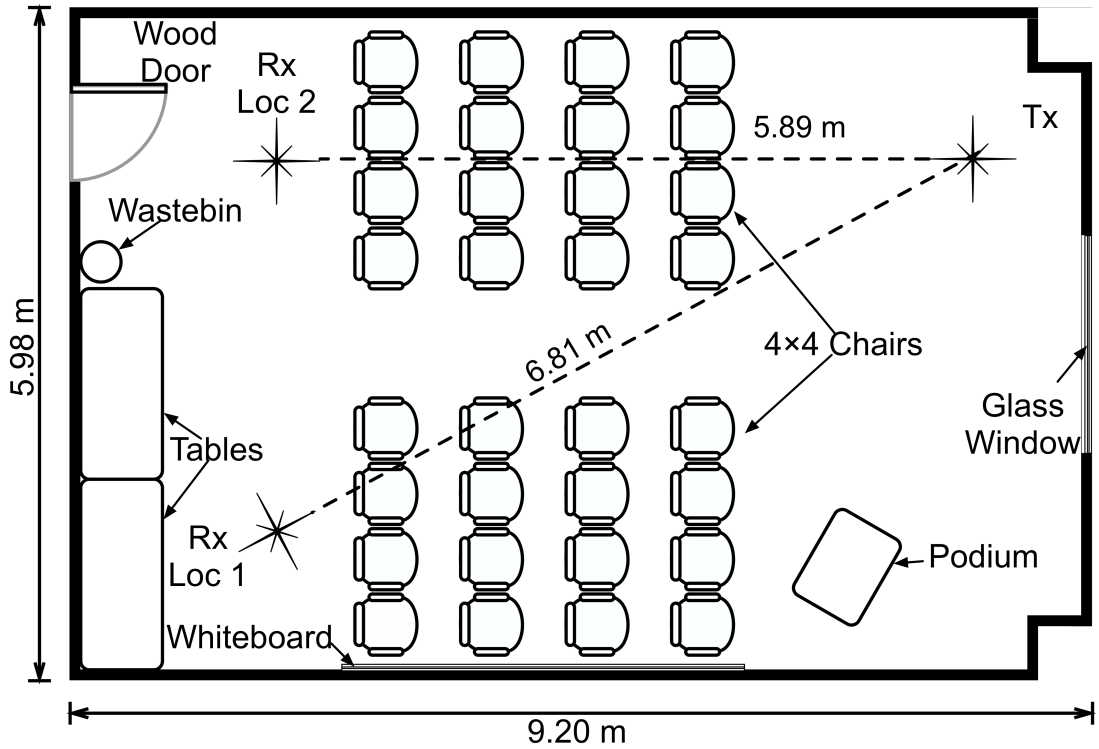

Figure 4.3: Floor plan of the investigated conference room.

The Tx was placed at the upper right corner, and two Rx locations at the upper and lower left corners were investigated. These locations were chosen to take advantage of the room size and examine channels with relatively long distances. While the transmitter can maximize its coverage if mounted on the ceiling, we put both the Tx and Rx on carts with the same heights (1.4 m). The rationale was to have all paths in a 2-D plane and simplify the channels to be examined.

4.3.1 PAP Measurements

For the PAP measurements, to investigate the 350 and 650 GHz bands, the synthesized sweeper on the Tx side was set to output CW RF signals with frequencies of 12.963 and 12.037 GHz, to be multiplied by 27 and 54, respectively. Accordingly, the CW RF signals feeding the signal generator on the Rx side had frequencies of 29.133 and 36.089 GHz, and the respective multiplication factors were 12 and 18. For both spectral windows, the down-converted CW signals were set at a 400 MHz frequency and their power was measured using the spectrum analyzer. The detailed configuration of all system components is summarized in Table 4.1.

To scan all available paths, we programed the rotary stages to rotate both the Tx and Rx in the azimuth from -180 to 180 degrees, with a step size of 3 degrees. At each (AoD, AoA) combination, the power measurement was performed 10 times and the results were transferred to a PC, where the data average was calculated to remove possible time-varying fading. The measured signal powers indicate the relative loss in the signal propagating along different paths. The received signal power P_r is modeled by the well-known link budget equation as

$$P_r = P_t + G_t + G_r - PL, \tag{4.1}$$

where all terms have units in the dB scale, G_t and G_r are the Tx and Rx antenna gains, respectively, and P_t is the Tx power, which varies at different frequencies. To obtain the path losses introduced by the channel only, denoted by PL, we performed calibrations of the measurement system at two frequencies, 350 and 650 GHz. The Tx and Rx were separated

Table 4.1: System Configuration for PAP Measurements

Components		350 GHz	650 GHz
Tx	Synthesized Sweep Signal Generator HP8340A	f=12.963 GHz	f=12.037 GHz
	SGX[1]	AMC(WR9.0) +×3(WR2.8) N=27	AMC(WR9.0) +×2(WR4.3) +×3(WR1.5) N=54
Rx	Synthesized Sweep Signal Generator HP83650B	f=29.133 GHz	f=36.089 GHz
	SAX	MixAMC(WR2.2) N=12	MixAMC(WR1.5) N=18
	Spectrum Analyzer[2] HP8592A	f=400 MHz RBW=300 kHz	f=400 MHz RBW=300 kHz

[1] ×3 and ×2 denote VDI frequency triplers and doublers respectively, and N is the multiplication factor.

[2] RBW stands for the resolution bandwidth of the spectrum analyzer.

by 0.3 m and were carefully aligned using a laser pointer to receive the maximum power. At such a short distance, it is reasonable to assume that there are no significant multipath components. It is worth noting that the received signal levels are at least 15 dB below the saturation level, ensuring that no nonlinearity impacts the measurements. Since small variations in the position of Tx and Rx were not resulting in any observable change in the measured data, the impact of potential standing waves formed between the Tx and Rx seem to be negligible. Therefore, the path loss can be calculated using the free space path loss equation, given as

$$PL_{FS} = 20\log_{10}(d) + 20\log_{10}(f) + 20\log_{10}\left(\frac{4\pi}{c}\right), \tag{4.2}$$

where d denotes the Tx and Rx separation, f is the carrier frequency, and c represents the speed of light. The received signal power during calibration is also calculated from the free space path loss equation as

$$P_{r,cal} = P_t + G_t + G_r - PL_{FS}. \tag{4.3}$$

By subtracting (4.3) from (4.1), the path loss values are calculated and used to form the PAP of the terahertz channel.

$$PL = P_r - P_{r,cal} + PL_{FS}. \tag{4.4}$$

4.3.2 PDP Measurements

For the PDP measurements, on the Tx side, the AWG generates the probe signal, which is a train of 2000 chirp signals with a 200 ns period and a 50% duty cycle. The frequency of each chirp signal was set to increase linearly, and the 100-ns separation between consecutive chirps was sufficiently long to include all multipath components. For the 350 GHz band, the chirp signal ranged from 12.778 GHz to 13.148 GHz. Based on the theory of the chirp bandwidth expansion technique, with a multiplication factor of 27, we had a 10 GHz bandwidth chirp signal centered at 350 GHz originating from the Tx. Similarly, for the 650 GHz band, the chirp signal was swept from 11.944 GHz to 12.130 GHz and a multiplication factor of 54 was used.

On the Rx side, in both cases, we aimed to down-convert the received chirp signal to a common lower frequency range, from 1 GHz to 11 GHz. Therefore, the frequency of the CW signal feeding the SAX was 28.667/35.778 GHz and multiplied by 12/18 when operating in the 350/650 GHz band. A built-in low-pass filter with a cut-off frequency at 12 GHz was also used to reject unnecessary noise as well as harmonics. The down-converted signal was recorded and transferred to the PC upon being triggered. Only a subset of the resolvable paths was investigated on the basis of the PAP measurement results. The detailed configuration of all system components is summarized in Table 4.2.

Table 4.2: System Configuration for PDP Measurements

Components		350 GHz	650 GHz
Tx	AWG[1]	Chirp signal f_L=12.778 GHz f_H=13.148 GHz T=100 ns	Chirp signal f_L=11.944 GHz f_H=12.130 GHz T=100 ns
	SGX	AMC(WR9.0) +×3(WR2.8) N=27	AMC(WR9.0) +×2(WR4.3) +×3(WR1.5) N=54
Rx	Synthesized Sweep Signal Generator HP83650B	f=28.667 GHz	f=35.778 GHz
	SAX	MixAMC(WR2.2) N=12	MixAMC(WR1.5) N=18
	Oscilloscope[2] DSA72004C	f_s=50 GHz RL=20 Msamples	f_s=50 GHz RL=20 Msamples

[1] The lower frequency limit f_L, the higher frequency limit f_H, and the duration T of the chirp signal.

[2] Oscilloscope sampling frequency f_s, and the total number of samples stored in the buffer RL.

Multiple chirp signals were averaged to improve the SNR. As seen in Fig. 4.4, the signal shown is an example chirp signal measured at 350 GHz. In the time domain (see Fig. 4.4a), the received chirp signal was buried under the noise floor and became distinguishable after averaging 2000 chirp signals. In the frequency domain (see Fig. 4.4b), the chirp signal frequency varies from 1 to 11 GHz, corresponding to carrier frequencies in the range of 345-355 GHz. It can be observed quantitatively that the SNR was significantly improved by approximately 33 dB given the 2000 chirp signal captures. It should be noted that the mixing operation may introduce a phase difference between the consecutive captured chirp signals, which will result in degradation of the signal strength after averaging, yielding no improvement of the SNR.

However, the phase difference can be estimated, and the improvement remains when a phase correction is applied. In our measurements, the relative phase difference between consecutive chirps was an exact multiple of 2π; thus, there was no need for phase correction.

The impulse response of the channel was extracted from the averaged chirp signals by utilizing a deconvolution-based approach. In the frequency domain, the received signal can be expressed as

$$Y(f) = X(f)H(f)H_{sys}(f), \tag{4.5}$$

where $H(f)$,$X(f)$ and $H_{sys}(f)$ are, respectively, the frequency responses of the channel, the probe signal, the received signal, and the system including the AWG, amplifiers and the oscilloscope. Since the frequency response of the measurement system is not readily accessible, we performed a short-distance LoS calibration similar to the PAP measurements, to calculate the channel response. These calibration measurements provided a reference described by

$$Y_{cal}(f) = X(f)H_{cal}(f)H_{sys}(f), \tag{4.6}$$

where $H_{cal}(f)$ is the frequency response of the calibration channel. By normalizing the measured frequency response of the received signal with the calibrated reference, we obtained

$$H'(f) = \frac{Y(f)}{Y_{cal}(f)} = \frac{H(f)}{H_{cal}(f)}, \tag{4.7}$$

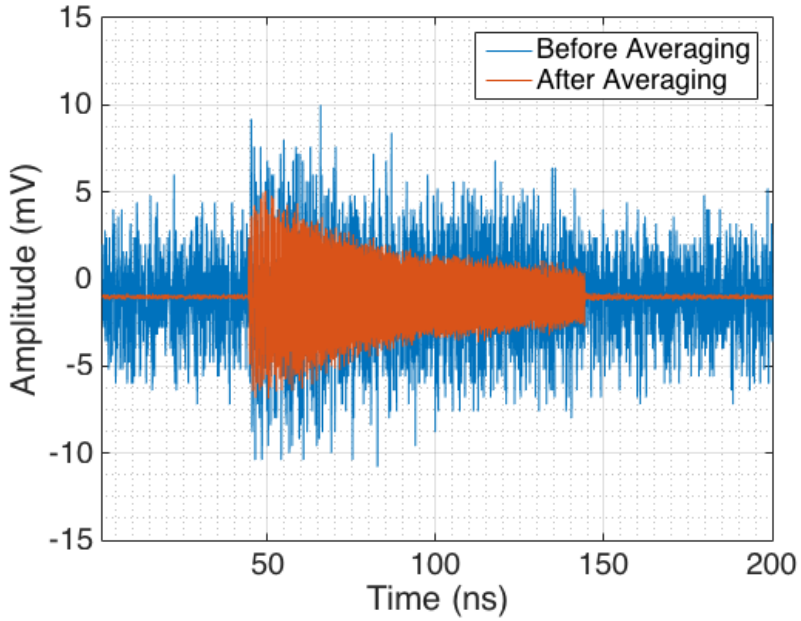

(a)

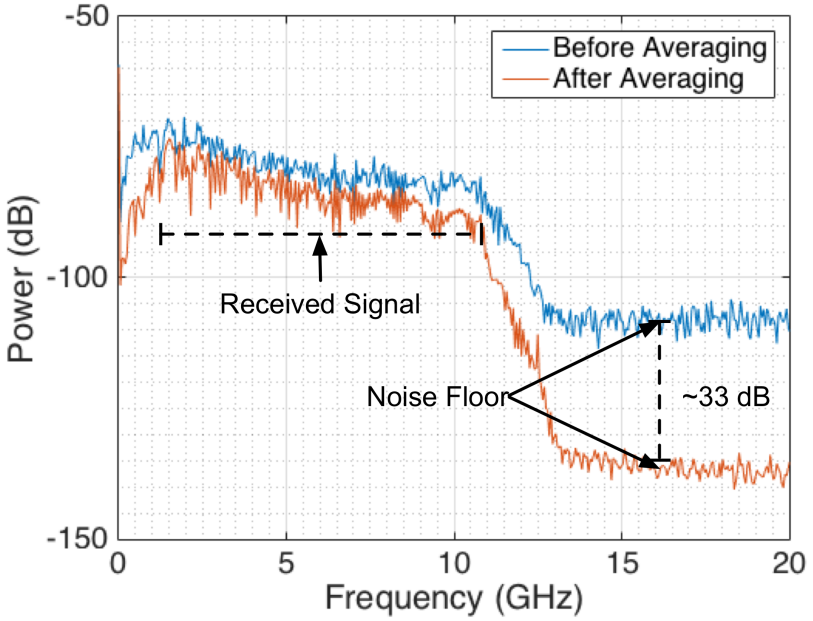

(b)

Figure 4.4: The improvement of SNR by averaging in time and frequency domains.

which is the frequency response of the examined channel divided by that of the calibration channel. In the time domain, this approach can be interpreted as deconvolving the response of the calibration channel from the measured channel, which amounts to a simple scaling and time shifting. The scaling factor can be evaluated using the free space path loss equation (4.2), and the time shifting involves the wave propagation time to travel 0.3 m. The channel frequency response $H(f)$ was obtained by revoking the scaling and shifting from $H'(f)$. Therefore, the inverse transform of $H(f)$ was computed as the measured channel impulse response $h(t)$ and the PDP was constructed by composing the power of the measured impulse responses as $|h(t)|^2$.

The division in (4.7) could be numerically unstable if there are values close to zero in $Y_{cal}(f)$. Additionally, analogous to zero-forcing channel equalization, the results are sensitive to noise if $Y_{cal}(f)$ fails to maintain a high SNR over the investigated spectrum. In our measurements, the received signals had frequency components ranging from 1 GHz to 11 GHz, but the sampling rate was 50 GS/s. Thus, before taking the ratio, we down-converted the received signal to the baseband and down-sampled it by 5 to avoid the aforementioned instability issue.

4.4 Measurement Results

4.4.1 Power Angle Profiles

The measured PAP results are illustrated in Fig. 4.5 and Fig. 4.6, for carrier frequencies 350 GHz and 650 GHz respectively. For each carrier frequency, two receiver locations are presented in two subfigures: the top one (a) is for Rx location 1; and the bottom one (b) is for location 2. The horizontal and vertical axes are the AoA and AoD values, respectively. Both angles are given with respect to the LoS path ranging from -180 to 180 degrees, and a positive angle corresponds to a clockwise rotation. Different colors represent different path loss levels based on the color bar on the side. When an angle combination provides a sufficient received signal power, it is associated with a distinguishable color. When the

received signal power falls below the noise floor and is indistinguishable, the corresponding points are painted with the same white color.

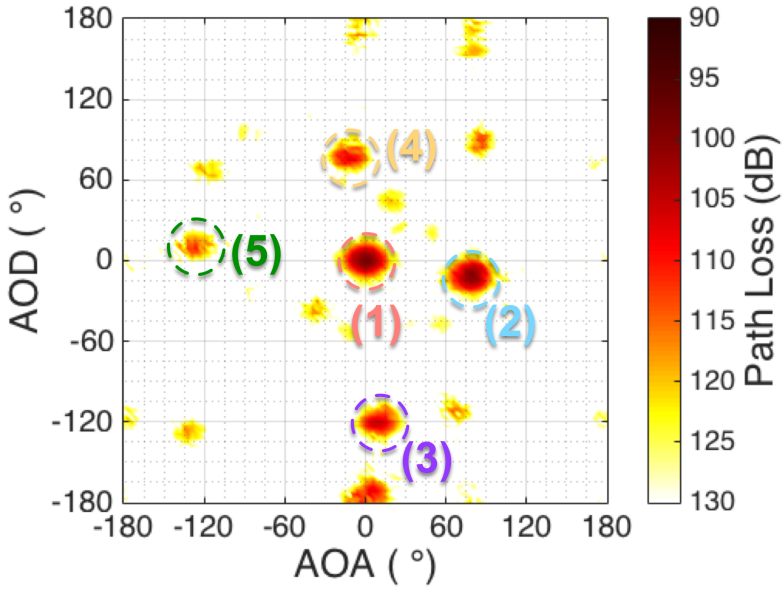

(a)

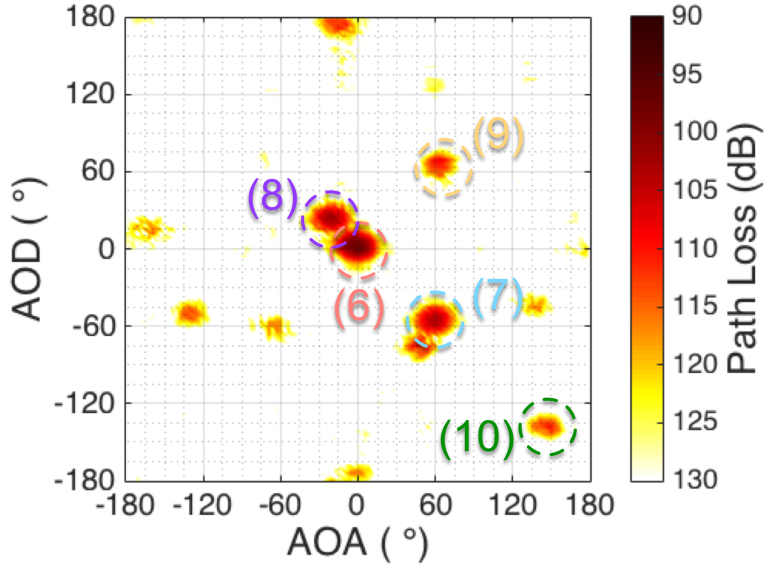

(b)

Figure 4.5: The measured power angle profiles for 350 GHz carrier frequency.

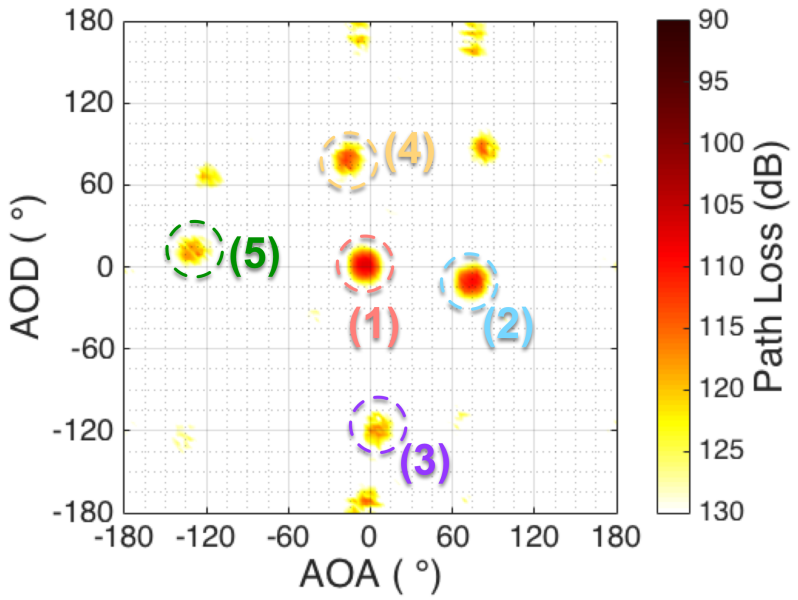

(a)

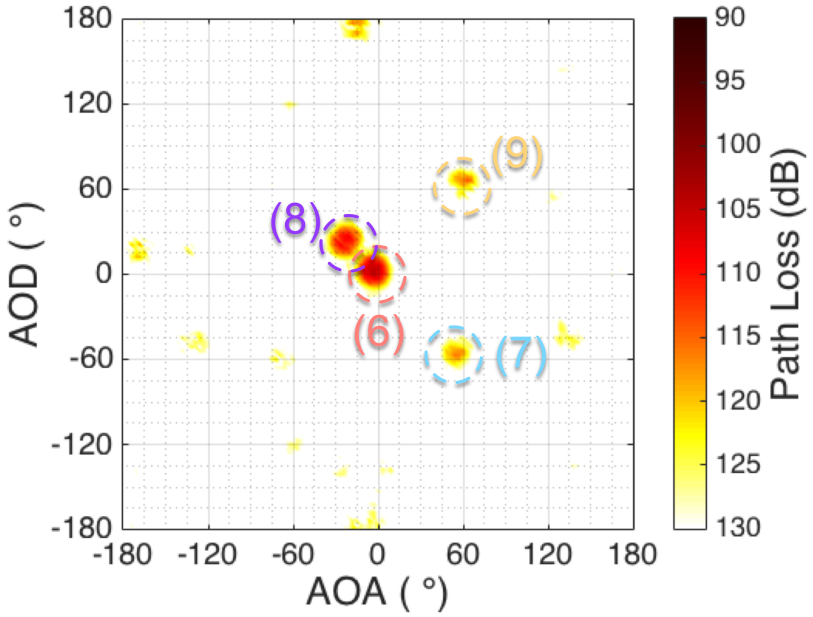

(b)

Figure 4.6: The measured power angle profiles for 650 GHz carrier frequency.

Each spot is identified as a spatially resolvable path, and we associate it with the room geometry by tracing the terahertz wave propagation in the scaled floor plan (Fig. 4.7). In Fig. 4.7, Each dashed line represents a resolvable path in the corresponding color as shown in Fig. 4.5 and Fig. 4.6. It should be noted that the utilized Tx/Rx horn antennas have a Gaussian beam pattern with a 12-degree HPBW, providing a high angular resolution that is needed to distinguish between closely-spaced paths. For each path, the trace originates from the Tx at the corresponding AoD, is then reflected if it hits an object, and is captured by the Rx exactly at the expected AoA. Thus, we are aware of how far the wave has traveled, how many reflections it has undergone, and what the reflectors are. The design implication is that as long as prior knowledge of a specific propagation environment is available, the paths can be estimated via ray tracing [PKJ13], rather than performing a thorough channel measurement campaign. As examples, for each Rx location, 5 resolvable paths and their corresponding spots are marked in the floor plan and PAP.

Among these resolvable paths, paths 1 and 6 are the LoS paths at the respective Rx locations, and they provide a strong signal strength due to the absence of any obstruction and having the shortest propagation distance. The other NLoS paths are found to experience various numbers of reflections up to 3, which is defined as the reflection order. The first-order reflections, such as the paths labeled from 2 to 5, should be considered first as backups when LoS path 1 is blocked. They offer negligible power degradation relative to the LoS path and are unlikely to be obstructed simultaneously in an uncrowded room. In contrast, the paths with higher reflection orders usually suffer from a longer propagation distance and higher loss introduced by multiple reflections. Thus, they show up in the PAP as lower contrast spots. The whiteboard appears to be a very strong reflector, which leads to some higher-order paths, such as paths 9 and 10, which are also potential NLoS backup paths.

Table 4.3 summarizes the spatial characteristics of the total 10 investigated paths. To show the impact of switching to a NLoS path in the case of obstruction of the LoS path, we consider a data communication link with a 1 GHz bandwidth and estimate the channel capacities for the studied LoS and NLoS paths. Channel capacity is defined as the maximum

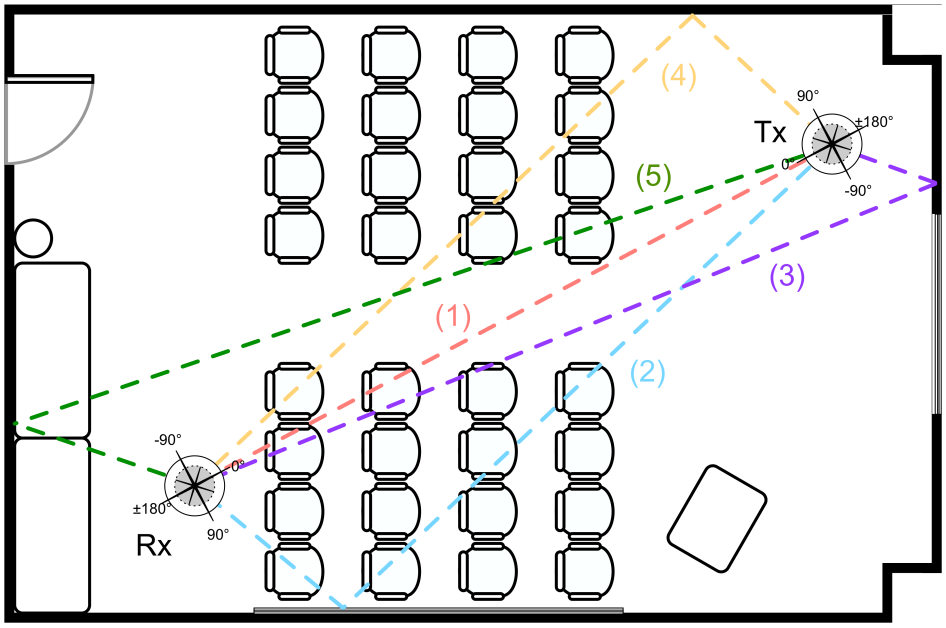

(a)

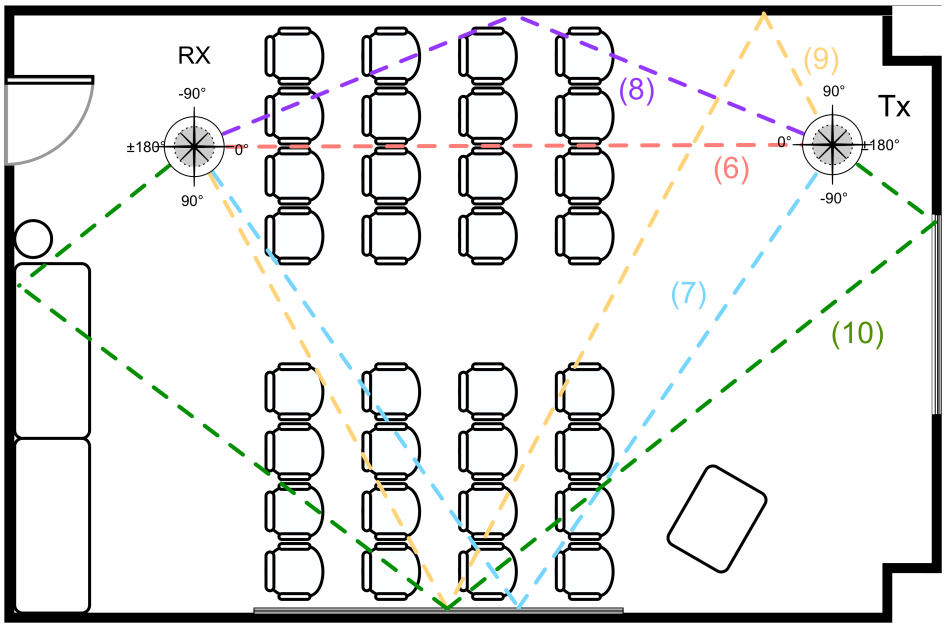

(b)

Figure 4.7: The floor plans with the identified paths marked for two Rx locations.

Table 4.3: Spatial Characteristics of the Investigated Paths

Paths	AOD (°)	AOA (°)	Order	Length (m)	Loss (dB)		SNR[1] (dB)		Rate[1] (Gbit/s)	
					350 GHz	650 GHz	350 GHz	650 GHz	350 GHz	650 GHz
(1)	0	0	0	6.81	99.2	105.0	1.5	-9.5	1.27	0.15
(2)	-9	78	1	8.18	102.1	108.4	-1.4	-12.9	0.79	0.07
(3)	-120	9	1	9.10	107.1	111.1	-6.2	-15.6	0.30	0.04
(4)	75	-12	1	8.27	108.1	108.7	-7.4	-13.2	0.24	0.07
(5)	9	-126	1	9.84	114.3	114.9	-13.6	-19.4	0.06	0.02
(6)	0	0	0	5.89	101.0	103.1	-0.3	-7.6	0.95	0.23
(7)	-54	60	1	10.96	107.2	109.7	-6.5	-14.2	0.29	0.05
(8)	24	-21	1	6.40	102.2	106.6	-1.5	-11.1	0.77	0.11
(9)	69	63	2	13.06	111.6	116.1	-10.9	-20.6	0.11	0.01
(10)	-138	147	3	15.35	124.6	>130	-23.9	N/A	0.01	N/A

[1] Extrapolated value when the bandwidth of the system is set to 1 GHz.

data rate a stationary wireless link can support without error [SWP12], calculated as

$$C = B \log_2 (1 + SNR), \tag{4.8}$$

where B is the channel bandwidth and SNR is the signal-to-noise ratio. In our case, the bandwidth is simply 1 GHz as we assumed. To obtain a reasonable estimate of the SNR value, we evaluate it using

$$SNR = \frac{P_r}{P_n} = \frac{P_t G_t G_r PL}{N_0 B}, \tag{4.9}$$

where the received signal power and noise power are denoted by P_r and P_n, respectively. It can be noted from (4.9) that does not depend on the bandwidth, hence the received power from the PAP measurements are used for our calculations. However, since the resolution bandwidth of the spectrum analyzer was set to 300 kHz in our measurements, the noise power levels in our calculations should be adjusted according to the assumed bandwidth of 1 GHz. Assuming an identical noise power spectral density, the measured noise power levels of -98 dBm and -89 dBm at the 350 and 650 GHz bands are increased by 35.23 dB, $10 \times \log_{10} \left(\frac{1\text{GHz}}{300\text{kHz}}\right)$, to -62.7 dBm and -53.8 dBm, respectively. As predicted, when switching from a LoS path (e.g. path 1) to a NLoS path (e.g. path 2), the maximum data rate is reduced (by 48% and 53% for the 350 GHz and 650 GHz bands, respectively).

4.4.2 Power Delay Profiles

The PDP measurement results are derived from the impulse responses of each resolvable path, as shown in Fig. 4.8 and Fig. 4.9 for carrier frequencies 350 GHz and 650 GHz. For each carrier frequency, two receiver locations are presented in two subfigures: the top one (a) is for Rx location 1; and the bottom one (b) is for location 2. Each colored trace describes the power distribution over time of a spatially resolvable path. They are gathered to show the relative power and delay between each path. The horizontal axis is the delay with a 0.1 ns resolution, as the investigated bandwidth is 10 GHz. Due to such a high timing resolution, two multipath components can be resolved in the PDP if their propagation distances differ by as little as 3 cm. The vertical axis is the power of each multipath component relative to the Tx power in the dB scale.

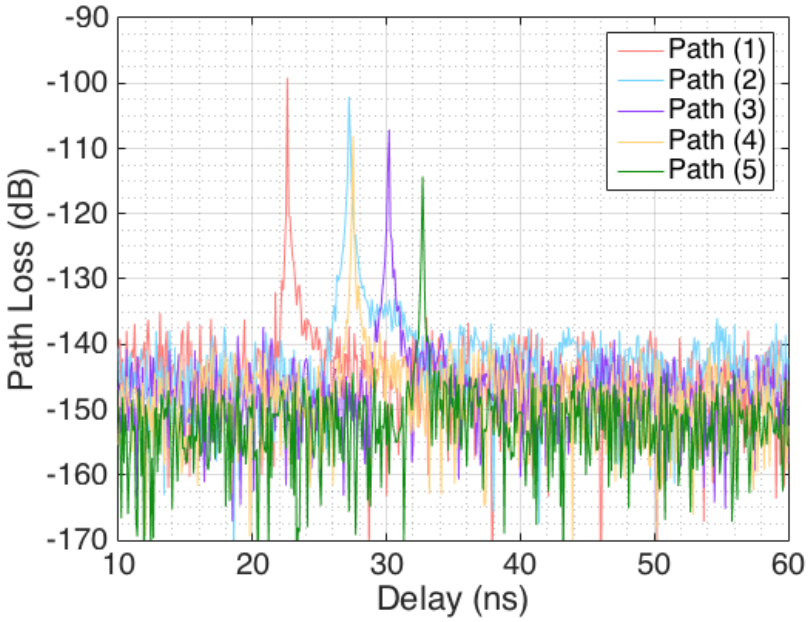

(a)

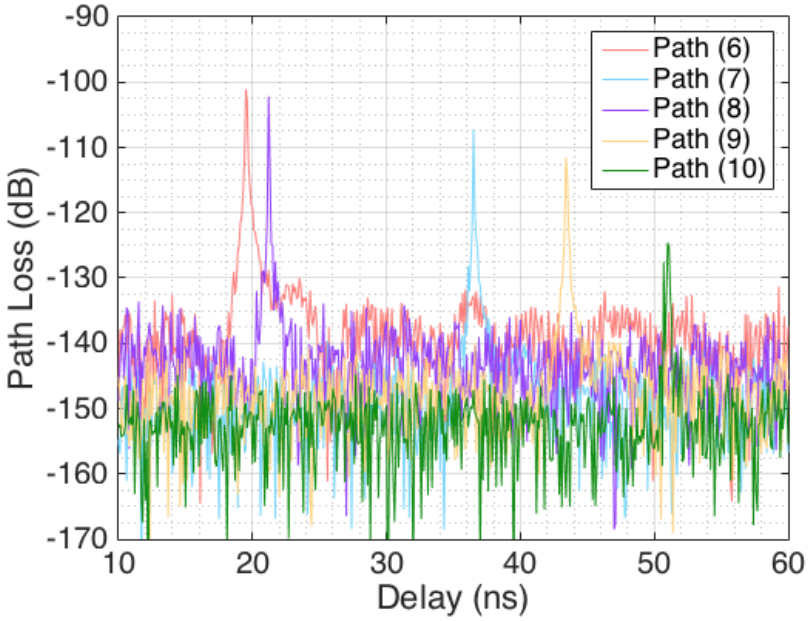

(b)

Figure 4.8: The measured power delay profiles for 350 GHz carrier frequency.

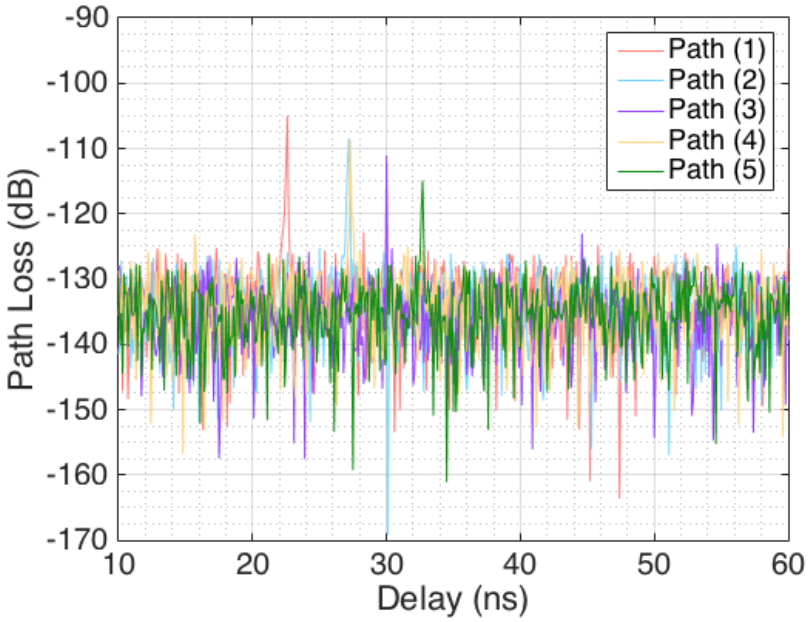

(a)

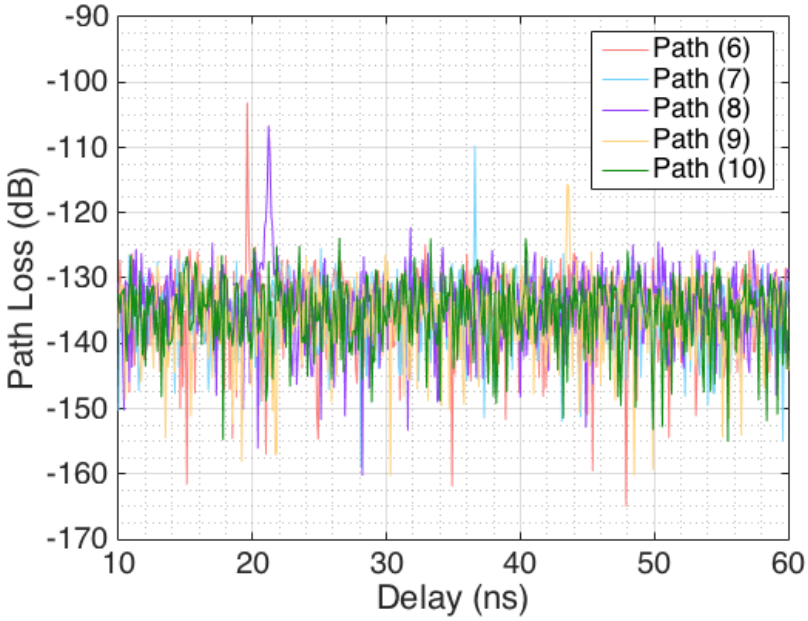

(b)

Figure 4.9: The measured power delay profiles for 650 GHz carrier frequency.

Every path has a single narrow peak, and no significant second peak is observed, due to the use of highly directional antennas. The diffusive reflections from rough surfaces may result in broadening of the peaks, which is not observed in our measured results. Similar to the PAP measurement results, the path loss of path 10 is out of the dynamic range of our measurement system at 650 GHz.

To quantitatively characterize the channel dispersion in time, the mean excess delay $\bar{\tau}$ and the root mean square (RMS) delay spread σ_τ of each path are evaluated based on

$$\bar{\tau} = \frac{\sum p_i \tau_i}{\sum p_i}, \tag{4.10}$$

$$\sigma_\tau = \sqrt{\frac{\sum p_i \tau_i^2}{\sum p_i} - \left(\frac{\sum p_i \tau_i}{\sum p_i}\right)^2}, \tag{4.11}$$

where p_i and τ_i are, respectively, the power and delay of the ith component of the impulse response.

The RMS delay spread quantifies the temporal spreading effect of the wireless channel and is the parameter that determines the complexity of the required equalization. As a rule of thumb, for a given RMS delay spread σ_τ and symbol duration T_s, the number of coefficients needed in the equalizer to remove ISI is σ_τ / T_s. RMS delay spread also determines the coherence bandwidth B_c, defined as the frequency range over which the channel can be considered flat or highly correlated.

$$B_c = \frac{0.2}{\sigma_\tau}, \tag{4.12}$$

where the constant in the numerator may vary depending on the specific design requirements.

Figure 4.10 shows the histograms of the estimated and values for path 7 when capturing data over 0.4 ms, indicating a larger spread in the extracted and values for the 650 GHz channel. Table 4.4 summarizes the temporal characteristics of the total 10 investigated paths. The high correlation between the mean excess delays and the expected propagation time justifies our impulse response measurement method. The existence of multiple NLoS paths with sufficient signal powers allows the maintenance of robust communication despite possible shadowing between the Tx and Rx. With a high directionality of both the Tx and

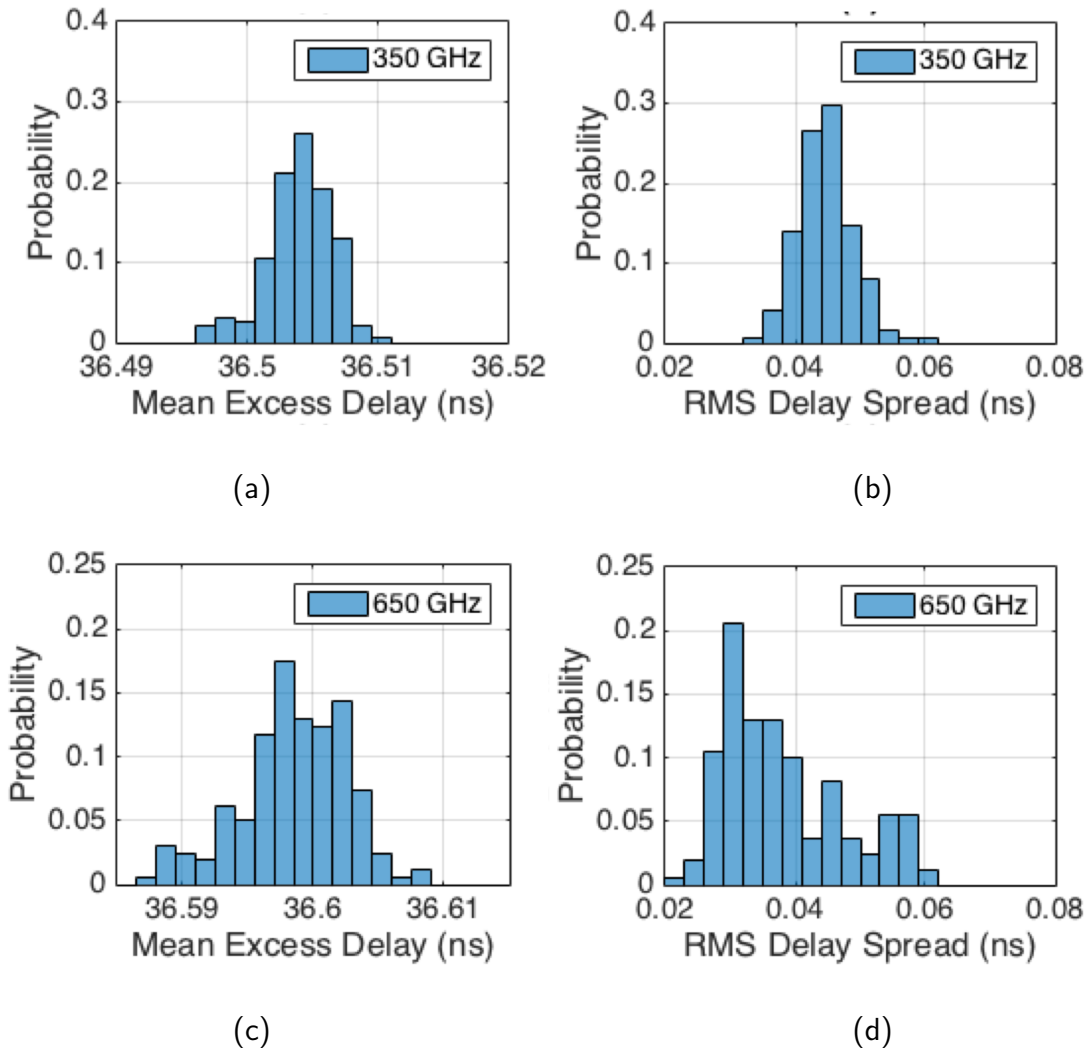

Figure 4.10: The histograms of the estimated mean excess delay and RMS delay spread for path (7) at 350 GHz and 650 GHz.

Table 4.4: Temporal Characteristics of the Investigated Paths

Paths	AOD (°)	AOA (°)	Order	TOF[1] (ns)	Mean excess delay (ns)		RMS delay spread (ns)		Coherence Band-width (GHz)	
					350 GHz	650 GHz	350 GHz	650 GHz	350 GHz	650 GHz
(1)	0	0	0	22.70	22.60	22.58	0.02	0.06	10.10	3.3
(2)	-9	78	1	27.27	27.22	27.16	0.06	0.06	3.3	3.3
(3)	-120	9	1	30.33	30.18	30.00	0.06	0.02	3.3	10.0
(4)	75	-12	1	27.57	27.50	27.32	0.04	0.06	5.0	3.3
(5)	9	-126	1	32.80	32.70	32.68	0.04	0.06	5.0	3.3
(6)	0	0	0	19.63	19.54	19.60	0.08	0.02	2.5	10.0
(7)	-54	60	1	36.53	36.50	36.60	0.04	0.02	5.0	10.0
(8)	24	-21	1	21.33	21.20	21.22	0.04	0.06	5.0	3.3
(9)	69	63	2	43.53	43.44	43.54	0.08	0.06	2.5	3.3
(10)	-138	147	3	51.17	51.04	N/A	0.08	N/A	2.5	N/A

[1] TOF is short for time of flight, which the THz wave takes to arrive at the receiver.

Rx, the multipath components are significantly filtered out spatially. The calculated delay spreads for each path are found to be less than 80 ps for both 350 GHz and 650 GHz bands. No equalization is required to address the ISI when the symbol duration is greater than the RMS delay spread, simplifying the terahertz transceiver system design.

4.5 Summary

To design terahertz wireless indoor communication systems, we have extended knowledge of wireless channels from the 350 GHz to 650 GHz atmospheric transmission band by conducting an extensive channel measurement campaign in a typical indoor environment. From the measurement results, we have observed two main facts regarding terahertz wave propagation, which significantly affect the requirements for designing an indoor terahertz communication system.

First, the PAP measurement results have shown the existence of multiple NLoS paths with sufficient power at both 350 GHz and 650 GHz bands. These paths are valuable supplements to the direct LoS path in the case of shadowing, at the expense of some reduction at the maximum achievable data rate. Implementing a smart antenna array with adaptive beams [HYW16] and developing an adaptation and tracking algorithm are needed to maintain robust terahertz communication. The measurement results are used to calculate the reduction in the 650 GHz channel capacity in comparison with that of the 350 GHz channel for both LoS and NLoS paths.

Second, based on the PDP measurement results, no significant multipath components have been observed within any spatially resolvable path at both 350 GHz and 650 GHz bands over a 10 GHz bandwidth. With high directionality, a large delay spread is avoided and the channel dispersion is limited. Our measurement results in a typical indoor environment predict that no equalization is required to address the ISI when the symbol duration is greater than 80 ps at both 350 GHz and 650 GHz bands.

There are some other observations worth addressing as well. Because of the strong cor-

relation between the resolvable paths and the propagation environment, ray tracing appears to be an efficient method for evaluating site-specific channels at both 350 GHz and 650 GHz bands. The specular reflection contributes most to the NLoS paths; hence, the characterization of construction materials is necessary to yield accurate ray tracing results [PJM07].

CHAPTER 5

Conclusions

To wrap up this dissertation, a selection of practical issues of interference alignment and THz communication are extensively studied to pave the road for future development in real life. Due to the dramatic changes in the ways people create and share information in the recent decades, a demand for wireless communication systems with over 100 Gb/s data rate has been envisioned. Promising techniques, such as interference alignment (IA) and THz communication and many more, have been devised by researchers to fulfill such expectation. In theory, given ideal assumptions, they show extraordinary increase in the promised data rate relative to current wireless communication systems. Nevertheless, because of the hardware impairments, many practical challenges have to be addressed before bringing these advanced techniques from theory to practice. During my four-year Ph.D. program, three practical challenges have been addressed. The methods we have proposed and the experiments conducted for validation are all compiled in this dissertation.

5.1 Summary of Contributions

In chapter 2, we consider the synchronization and channel estimation problem associated with enabling IA, by which multiple communication links can be supported simultaneously reusing the same channel. Before achieving IA, in view of the uncoordinated interference, a concurrent synchronization and channel estimation mechanism with robustness against co-channel interference is needed. We start by deriving the maximum-likelihood expressions for optimal estimators of frequency offset, timing offset, and channel. Then, it is realized that such estimators are infeasible in practice for requiring a computationally costly 2-D

search. To reduce the complexity and make it practical, we propose a Zadoff-Chu sequence based pilot structure. By utilizing its unique properties, the 2-D search problem can be converted into two 1-D search problems. Experimental results verify the great performance of our proposed method in terms of both the residual frequency offset and the sum rate of an IA network.

In chapter 3, we focus on the channel reciprocity in time division duplex (TDD) networks, which is assumed by a large number of distributed interference alignment algorithms. The physical channel is reciprocal, but the channel considered by IA is not, because it also involves the radio frequency (RF) front-ends of the transceiver, which are different circuits for transmit and receive modes individually. The difference between the two circuits yields mismatch between the forward and backward channels. Given the mutual coupling effect of the antenna array, the channel's non-symmetry is further complicated. In this work, we provide the modeling of the non-reciprocity for the TDD MIMO channels, and propose a corresponding calibration method to minimize the mismatch. Experimental validation has been conducted with classic IA algorithms. The results highlight the indispensability of the reciprocity calibration for approaching the network capacity promised by IA.

In chapter 4, with a view to assessing THz communication system design requirements in practice, we measure the channels for both 350 GHz and 650 GHz carrier frequencies in a typical indoor environment. To obtain the spatial and temporal characteristics of the channel, the power angle profile (PAP) and the power delay profile (PDP) are measured using our proposed measurement systems and methods. Multiple spatially resolvable paths are observed at both 350 GHz and 650 GHz carrier frequencies. The signal-to-noise ratio (SNR) of the received signal through the non-line-of-sight (NLoS) paths is sufficient to enable robust communication when the direct line-of-sight (LoS) path is blocked. The channel dispersion characterization over a 10 GHz bandwidth shows that the delay spreads for the resolved LoS and NLoS paths are less then 80 ps for both bands. Therefore, no complicated equalizer is required to compensate the channel dispersion, which greatly simplifies the THz transceiver design.

5.2 Future Work

5.2.1 Prototyping the First Real-time IA System via Channel Reciprocity

For interference alignment, there has been some effort to implement interference alignment in real life, but they all are limited to sharing the channel information via feedback. It is fine to do feedback for a small scale network, i.e. 3 users, but it becomes impractical as the number of users increases. Assigning exclusive resources to each user for feedback is quite inefficient as users are not likely to be strong interference sources all at the same time. In comparison, the other group of IA strategies that utilizes channel reciprocity is more efficient and flexible. Although the channel reciprocity based approached have been proposed for quite a while, there is not any successful report on implementing such algorithms yet. In our attempt to build up the first channel reciprocity based IA network, we gradually realized the necessity of addressing the practical challenges induced from the hardware impairments. Especially for the channel reciprocity, the non-reciprocity from the antenna mutual coupling effect has been ignored by many researchers. This could have failed some of the trials so far. Since we have addressed not only the non-reciprocity issue, but also practical synchronization and channel estimation challenges, we are closer to bringing the reciprocity-based IA from theory to practice. One possible practical challenge to be addressed could be the large overhead, which makes the whole system vulnerable to fast time-varying channels.

5.2.2 Indoor Communication Link with Smart Massive Antenna Array

It is still in the early phase of designing a robust high speed THz indoor communication system. There are many practical issues that need to be resolved. Our indoor channel measurements have revealed the fact that, by utilizing highly directional antennas, NLoS paths with sufficient signal strength are available as backups, and the multipath effect could be mitigated by the spatial gain. Nevertheless, it also has posed a problem: is there a smart way to dynamically exploit the optimal available channel? In our current experiments, we rely on horn antennas for high directional and mechanical pan stage for various channels.

A more favoured approach is to implement a THz antenna array with a massive amount of antenna elements. A very sharp beam can be formed to provide tremendous beamforming gain thanks to the sub-millimeter THz wavelength. In addition, it becomes possible to adjust the beam electronically. More advanced algorithms could be devised to track the changing channel and smartly stay on the channel with the highest signal quality. With the development of the THz technology, smaller THz components with high radiation power and high sensitivity are going to make it happen in the near future.

REFERENCES

[ABM04] Albert Aguasca, Antoni Broquetas, Jordi J Mallorquí, and Xavier Fabregas. "A solid state L to X-band flexible ground-based SAR system for continuous monitoring applications." In *IGARSS 2004. 2004 IEEE International Geoscience and Remote Sensing Symposium*, volume 2, pp. 757–760. IEEE, 2004.

[Bal16] Constantine A Balanis. *Antenna theory: analysis and design*. John wiley & sons, 2016.

[BCK03] André Bourdoux, Boris Come, and Nadia Khaled. "Non-reciprocal transceivers in OFDM/SDMA systems: Impact and mitigation." In *Radio and Wireless Conference, 2003. RAWCON'03. Proceedings*, pp. 183–186. IEEE, 2003.

[BHP14] Christopher W Berry, Mohammad R Hashemi, Sascha Preu, Hong Lu, Arthur C Gossard, and Mona Jarrahi. "High power terahertz generation using 1550 nm plasmonic photomixers." *Applied Physics Letters*, **105**(1):011121, 2014.

[BRB14] Francisco Lázaro Blasco, Francesco Rossetto, and Gerhard Bauch. "Time interference alignment via delay offset for long delay networks." *IEEE Transactions on Communications*, **62**(2):590–599, 2014.

[Chu72] David Chu. "Polyphase codes with good periodic correlation properties (corresp.)." *IEEE Transactions on information theory*, **18**(4):531–532, 1972.

[CJ08] Viveck R Cadambe and Syed Ali Jafar. "Interference alignment and spatial degrees of freedom for the k user interference channel." In *2008 IEEE International Conference on Communications*, pp. 971–975. IEEE, 2008.

[DSP15] Guillaume Ducournau, Pascal Szriftgiser, Fabio Pavanello, Emilien Peytavit, Mohammed Zaknoune, Denis Bacquet, Alexandre Beck, Tahsin Akalin, and Jean-François Lampin. "THz communications using photonics and electronic devices: the race to data-rate." *Journal of Infrared, Millimeter, and Terahertz Waves*, **36**(2):198–220, 2015.

[DW12] Amir Dezfooliyan and Andrew M Weiner. "Evaluation of time domain propagation measurements of UWB systems using spread spectrum channel sounding." *IEEE Transactions on Antennas and Propagation*, **60**(10):4855–4865, 2012.

[DZZ14] Guang-long Du, Wei-xia Zou, Zheng Zhou, and Jian-han Liu. "On feasibility of linear interference alignment for single-input–single-output multi-frequency interference channel." *IET Communications*, **8**(12):2207–2212, 2014.

[EH12] Omar El Ayach and Robert W Heath. "Interference alignment with analog channel state feedback." *IEEE Transactions on Wireless Communications*, **11**(2):626–636, 2012.

[ELH12] Omar El Ayach, Angel Lozano, and Robert W Heath. "On the overhead of interference alignment: Training, feedback, and cooperation." *IEEE Transactions on Wireless Communications*, **11**(11):4192–4203, 2012.

[EPH13] Omar El Ayach, Steven W Peters, and Robert W Heath. "The practical challenges of interference alignment." *IEEE Wireless Communications*, **20**(1):35–42, 2013.

[ESB98] Ove Edfors, Magnus Sandell, J-J Van de Beek, Sarah Kate Wilson, and Per Ola Borjesson. "OFDM channel estimation by singular value decomposition." *IEEE Transactions on communications*, **46**(7):931–939, 1998.

[FZF13] Hamed Farhadi, Ali A Zaidi, Carlo Fischione, Chao Wang, and Mikael Skoglund. "Distributed interference alignment and power control for wireless MIMO interference networks with noisy channel state information." In *2013 First International Black Sea Conference on Communications and Networking (BlackSeaCom)*, pp. 23–27. IEEE, 2013.

[GCG11] José Antonio García-Naya, Luis Castedo, O González, David Ramírez, and Ignacio Santamaria. "Experimental evaluation of interference alignment under imperfect channel state information." In *2011 19th European Signal Processing Conference*, pp. 1085–1089. IEEE, 2011.

[GCJ08] Krishna Gomadam, Viveck R Cadambe, and Syed A Jafar. "Approaching the capacity of wireless networks through distributed interference alignment." In *IEEE GLOBECOM 2008-2008 IEEE Global Telecommunications Conference*, pp. 1–6. IEEE, 2008.

[GCJ11] Krishna Gomadam, Viveck R Cadambe, and Syed A Jafar. "A distributed numerical approach to interference alignment and applications to wireless interference networks." *IEEE Transactions on Information Theory*, **57**(6):3309–3322, 2011.

[GDP11] Eyal Gerecht, Kevin O Douglass, and David F Plusquellic. "Chirped-pulse terahertz spectroscopy for broadband trace gas sensing." *Optics Express*, **19**(9):8973–8984, 2011.

[GK83] I Gupta and A Ksienski. "Effect of mutual coupling on the performance of adaptive arrays." *IEEE Transactions on Antennas and Propagation*, **31**(5):785–791, 1983.

[GLR14] Daniel Gomez-Garcia, Carl Leuschen, Fernando Rodriguez-Morales, Jie-Bang Yan, and Prasad Gogineni. "Linear chirp generator based on direct digital synthesis and frequency multiplication for airborne FMCW snow probing radar." In *2014 IEEE MTT-S International Microwave Symposium (IMS2014)*, pp. 1–4. IEEE, 2014.

[GML14] Malik Muhammad Usman Gul, Xiaoli Ma, and Sungeun Lee. "Timing and frequency synchronization for OFDM downlink transmissions using Zadoff-Chu sequences." *IEEE Transactions on Wireless Communications*, **14**(3):1716–1729, 2014.

[Gol67] Robert Gold. "Optimal binary sequences for spread spectrum multiplexing (Corresp.)." *IEEE Transactions on Information Theory*, **13**(4):619–621, 1967.

[GRS11] O González, David Ramirez, Ignacio Santamaria, José Antonio García-Naya, and Luis Castedo. "Experimental validation of interference alignment techniques using a multiuser MIMO testbed." In *2011 International ITG Workshop on Smart Antennas*, pp. 1–8. IEEE, 2011.

[GSK05] Maxime Guillaud, Dirk TM Slock, and Raymond Knopp. "A practical method for wireless channel reciprocity exploitation through relative calibration." In *ISSPA*, pp. 403–406, 2005.

[GVP08] BP Gorshunov, AA Volkov, AS Prokhorov, and IE Spektor. "Methods of terahertz-subterahertz BWO spectroscopy of conducting materials." *Physics of the solid state*, **50**(11):2001, 2008.

[Has93] Homayoun Hashemi. "The indoor radio propagation channel." *Proceedings of the IEEE*, **81**(7):943–968, 1993.

[HGF17] Danping He, Ke Guan, Alexander Fricke, Bo Ai, Ruisi He, Zhangdui Zhong, Akifumi Kasamatsu, Iwao Hosako, and Thomas Kürner. "Stochastic channel modeling for kiosk applications in the terahertz band." *IEEE Transactions on Terahertz Science and Technology*, **7**(5):502–513, 2017.

[Hui04] Hon Tat Hui. "A new definition of mutual impedance for application in dipole receiving antenna arrays." *IEEE Antennas and Wireless Propagation Letters*, **3**(1):364–367, 2004.

[HYW16] Mohammed Reza M Hashemi, Shang-Hua Yang, Tongyu Wang, Nelson Sepúlveda, and Mona Jarrahi. "Electronically-controlled beam-steering through vanadium dioxide metasurfaces." *Scientific reports*, **6**:35439, 2016.

[HYY17] Shu-Wei Huang, Jinghui Yang, Shang-Hua Yang, Mingbin Yu, Dim-Lee Kwong, Tanya Zelevinsky, Mona Jarrahi, and Chee Wei Wong. "Globally stable microresonator Turing pattern formation for coherent high-power THz radiation on-chip." *Physical Review X*, **7**(4):041002, 2017.

[Jaf11] Syed A Jafar et al. "Interference alignmentA new look at signal dimensions in a communication network." *Foundations and Trends® in Communications and Information Theory*, **7**(1):1–134, 2011.

[Jar15] Mona Jarrahi. "Advanced photoconductive terahertz optoelectronics based on nano-antennas and nano-plasmonic light concentrators." *IEEE Transactions on Terahertz Science and Technology*, **5**(3):391–397, 2015.

[JCK15] Xiwen Jiang, Mirsad Čirkić, Florian Kaltenberger, Erik G Larsson, Luc Deneire, and Raymond Knopp. "MIMO-TDD reciprocity under hardware imbalances: Experimental results." In *2015 IEEE International Conference on Communications (ICC)*, pp. 4949–4953. IEEE, 2015.

[JDP17] Yi Jiang, Babak Daneshrad, and Gregory J Pottie. "A Practical Approach to Joint Timing, Frequency Synchronization and Channel Estimation for Concurrent Transmissions in a MANET." *IEEE Transactions on Wireless Communications*, **16**(6):3461–3475, 2017.

[JPM11] Christian Jansen, Sebastian Priebe, Christoph Moller, Martin Jacob, Hanno Dierke, Martin Koch, and Thomas Kurner. "Diffuse scattering from rough surfaces in THz communication channels." *IEEE Transactions on Terahertz Science and Technology*, **1**(2):462–472, 2011.

[JW04] Michael A Jensen and Jon W Wallace. "A review of antennas and propagation for MIMO wireless communications." *IEEE Transactions on Antennas and Propagation*, **52**(11):2810–2824, 2004.

[KGZ11] Boris Kouassi, Irfan Ghauri, Bassem Zayen, and Luc Deneire. "On the performance of calibration techniques for cognitive radio systems." In *2011 The 14th International Symposium on Wireless Personal Multimedia Communications (WPMC)*, pp. 1–5. IEEE, 2011.

[KJG10] Florian Kaltenberger, Haiyong Jiang, Maxime Guillaud, and Raymond Knopp. "Relative channel reciprocity calibration in MIMO/TDD systems." In *2010 Future Network & Mobile Summit*, pp. 1–10. IEEE, 2010.

[KJP12] T Kleine-Ostmann, M Jacob, S Priebe, R Dickhoff, T Schrader, and T Kürner. "Diffraction measurements at 60 GHz and 300 GHz for modeling of future THz communication systems." In *2012 37th International Conference on Infrared, Millimeter, and Terahertz Waves*, pp. 1–2. IEEE, 2012.

[KLA13] Swen Koenig, Daniel Lopez-Diaz, Jochen Antes, Florian Boes, Ralf Henneberger, Arnulf Leuther, Axel Tessmann, René Schmogrow, David Hillerkuss, Robert Palmer, et al. "Wireless sub-THz communication system with high data rate." *Nature photonics*, **7**(12):977, 2013.

[KX10] K Raj Kumar and Feng Xue. "An iterative algorithm for joint signal and interference alignment." In *2010 IEEE International Symposium on Information Theory*, pp. 2293–2297. IEEE, 2010.

[LCS98] YLJC Li, Leonard J Cimini, and Nelson R Sollenberger. "Robust channel estimation for OFDM systems with rapid dispersive fading channels." *IEEE Transactions on communications*, **46**(7):902–915, 1998.

[LGH14] Seogoo Lee, Andreas Gerstlauer, and Robert W Heath. "Distributed real-time implementation of interference alignment with analog feedback." *IEEE Transactions on Vehicular Technology*, **64**(8):3513–3525, 2014.

[LHL09] Hoi-Shun Lui, Hon Tat Hui, and Mook Seng Leong. "A note on the mutual-coupling problems in transmitting and receiving antenna arrays." *IEEE Antennas and Propagation Magazine*, **51**(5):171–176, 2009.

[LY03] GL Li and PKL Yu. "Optical intensity modulators for digital and analog applications." *Journal of Lightwave Technology*, **21**(9):2010, 2003.

[MBL03] Hlaing Minn, Vijay K Bhargava, and Khaled Ben Letaief. "A robust timing and frequency synchronization for OFDM systems." *IEEE transactions on wireless communications*, **2**(4):822–839, 2003.

[MC04] Nektarios Moraitis and Philip Constantinou. "Indoor channel measurements and characterization at 60 GHz for wireless local area network applications." *IEEE Transactions on Antennas and Propagation*, **52**(12):3180–3189, 2004.

[MEJ09] Konstantinos Manolakis, David Manuel Gutiérrez Estévez, Volker Jungnickel, Wen Xu, and Christian Drewes. "A closed concept for synchronization and cell search in 3GPP LTE systems." In *2009 IEEE Wireless Communications and Networking Conference*, pp. 1–6. IEEE, 2009.

[MFZ14] Nima N Moghadam, Hamed Farhadi, Per Zetterberg, and Mikael Skoglund. "Testbed implementation of iterative interference alignment and power control for wireless MIMO interference networks." In *2014 IEEE 15th International Workshop on Signal Processing Advances in Wireless Communications (SPAWC)*, pp. 239–243. IEEE, 2014.

[MMI96] Takeshi Manabe, Yuko Miura, and Toshio Ihara. "Effects of antenna directivity and polarization on indoor multipath propagation characteristics at 60 GHz." *IEEE Journal on selected Areas in Communications*, **14**(3):441–448, 1996.

[NHM13] Tadao Nagatsuma, Shogo Horiguchi, Yusuke Minamikata, Yasuyuki Yoshimizu, Shintaro Hisatake, Shigeru Kuwano, Naoto Yoshimoto, Jun Terada, and Hiroyuki Takahashi. "Terahertz wireless communications based on photonics technologies." *Optics express*, **21**(20):23736–23747, 2013.

[NK14] Tadao Nagatsuma and Kazutoshi Kato. "Photonically-assisted 300-GHz wireless link for real-time 100-Gbit/s transmission." In *2014 IEEE MTT-S International Microwave Symposium (IMS2014)*, pp. 1–4. IEEE, 2014.

[NOY16] Tadao Nagatsuma, Kazuki Oogimoto, Yu Yasuda, Yusuke Fujita, Yuki Inubushi, Shintaro Hisatake, Aitor Martinez Agoues, and Gonzalo Crespo Lopez. "300-GHz-band wireless transmission at 50 Gbit/s over 100 meters." In *2016 41st International Conference on Infrared, Millimeter, and Terahertz waves (IRMMW-THz)*, pp. 1–2. IEEE, 2016.

[Par92] J.D. Parsons. *The mobile radio propagation channel*. Halsted Press, 1992.

[PDM11] Sascha Preu, GH Döhler, S Malzer, LJ Wang, and AC Gossard. "Tunable, continuous-wave terahertz photomixer sources and applications." *Journal of Applied Physics*, **109**(6):4, 2011.

[PH09] Steven W Peters and Robert W Heath. "Interference alignment via alternating minimization." In *2009 IEEE International Conference on Acoustics, Speech and Signal Processing*, pp. 2445–2448. IEEE, 2009.

[PJJ11] Sebastian Priebe, Christian Jastrow, Martin Jacob, Thomas Kleine-Ostmann, Thorsten Schrader, and Thomas Kurner. "Channel and propagation measurements at 300 GHz." *IEEE Transactions on Antennas and Propagation*, **59**(5):1688–1698, 2011.

[PJM07] Radoslaw Piesiewicz, Christian Jansen, Daniel Mittleman, Thomas Kleine-Ostmann, Martin Koch, and Thomas Kurner. "Scattering analysis for the modeling of THz communication systems." *IEEE Transactions on Antennas and Propagation*, **55**(11):3002–3009, 2007.

[PK13] Sebastian Priebe and Thomas Kurner. "Stochastic modeling of THz indoor radio channels." *IEEE Transactions on Wireless Communications*, **12**(9):4445–4455, 2013.

[PKJ13] Sebastian Priebe, Marius Kannicht, Martin Jacob, and Thomas Kürner. "Ultra broadband indoor channel measurements and calibrated ray tracing propagation modeling at THz frequencies." *Journal of Communications and Networks*, **15**(6):547–558, 2013.

[PSL13] Mark Petermann, Markus Stefer, Frank Ludwig, Dirk Wubben, Martin Schneider, Steffen Paul, and Karl-Dirk Kammeyer. "Multi-user pre-processing in multi-antenna OFDM TDD systems with non-reciprocal transceivers." *IEEE Transactions on Communications*, **61**(9):3781–3793, 2013.

[Rap96] Theodore S Rappaport et al. *Wireless communications: principles and practice*, volume 2. prentice hall PTR New Jersey, 1996.

[RBP14] Ryan Rogalin, Ozgun Y Bursalioglu, Haralabos Papadopoulos, Giuseppe Caire, Andreas F Molisch, Antonios Michaloliakos, Vlad Balan, and Konstantinos Psounis. "Scalable synchronization and reciprocity calibration for distributed multiuser MIMO." *IEEE Transactions on Wireless Communications*, **13**(4):1815–1831, 2014.

[SBH10] Changxin Shi, Randall A Berry, and Michael L Honig. "Adaptive beamforming in interference networks via bi-directional training." In *2010 44th Annual Conference on Information Sciences and Systems (CISS)*, pp. 1–6. IEEE, 2010.

[SC97] Timothy M Schmidl and Donald C Cox. "Robust frequency and timing synchronization for OFDM." *IEEE transactions on communications*, **45**(12):1613–1621, 1997.

[SFB14] Haymen Shams, Martyn J Fice, Katarzyna Balakier, Cyril C Renaud, Frédéric van Dijk, and Alwyn J Seeds. "Photonic generation for multichannel THz wireless communication." *Optics express*, **22**(19):23465–23472, 2014.

[Sie02] Peter H Siegel. "Terahertz technology." *IEEE Transactions on microwave theory and techniques*, **50**(3):910–928, 2002.

[SKA14] Ho-Jin Song, Jae-Young Kim, Katsuhiro Ajito, Naoya Kukutsu, and Makoto Yaita. "50-Gb/s direct conversion QPSK modulator and demodulator MMICs for terahertz communications at 300 GHz." *IEEE Transactions on Microwave Theory and Techniques*, **62**(3):600–609, 2014.

[SLY11] Jing Shi, Qinglin Luo, and Mingli You. "An efficient method for enhancing TDD over the air reciprocity calibration." In *2011 IEEE Wireless Communications and Networking Conference*, pp. 339–344. IEEE, 2011.

[SN11] Ho-Jin Song and Tadao Nagatsuma. "Present and future of terahertz communications." *IEEE transactions on terahertz science and technology*, **1**(1):256–263, 2011.

[SS98] A Lee Swindlehurst and Petre Stoica. "Maximum likelihood methods in radar array signal processing." *Proceedings of the IEEE*, **86**(2):421–441, 1998.

[SWP12] Thomas Schneider, Andrzej Wiatrek, Stefan Preußler, Michael Grigat, and Ralf-Peter Braun. "Link budget analysis for terahertz fixed wireless links." *IEEE Transactions on Terahertz Science and Technology*, **2**(2):250–256, 2012.

[SYA12] Clayton Shepard, Hang Yu, Narendra Anand, Erran Li, Thomas Marzetta, Richard Yang, and Lin Zhong. "Argos: Practical many-antenna base stations." In *Proceedings of the 18th annual international conference on Mobile computing and networking*, pp. 53–64. ACM, 2012.

[TGK08] Jack Tucek, David Gallagher, Ken Kreischer, and Rob Mihailovich. "A compact, high power, 0.65 THz source." In *2008 IEEE International Vacuum Electronics Conference*, pp. 16–17. IEEE, 2008.

[Ton07] Masayoshi Tonouchi. "Cutting-edge terahertz technology." *Nature photonics*, **1**(2):97, 2007.

[VES95] J-J Van De Beek, Ove Edfors, Magnus Sandell, Sarah Kate Wilson, and P Ola Borjesson. "On channel estimation in OFDM systems." In *1995 IEEE 45th Vehicular Technology Conference. Countdown to the Wireless Twenty-First Century*, volume 2, pp. 815–819. IEEE, 1995.

[VRE17] Joao Vieira, Fredrik Rusek, Ove Edfors, Steffen Malkowsky, Liang Liu, and Fredrik Tufvesson. "Reciprocity calibration for massive MIMO: Proposal, modeling, and validation." *IEEE Transactions on Wireless Communications*, **16**(5):3042–3056, 2017.

[VRT14] Joao Vieira, Fredrik Rusek, and Fredrik Tufvesson. "Reciprocity calibration methods for massive MIMO based on antenna coupling." In *2014 IEEE Global Communications Conference*, pp. 3708–3712. IEEE, 2014.

[WCL18] Ning Wang, Semih Cakmakyapan, Yen-Ju Lin, Hamid Javadi, and Mona Jarrahi. "Room temperature terahertz spectrometer with quantum-level sensitivity." *arXiv preprint arXiv:1806.05256*, 2018.

[WV13] Craig Wilson and Venugopal Veeravalli. "A convergent version of the Max SINR algorithm for the MIMO interference channel." *IEEE Transactions on Wireless Communications*, **12**(6):2952–2961, 2013.

[WW09] Chin-Liang Wang and Hung-Chin Wang. "On joint fine time adjustment and channel estimation for OFDM systems." *IEEE Transactions on Wireless Communications*, **8**(10):4940–4944, 2009.

[WW11] Chin-Liang Wang and Hung-Chin Wang. "Optimized joint fine timing synchronization and channel estimation for MIMO systems." *IEEE Transactions on Communications*, **59**(4):1089–1098, 2011.

[WWY15] Hao Wei, Dongming Wang, and Xiaohu You. "Reciprocity of mutual coupling for TDD massive MIMO systems." In *2015 International Conference on Wireless Communications & Signal Processing (WCSP)*, pp. 1–5. IEEE, 2015.

[XKR02] Hao Xu, Vikas Kukshya, and Theodore S Rappaport. "Spatial and temporal characteristics of 60-GHz indoor channels." *IEEE Journal on selected areas in communications*, **20**(3):620–630, 2002.

[YJ15] Shang-Hua Yang and Mona Jarrahi. "Frequency-tunable continuous-wave terahertz sources based on GaAs plasmonic photomixers." *Applied Physics Letters*, **107**(13):131111, 2015.

[YJ18] Nezih Tolga Yardimci and Mona Jarrahi. "Nanostructure-Enhanced Photoconductive Terahertz Emission and Detection." *Small*, **14**(44):1802437, 2018.

[YWL15] S-H Yang, R Watts, X Li, N Wang, V Cojocaru, J OGorman, LP Barry, and M Jarrahi. "Tunable terahertz wave generation through a bimodal laser diode and plasmonic photomixer." *Optics Express*, **23**(24):31206–31215, 2015.

[ZF13] Hans-Jurgen Zepernick and Adolf Finger. *Pseudo random signal processing: theory and application*. John Wiley & Sons, 2013.